THE COLLISIONAL AND DYNAMICAL EVOLUTION OF THE MAIN BELT, NEA AND TNO POPULATIONS

by

David Patrick O'Brien

A Dissertation Submitted to the Faculty of the
DEPARTMENT OF PLANETARY SCIENCES
In Partial Fulfillment of the Requirements
For the Degree of
DOCTOR OF PHILOSOPHY
In the Graduate College
THE UNIVERSITY OF ARIZONA

2 0 0 4

UMI Number: 3131625

INFORMATION TO USERS

The quality of this reproduction is dependent upon the quality of the copy submitted. Broken or indistinct print, colored or poor quality illustrations and photographs, print bleed-through, substandard margins, and improper alignment can adversely affect reproduction.

In the unlikely event that the author did not send a complete manuscript and there are missing pages, these will be noted. Also, if unauthorized copyright material had to be removed, a note will indicate the deletion.

UMI®

UMI Microform 3131625

Copyright 2004 by ProQuest Information and Learning Company.

All rights reserved. This microform edition is protected against unauthorized copying under Title 17, United States Code.

ProQuest Information and Learning Company
300 North Zeeb Road
P.O. Box 1346
Ann Arbor, MI 48106-1346

The University of Arizona ®
Graduate College

As members of the Final Examination Committee, we certify that we have read the

dissertation prepared by David P. O'Brien

entitled The Collisional and Dynamical Evolution of the Main-Belt, NEA and TNO Populations

and recommend that it be accepted as fulfilling the dissertation requirement for the

Degree of Doctor of Philosophy

Richard Greenberg — June 1, 2004
Richard J. Greenberg — date

H. Jay Melosh — 6/3/2004
H. Jay Melosh — date

Jonathan I. Lunine /jw — 6-1-04
Jonathan I. Lunine — date

John S. Lewis /jw — 6-2-04
John S. Lewis — date

Wm Boynton — 6/1/04
William V. Boynton — date

Final approval and acceptance of this dissertation is contingent upon the candidate's submission of the final copies of the dissertation to the Graduate College.

I hereby certify that I have read this dissertation prepared under my direction and recommend that it be accepted as fulfilling the dissertation requirement.

Richard Greenberg — June 1, 2004
Dissertation Director: Richard J. Greenberg — date

STATEMENT BY AUTHOR

This dissertation has been submitted in partial fulfillment of requirements for an advanced degree at The University of Arizona and is deposited in the University Library to be made available to borrowers under rules of the library.

Brief quotations from this dissertation are allowable without special permission, provided that accurate acknowledgment of source is made. Requests for permission for extended quotation from or reproduction of this manuscript in whole or in part may be granted by the head of the major department or the Dean of the Graduate College when in his or her judgment the proposed use of the material is in the interests of scholarship. In all other instances, however, permission must be obtained from the author.

SIGNED:

ACKNOWLEDGEMENTS

I guess I have always known that I would be a scientist when I grew up, and I am thankful for the many positive influences and opportunities in my life that have helped me along that path. Even more so, I am thankful for the friendships I have made and the chances I've had to grow as a person while I've progressed in my scientific career. The people I am grateful to and the memories I'd like to recount here deserve far more than the single page allowed by Grad College, but since that's the rule, here goes.....

First and foremost, I would like to thank my family (nuclear and extended) for giving me so much support and for being a great bunch of people to spend time with. Thanks to the many friends I made during my undergraduate years at Cornell, especially Mark, who was always there for me as a friend and wasn't afraid to tell me when I was doing something too stupid for my own good. Many thanks to Steve Squyres at Cornell, who gave me my first job in planetary science. If it weren't for that job, I may have ended up as an astronomer, or even worse, a physicist.

As for grad school, I can't imagine a better place to have spent the last 6 years than LPL. Many thanks to the faculty I have taken classes from and worked with, especially Jay Melosh, Jonathan Lunine, Bob Brown, Ralph Lorenz, Zibi Turtle, and Renu Malhotra. Thanks in particular to my advisor, Rick Greenberg. He was always more than willing to help me out and offer advice, and it was always fun to chat with him about non-work stuff as well. The asteroid community in general has been a very friendly and cooperative bunch, and I would specifically like to thank Bill Bottke, Dan Durda, and Jean-Marc Petit for their help and advice during my graduate career.

Many thanks to my fellow inhabitants of the closet office, Fred and Jason. We certainly proved that lack of sunlight does not hinder brilliance. Thanks to my fellow 'Fun Boys' Fred, Terry and Gareth for keepin' it fun. Thanks to my current and past roommates at Hawthorne House for keeping the HH tradition alive despite the occasional cockroach invasions and the general odd smell of the place. The many traditions of LPL, both old and new, deserve mention for making the department a fun place to be and for preventing us from going too insane: Bratfest is the greatest party ever; April Fools pranks and Christmas Skits give us the chance to get back at the faculty; Narcolepsy, the LPL soccer team, provides necessary exercise to counteract hours of sitting in front of computers; Thesis burnings give a sense of finality to our graduate careers; Friday Beers gives us the chance to get together and relax, discuss, complain, and gossip; Thursday Beers gives us the chance to do the same thing one day earlier; Wednesday Beers.....

As I'm basically out of space, I'll issue a blanket 'thank you' to the many other people I've met during my time at LPL and that I'm fortunate to have as my friends. Thank you all for helping to make my time here enjoyable and memorable. The final thanks goes to Brooke White, who has been an important and wonderful part of my life for my last three years here. Thank you B!

DEDICATION

To my family, friends and colleagues,
who have helped me get to where I am today
while still retaining most of my sanity

TABLE OF CONTENTS

LIST OF FIGURES **8**
LIST OF TABLES **10**
ABSTRACT **11**
CHAPTER 1 Introduction **13**
CHAPTER 2 Background **18**
  2.1 Observational Constraints 18
    2.1.1 Main-Belt Size Distribution 18
    2.1.2 NEA Size Distribution 19
    2.1.3 Meteorite Cosmic Ray Exposure Ages 21
    2.1.4 Asteroid Families 24
    2.1.5 Vesta's Basaltic Crust 29
    2.1.6 Craters on Asteroids 29
  2.2 Asteroid Strength 31
CHAPTER 3 Analytical Collisional Evolution Model **37**
  3.1 Introduction 37
  3.2 Single-Slope Collisional Model 39
    3.2.1 Collisional Destruction 40
    3.2.2 Collisional Production 42
    3.2.3 Collisional Steady State 45
    3.2.4 Proof of Uniqueness of Analytical Solution 46
  3.3 Two-Slope Collisional Model 47
    3.3.1 Gravity Scaled Portion of the Population 48
    3.3.2 Strength Scaled Portion of the Population 50
    3.3.3 Waves in the Size Distribution 53
  3.4 Comparison to Numerical Results 60
  3.5 Summary and Implications 66
CHAPTER 4 Asteroid and Meteorite Dynamics **70**
  4.1 Development of the 'Modern' Delivery Scenario 70
  4.2 The Bottke et al. Simulations 78
  4.3 Summary and Discussion 80
CHAPTER 5 Yarkovsky-Driven Asteroid Removal **82**
  5.1 Diurnal Yarkovsky Force 83
  5.2 Seasonal Yarkovsky Force 86
  5.3 Semi-major Axis Mobility due to the Yarkovsky Effect 91
  5.4 The Yarkovsky Effect and Asteroid Removal 96

TABLE OF CONTENTS — *Continued*

CHAPTER 6 Numerical Collisional/Dynamical Model **102**
- 6.1 NEA and Main Belt Collisional and Dynamical Evolution Model . . 103
  - 6.1.1 Outcome of Single Collisional Events 103
  - 6.1.2 Full Model 114
- 6.2 Effects of Different Collisional Parameters 119
- 6.3 Results 124

CHAPTER 7 Comparison to Asteroid Cratering Records **136**
- 7.1 Properties of Asteroids Observed by Spacecraft 136
- 7.2 Crater Production 136
- 7.3 Crater Erasure Mechanisms 143
  - 7.3.1 Jolt 143
  - 7.3.2 Overlap of Craters 145
  - 7.3.3 Local Jolt 147
- 7.4 Results 148

CHAPTER 8 Collisional Evolution of Trans-Neptunian Objects . **150**
- 8.1 Introduction 150
- 8.2 The Structure and Dynamical History of the TNO Region 152
- 8.3 The Link Between TNOs and the Jupiter-Family Comets 154
- 8.4 The Size-Distribution of the TNO Population 155
- 8.5 Application of Analytical Model 156
- 8.6 Numerical Simulations 160
- 8.7 Conclusion 167

CHAPTER 9 Summary and Discussion **169**

APPENDIX A Power-Law Size and Mass Distributions **173**

REFERENCES **180**

LIST OF FIGURES

2.1 Observational estimates of the main belt size distribution. 20
2.2 Observational estimates of the NEA size distribution. 22
2.3 Estimate of the NEA size distribution from lunar cratering data compared with observational estimates 23
2.4 Cosmic ray exposure age histograms for ordinary chondrites. 25
2.5a Proper a and e for numbered asteroids 27
2.5b Proper a and i for numbered asteroids 28
2.6 Crater populations on asteroids observed by spacecraft. 30
2.7 Estimates of Q_S 34
2.8 Estimates of Q_D^* 35
3.1 Hypothetical Q_D^* law 49
3.2a Wave formation in collisional populations 55
3.2b Wave formation in collisional populations 56
3.2c Wave formation in collisional populations 57
3.3 Comparison of analytical and numerical results 62
3.4 Comparison of numerical and analytical models 63
3.5 Q_D^* used for comparison between analytical and numerical results . . . 64
5.1 Diagram illustrating the 'diurnal' Yarkovsky effect. 84
5.2 Diagram illustrating the 'seasonal' Yarkovsky effect. 88
5.3 Geometry used for calculation of the 'seasonal' Yarkovsky effect. 89
5.4 Plot of the Yarkovsky semimajor-axis drift rate $\dot{a}$ of stony bodies . . . 93
5.5 Plot of the Yarkovsky semimajor-axis drift rate $\dot{a}$ of iron bodies 94
5.6 Plot of the Yarkovsky semimajor-axis drift rate $\dot{a}$ of stony bodies with size-dependent thermal properties 97
5.7 Plot of the Yarkovsky removal rate as a function of diameter 100
6.1 Different Q_S curves yielding the same Q_D^* 120
6.2 Dependence of evolved population on Q_S for constant Q_D^* 122
6.3 Dependence of Evolved Population on Cratering Efficiency 123
6.4 Family of Q_D^* curves that can potentially reproduce the positions of peaks and valleys in the main-belt size distribution 126
6.5 Best-fit main belt population 128
6.6 Strength law for best-fit main-belt population 129
6.7 Lifetimes of bodies in best-fit main belt population 130
6.8 Non-collisional removal rates used for best-fit population 131
6.9 Simulated NEA population 132

LIST OF FIGURES — *Continued*

6.10 Main belt population evolved without non-collisional removal 134
7.1 Crater diameter vs. projectile diameter for Gaspra, from hydrocode simulations by Nolan et al. (1996) 140
7.2 Crater diameter vs. projectile diameter for Gaspra, Ida, Mathilde, and Eros 144
7.3 Crater erasure due to global jolting in impacts 146
7.4 Comparison of best-fit main-belt population to asteroid cratering records 149
8.1 Observational estimate of the size distribution of all TNOs 157
8.2 Observational estimate of the 'classical' and 'excited' TNO size distributions 158
8.3 Strength law for icy bodies 161
8.4 Classical TNO collisional evolution (steep initial population) 163
8.5 Excited TNO collisional evolution (steep initial population) 164
8.6 Classical TNO collisional evolution (shallow initial population) 165
8.7 Excited TNO collisional evolution (shallow initial population) 166

LIST OF TABLES

4.1 Dynamical properties of NEA source regions 79
5.1 Asterioid thermal parameters 85
6.1 Asteroid collision velocities and probabilities 115
7.1 Properties of asteroids that have been observed by spacecraft 137
7.2 Pi-group scaling constants for competent rock and loose sand 142
8.1 TNO collision velocities and probabilities 160
A.1 Different power-law representations of size and mass distributions . . . 179

ABSTRACT

The size distribution of main-belt of asteroids is determined primarily by collisional processes. Large asteroids break up and form smaller asteroids in a collisional cascade, with the outcome controlled by the strength-vs.-size relationship for asteroids. We develop an analytical model that incorporates size-dependent strength and is able to reproduce the general features of the main-belt size distribution.

In addition to collisional processes, the non-collisional removal of asteroids from the main belt (and their insertion into the near-Earth asteroid (NEA) population) is critical, and involves several effects: Strong resonances increase the orbital eccentricity of asteroids and cause them to enter the inner planet region; Chaotic diffusion by numerous weak resonances causes a slow leak of asteroids into the Mars- and Earth-crossing populations; And the Yarkovsky effect, a radiation force on asteroids, is the primary process that drives asteroids into these resonant escape routes. Yarkovsky drift is size-dependent and can potentially modify the main-belt size distribution. The NEA size distribution is primarily determined by its source, the main belt population, and by the size-dependent processes that deliver bodies from the main belt. All of these processes are simulated in a numerical collisional evolution model that incorporates removal by non-collisional processes. This model yields the strength-vs.-size relationship for main-belt asteroids and the non-collisional removal rates from the main belt required for consistency with the observed main-belt and NEA size distributions. Our results are consistent with other estimates of strength and removal rates, and fit a wide range of constraints, such as the number of observed asteroid families, the preserved basaltic crust of Vesta, the cosmic ray exposure ages of meteorites, and the observed cratering records on

asteroids.

Finally, our analytical and numerical models are applied to the collisional evolution of the trans-Neptunian objects (TNOs). We show that the TNO population likely started with a shallow initial size distribution, and that bodies $\gtrsim$ 10 km in diameter are likely not in a collisional steady state. In addition, we show that the population of bodies in the TNO region below the size range of recent observational surveys is likely large enough to explain the observed numbers of Jupiter-family comets.

CHAPTER 1

Introduction

The work of Öpik (1951) and Piotrowski (1952, 1953) showed that main-belt asteroids collide with one another at velocities of ~ 5 km/s, and that these collisions occur frequently over geologic time. Since those early works, the evolution of the asteroid size distribution due to such collisions has been considered by many authors. The theoretical models of Dohnanyi (1969), Greenberg and Nolan (1989), Williams and Wetherill (1994), and Tanaka et al. (1996) all showed that for a population of self-similar colliding bodies (all bodies have the same collisional response parameters, such as strength per unit mass), the steady-state is a differential power-law size distribution

$$\mathrm{d}N = BD^{-p}\mathrm{d}D \tag{1.1}$$

where D is the diameter, $\mathrm{d}N$ is the incremental number of bodies in the size range $[D, D + \mathrm{d}D]$, B is a constant, and the power law index $p = 3.5$, independent of the details of the collisional physics. See Appendix A for how the differential size distribution is related to other commonly used representations of the size distribution, such as the cumulative number distribution and the log-incremental distribution.

As theoretical understanding of the evolution of the main-belt size distribution has improved, so has our knowledge of the actual population from observational studies. Extensive survey programs such as Spacewatch (Jedicke and Metcalfe, 1998), the Sloan Digital Sky Survey (SDSS) (Ivezić et al., 2001), and the Subaru Sub-km Main Belt Asteroid Survey (SMBAS) (Yoshida et al., 2003), with appropriate corrections for observational biases, give estimates of the main-belt size distribution down to diameters as small as ~ 500 m.

The main-belt size distribution differs significantly from the single power law predicted by earlier theories, and is in fact 'wavy' with an average power law index p less than the classical value of 3.5. This disagreement with theory is due primarily to the fact that, as we discuss in Chapter 2, contrary to earlier assumptions, the strength of an asteroid does depend on its size: For small bodies ($D \lesssim 1$ km), material properties such as the flaw distribution control the strength, making them weaker with increasing size; Larger bodies, which have significant self-gravity, become stronger with increasing size due to gravitational self-compression and even if they break up, they are effectively stronger due to the gravitational reaccumulation of fragments.

Size-dependent strength is accounted for in the analytical model of O'Brien and Greenberg (2003) (also Chapter 3 of this dissertation), as well as in numerical collisional evolution models (Durda, 1993; Davis et al., 1994; Durda and Dermott, 1997; Durda et al., 1998; Marzari et al., 1999). In general, the power-law index p of the population is expected to be > 3.5 when strength decreases with increasing size and < 3.5 when strength increases with size. Therefore, on a log-log plot, the small-body portion of the size-distribution, for which material properties dominate the strength, should be steeper than the large-body part, where gravity dominates. In addition, these researchers found that the transition between these two different regimes creates 'waves' that propagate through the large body size distribution. For a given set of size-dependent strength parameters for asteroids, collisions can 'sculpt' the main-belt size distribution. Conversely, given knowledge of the main-belt size distribution from surveys such as Spacewatch, the Sloan Digital Sky Survey (SDSS), and the Subaru Sub-km Main Belt Asteroid Survey (SMBAS), we are able to place constraints on the strength law for asteroids.

Collisions are not the only process that affects the main-belt size distribution. Numerous dynamical mechanisms (described in detail in Chapter 4) can influence it as well: Orbital resonances between asteroids and the planets (primarily Jupiter, Saturn, and Mars) provide 'escape routes' from the main belt; Also, the Yarkovsky effect, a radiation force, provides semi-major-axis mobility to asteroids that can sweep them into these resonances and thus remove them from the main belt. The Yarkovsky effect is size-dependent, and can therefore affect the size distribution of the main belt.

Because of this size dependence, the shape of the main belt size distribution can be changed. Moreover, the bodies leaving the main belt through resonances enter the near-Earth asteroid (NEA) population. Indeed, the size distribution of NEAs is determined by the main-belt population from which they came and the size-dependent dynamical processes that helped deliver them. Thus, observational estimates of the NEA population from surveys such as Spacewatch and the JPL NEAT survey (Rabinowitz et al., 2000) and the MIT Lincoln Lab LINEAR survey (Stuart, 2001; Harris, 2002) serve as a constraint on the dynamical transport mechanisms between the main belt and NEAs, as well as a constraint on properties of the main-belt population itself.

A comprehensive model of main belt and NEA evolution must treat both collisional and dynamical processes. Without collisional evolution in the main belt, asteroid sizes depleted by dynamical mechanisms would never be replenished. Both the main belt and NEA populations would then have severe gaps in their size distributions. Likewise, without dynamical mechanisms operating, there would be no NEA population. With both processes acting coevally, the NEA population is sustained by the input of material from the main belt and the bodies removed from the main belt are partially replenished by fresh collisional fragments (thus preventing a runaway depletion).

There are 6 major observational constraints that must be satisfied by a comprehensive collisional and dynamical evolution model: It must reproduce (1) the main belt and (2) the NEA size distributions; (3) collisional lifetimes of meter-scale bodies must be consistent with the cosmic ray exposure (CRE) ages of stony meteorites; (4) the number of collisional disruption events involving bodies on the order of 200 km or larger must be consistent with the number of currently observable asteroid families; (5) the level of collisional intensity must be low enough that the basaltic crust of Vesta is preserved; And (6) the population of km-scale and smaller bodies must be consistent with the observed cratering records on Gaspra, Ida, Mathilde, and Eros. Such a model must also be consistent with independent estimates of asteroid strength in the literature, and must be consistent with dynamical models of the delivery of NEAs. No previous single model has attempted to reconcile all of these constraints.

In Chapter 2 we discuss the observational constraints just described, and discuss asteroid strength in terms of appropriate definitions, parameterizations, and theoretical and experimental constraints. In Chapter 3 we develop the first analytical collisional evolution model that incorporates size-dependent strength. That model is able to reproduce the general features of the main-belt size distribution (constraint 1), such as the transition in slope between small and large bodies and the development of a wave due to that transition.

Chapter 4 provides a review the dynamics involved in the transport of material between the main belt and NEA population, and identifies the results of previous dynamical studies that we will incorporate into our numerical model. In Chapter 5, we give a review of the Yarkovsky effect and derive an approximate relation for the removal rate from the main belt as a function of size. In Chapter 6 we develop a numerical model to treat the simultaneous collisional and dynamical evolution of the main belt and NEAs. We present the strength law and dynamical parameters that best fit the constraints 1-5, and show that our results are consistent with the estimates of asteroid strength by other authors and the dynamical results presented in Chapters 4 and 5. Finally, in Chapter 7 we show that the best-fit main-belt population presented in Chapter 6 is consistent with the final constraint, the cratering records observed on asteroids.

A natural application of the analytical and numerical tools that we have developed for studying asteroids is to model the collisional evolution of the trans-Neptunian object (TNO) population, which, like the asteroid belt, is a population that evolves under the influence of mutual collisions. The population of TNOs has recently been estimated, from an HST survey, down to a diameter of $\sim$ 10 km (Bernstein et al., 2003). In Chapter 8, we use our analytical and numerical models to help constrain the evolutionary history of the TNOs, and to infer what the population of TNOs below $\sim$ 10 km may be. Our results can potentially explain the discrepancy, noted by Bernstein et al. (2003), between observational estimates of the TNO population and dynamical models of the delivery of Jupiter-family comets.

CHAPTER 2

Background

This chapter consists of two sections. In the first section, we present the six primary observational constraints on the collisional and dynamical evolution of the asteroid belt. In the second section, we present the different definitions of asteroid strength in terms of appropriate definitions, parameterizations, and theoretical and experimental constraints, and we summarize published estimates of asteroid strength.

2.1 Observational Constraints

2.1.1 Main-Belt Size Distribution

The population of main-belt asteroids is 'observationally' complete to $\sim$ 30 km in diameter. For smaller asteroids, the Spacewatch survey (Jedicke and Metcalfe, 1998) provides a good estimate of the population down to a few km. The observed magnitudes of these asteroids can be converted into diameters using albedos derived from IRAS observations (which are available as a function of size and position in the main belt), as discussed by Durda and Dermott (1997, 1998). We use their values for the size distribution of asteroids larger than $\sim$ 3 km in diameter (D. Durda, private communication). Two recent observational surveys allow us to extrapolate this population down to smaller sizes. The Sloan Digital Sky Survey (Ivezić et al., 2001) finds a power-law index $p = 2.3 \pm 0.05$ (1.3 ± 0.05 cumulative) for the size distribution of asteroids between $\sim$ 400 m and 5 km in diameter, but estimates about a factor of two fewer small bodies than the Spacewatch survey at similar sizes. This discrepancy is likely due to a normalization error resulting from the much smaller section of sky searched by the SDSS (R. Jedicke, private communication). Here we adopt the slope found by the SDSS, but normalize the numbers by a constant factor to fit the Spacewatch results at 3-5 km. In this way we extend the estimate of the main-belt size distribution down to sub-km sizes. The Subarau Sub-km Main-Belt Asteroid Survey (SMBAS) (Yoshida et al., 2003) found a power-law index $p = 2.19 \pm 0.02$ for asteroids in the 500 m - 1 km diameter range, which is very close to the SDSS estimate in that size range, and can also be used to extrapolate the Spacewatch estimate down to sub-km sizes. A plot showing all of these estimates of the main belt size distribution is shown in Fig. 2.1.

2.1.2 NEA Size Distribution

The population of near-Earth asteroids (defined as asteroids with perihelia $q \leq 1.3$ AU and aphelia $Q \geq 0.983$ AU (Rabinowitz et al., 1994)) has been estimated by several surveys. Converting the results of these surveys into diameters is difficult since independent determinations of NEA albedos are not as extensive as the main-belt IRAS observations. Moreover, those albedos that have been determined (generally by ground-based IR observations) have a much wider range of values than those of main-belt asteroids (Delbó et al., 2003). Hence, we describe the NEA size distribution in terms of the absolute magnitude H rather than diameter D. H is defined as the visual magnitude an object would have if it were 1 AU from the Sun and observed at a distance of 1 AU at a phase angle of zero. If the visual geometric albedo p_V is known, the diameter (in kilometers) can be found from

$$D = \frac{1347}{\sqrt{p_V}} 10^{-H/5} \tag{2.1}$$

(see Bowell et al. (1989), Eq. A6). For an albedo $p_V = 0.11$, $H = 18$ corresponds to a diameter of approximately 1 km. Assuming a constant albedo, as the H-magnitude

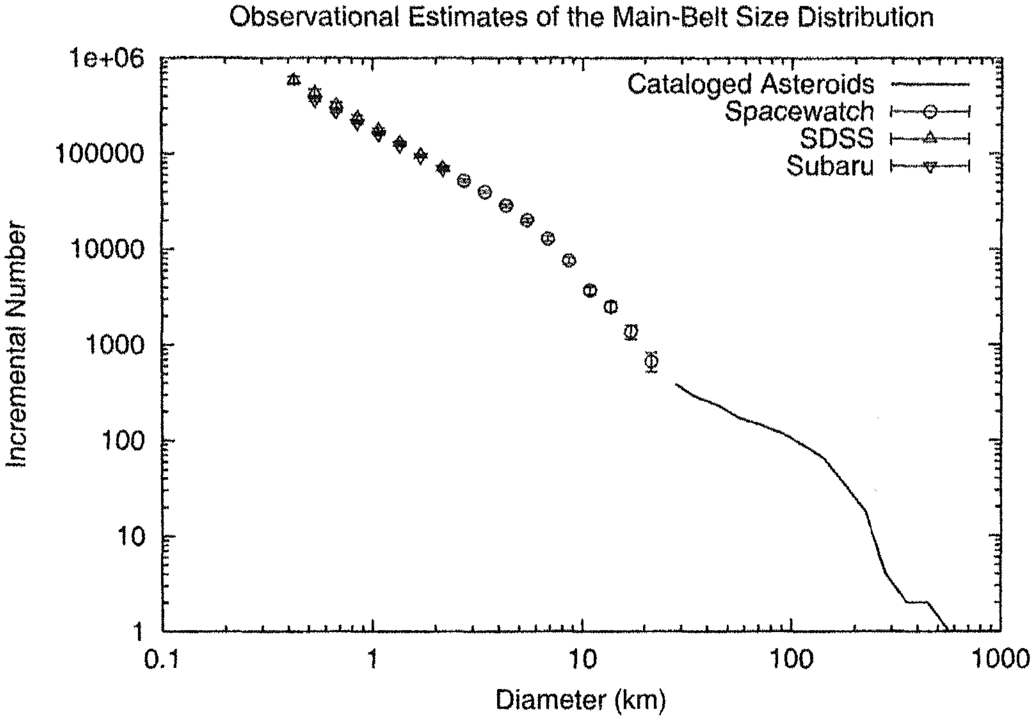

Figure 2.1: Observational estimates of the main belt size distribution. The solid line is the population of observed asteroids, and open circles are from Spacewatch main-belt observations (Jedicke and Metcalfe, 1998). These data, converted to diameters, were provided by D. Durda. The triangles are an extrapolation based on the Sloan Digital Sky Survey (Ivezić et al., 2001), and the upside-down triangles are an extrapolation base on the Subaru Sub-km Main Belt Asteroid Survey (Yoshida et al., 2003).

of a body increases, its diameter decreases.

Direct observations yield population statistics that are reasonably complete up to about $H = 15$ (we use the JPL DASTCOM database[1]). Using Spacewatch data along with data from JPL's Near Earth Asteroid Tracking (NEAT) program, Rabinowitz et al. (2000) estimated the NEA H-magnitude distribution down to an H magnitude of 30 (4 m in diameter for an albedo p_V=0.11). Based on MIT's Lincoln Lab's LINEAR survey, Stuart (2001) estimated the H-magnitude distribution of NEAs down to $H = 22.5$. Harris (2002), using the same dataset but a different technique to correct for observational biases, extended the NEA estimate down to $H = 25.5$ (the actual data are reported in Brown et al. (2002)). The estimates of the NEA H-distribution based on these observational surveys are shown in Fig. 2.2.

Werner et al. (2002) used the lunar cratering record to derive the impacting population on the lunar surface (i.e. the NEAs). Their results give an NEA population in terms of diameter, as opposed to the absolute magnitudes obtained from observational data. Figure 2.3 shows the estimates obtained from lunar craters converted to absolute magnitudes using albedos p_V of 0.11 and 0.40. The low-albedo curve best fits the larger (small H) NEAs and the high-albedo curve best fits the smaller NEAs.

2.1.3 Meteorite Cosmic Ray Exposure Ages

Another important observable quantity is the cosmic-ray exposure (CRE) age distribution of meteorites. CRE ages give the length of time a body has been exposed in space as a meter-scale object or near the surface of a larger body. Material in the interior of an asteroid or on the surface of the Earth is not exposed to cosmic rays. Thus, CRE ages tell us the time between when a meteoroid was liberated from its parent body and when it landed on Earth. The most common meteorites, the

---

[1] http://ssd.jpl.nasa.gov/sb_elem.html

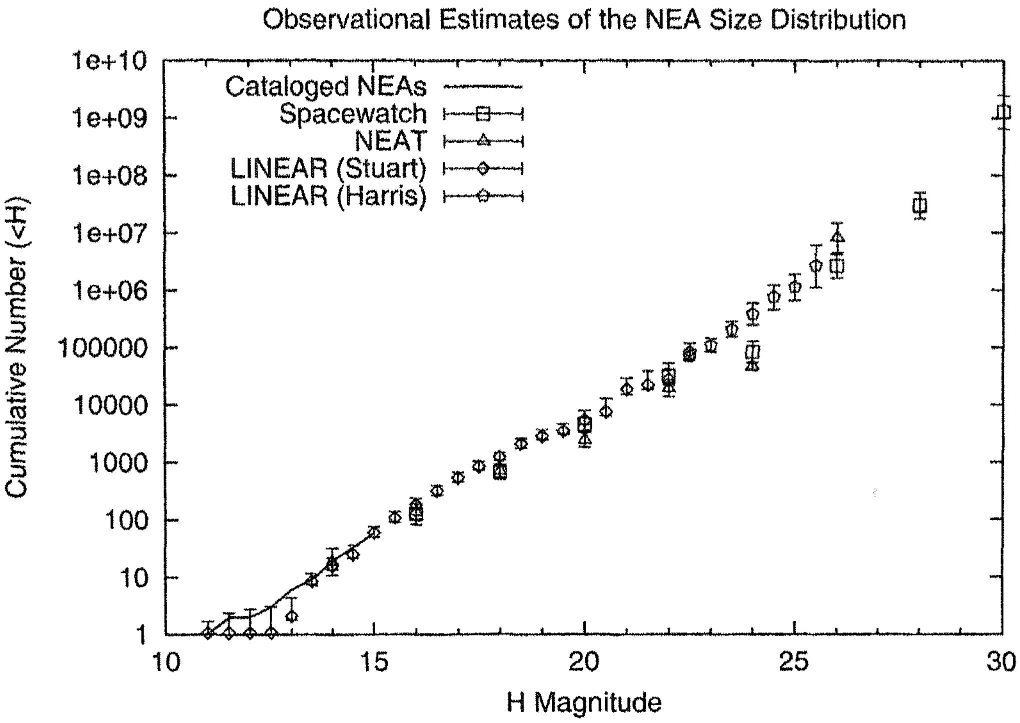

Figure 2.2: Observational estimates of the NEA size distribution. The solid line is the cataloged population of NEAs from the JPL DASTCOM database. Squares and triangles are the Rabinowitz et al. (2000) estimate using Spacewatch and NEAT data. Diamonds are the Stuart (2001) estimate using LINEAR data, and pentagons are the Harris (2002) extension of that estimate, published in Brown et al. (2002). Assuming a constant albedo, as the H-magnitude of a body increases, its diameter decreases.

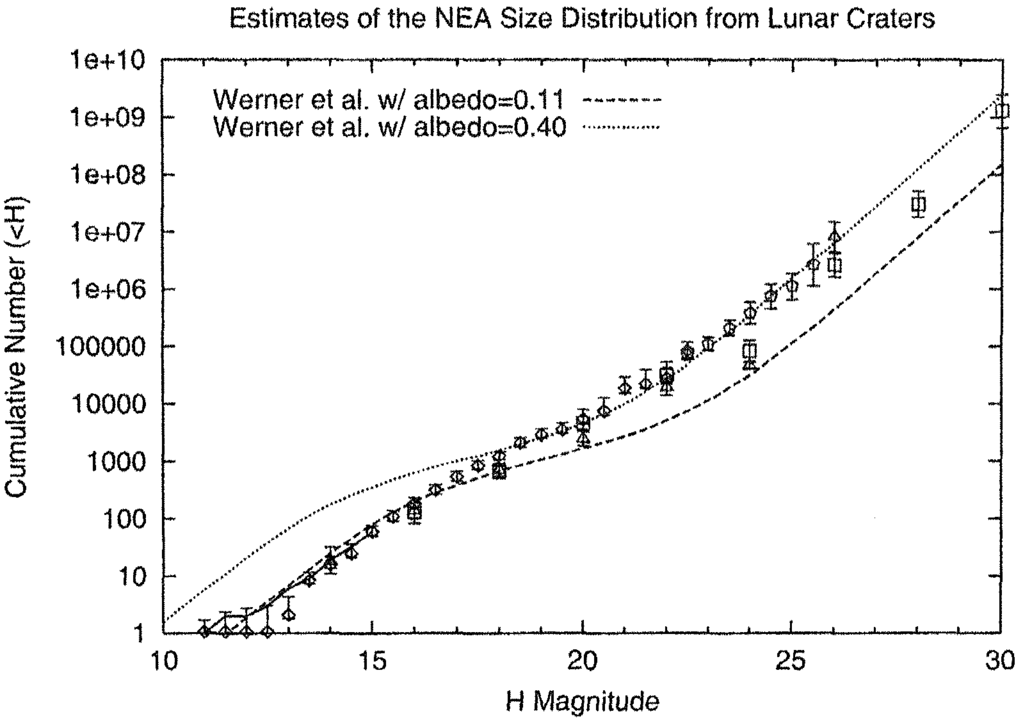

Figure 2.3: Estimate of the NEA size distribution from lunar cratering data (Werner et al., 2002) superimposed on the observational data from Fig. 2.2. The crater-derived data is originally in terms of diameter, and has been converted (using conversion factors from Werner et al.) to absolute magnitude H using albedos p_V of 0.11 and 0.40. Assuming a constant albedo, as the H-magnitude of a body increases, its diameter decreases. It is clear from this plot that the low-albedo curve best fits the larger NEAs (small H) and the-high albedo curve best fits the smaller NEAs, indicating that the albedo of NEAs is likely a function of size.

ordinary chondrites, have CRE ages ranging from a few million years to $\sim$ 100 Myr with a mean age of around 20 Myr (Marti and Graf, 1992). The different subclasses of ordinary chondrites have peaks at different ages, such as the prominent 8 Myr peak for the H chondrites, which is possibly the result of a significant impact event. Figure 2.4 shows the distributions of CRE ages for the different chondrite types. Achondrites have CRE ages similar to those of ordinary chondrites (Welten et al., 1997). Iron meteorites, on the other hand, have CRE ages on the order of 100 Myr - 1 Gyr, a factor of 10-100 larger than those of stony meteorites (Caffee et al., 1988).

Complex exposure histories, which occur when the geometry of irradiation changes, can be found in some meteorites. Such geometry changes could occur if a meteorite was on the surface of a larger parent body or buried at a shallow depth within the body, was liberated by a collision, then accumulated more exposure before arriving at Earth. The presence of a large number of meteorites with complex CRE histories would indicate that the precursor bodies of meteorites were relatively small (10 m or less in diameter), such that most of their mass was not strongly shielded from cosmic rays. Conversely, the lack of meteorites with complex CRE histories would indicate larger parent bodies. It has been estimated from some models of meteorite delivery that a significant fraction of meteorites should have complex exposure histories (e.g. Wetherill (1985), Vokrouhlický and Farinella (2000)). Complex exposure histories, however, require high precision measurements of different isotope ratios to detect, so there is not a large number of meteorites with positively identified complex CRE histories. Thus, we do not consider complex CRE histories to be a significant constraint on our models.

2.1.4 Asteroid Families

It has been known for nearly a century that there are clusterings of asteroids in orbital element space that are not random, but in fact result from the breakup of

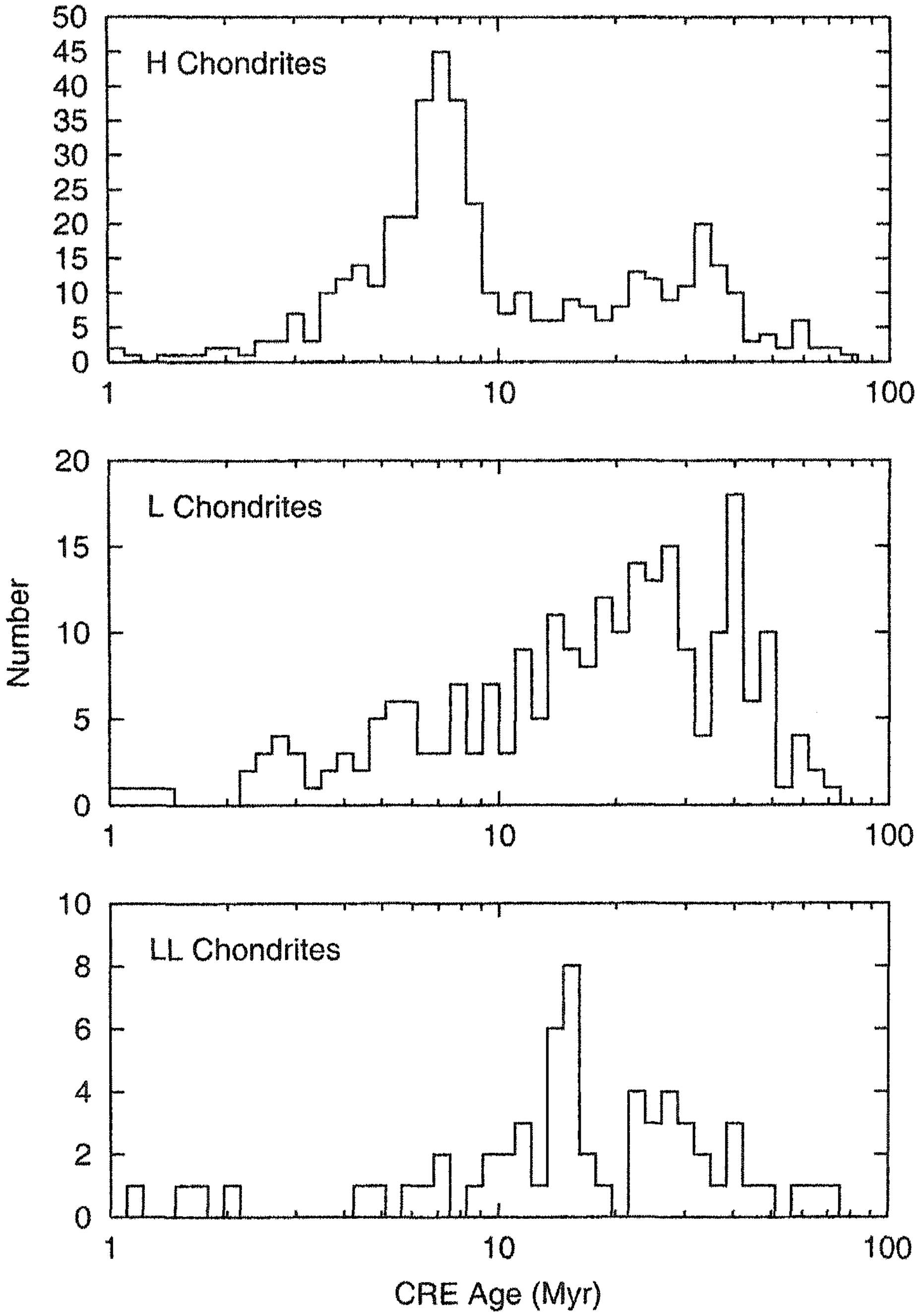

Figure 2.4: Cosmic ray exposure age histograms for ordinary chondrites. This figure is from Morbidelli and Gladman (1998) based on data provided to them by T. Graf.

a large parent body (Hirayama, 1918). The instantaneous, or osculating, orbital elements generally experience long- and short-period oscillations in their values due to planetary perturbations, which hide family clusterings (as reviewed by Knežević et al. (2002)). Proper elements eliminate these oscillations, and thus are nearly constant in time. Proper elements can be calculated from osculating elements either through analytic theory or with a fully numerical procedure ('synthetic'). We use the synthetic proper elements from the database of Knežević and Milani (2003)[2]. Figures 2.5a and 2.5b show plots of the semimajor axis a vs. the eccentricity e and vs. the inclination i for all of the numbered asteroids.

There are 8 asteroid families whose parent bodies were larger than 200 km in diameter (Davis et al., 1985). Several of them are immediately apparent in Figs. 2.5a and 2.5b, and have been known since the work of Hirayama (1918). More recently, Zappalá et al. (1995) used two different statistical methods on a large dataset of proper elements to identify smaller families. They found a total of 63 statistically significant clusterings with both methods, classifying either 30 or 32 of them as actual families and the rest as 'clumps,' which are statistically significant clusterings that are less pronounced than families.

Recently, Marzari et al. (1999) developed a numerical collisional evolution simulation that tracks the evolution of the entire main belt as well as individual families (formed from parent bodies larger than 100 km in diameter) as they are created. They found that the largest families (those with parent bodies larger than 200 km) would remain identifiable after 4.5 Gyr. Up to 90% of smaller families formed over the history of the solar system, however, would no longer be distinguishable due to collisional erosion. While their results are dependent somewhat on the collisional parameters they use, their general result that families formed from the breakup of the largest parent bodies can survive for the history of the solar system is likely to be true for any reasonable parameter choices.

---

[2] http://hamilton.dm.unipi.it/astdys

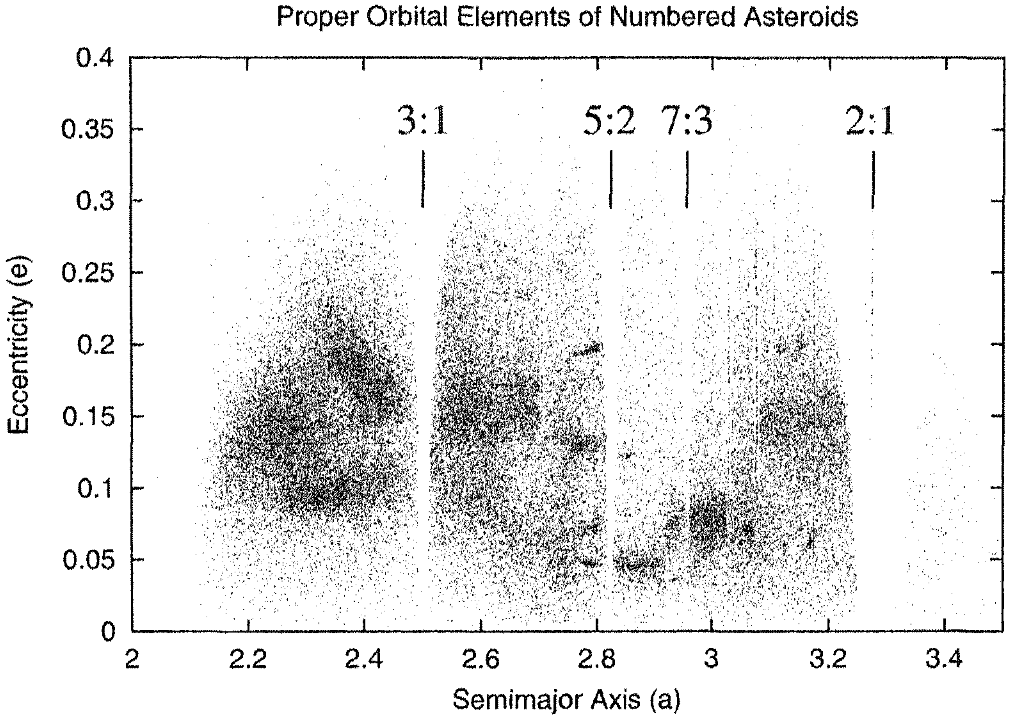

Figure 2.5a: Plots of the proper a and e of numbered asteroids from the database of Knežević and Milani (see Knežević and Milani (2003) for information about this database, which is accessible online). Major resonances are labeled, and a number of asteroid families are clearly visible.

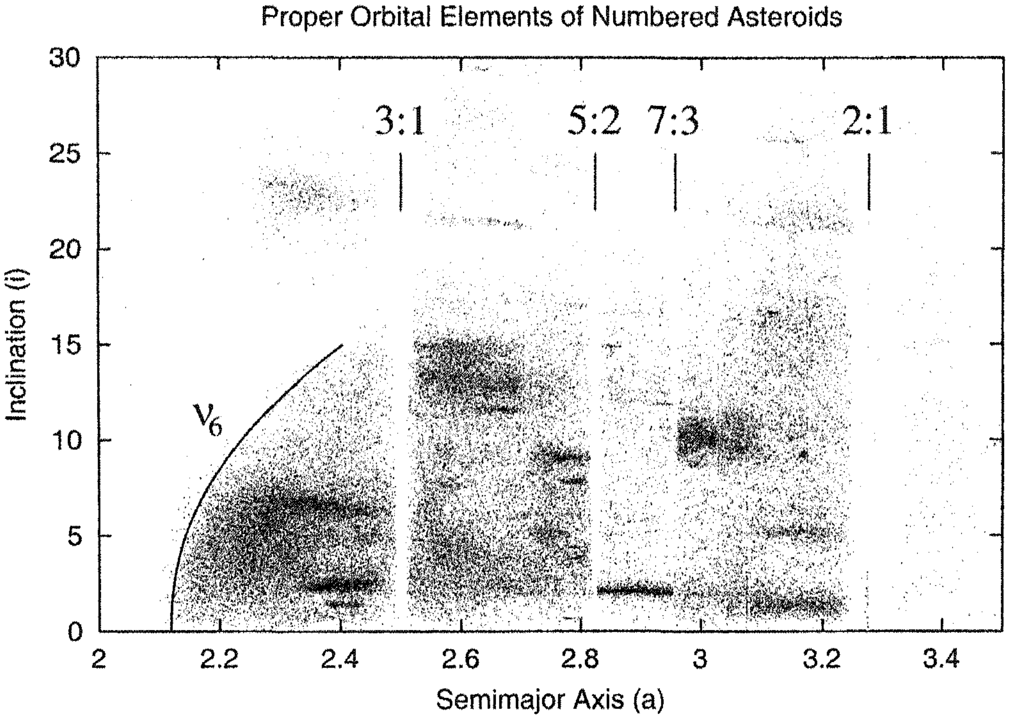

Figure 2.5b: Plots of the proper a and i of numbered asteroids from the database of Knežević and Milani (see Knežević and Milani (2003) for information about this database, which is accessible online). Major resonances are labeled, and a number of asteroid families are clearly visible.

The existence of the 8 large asteroid families requires that, in our model, about 8 parent bodies larger than 200 km break up over the history of the solar system. As the number of smaller families that are currently observable depends more sensitively on the collisional parameters used, and is much more computationally intensive to track, do not consider the smaller families as a constraint on our model.

2.1.5 Vesta's Basaltic Crust

The asteroid Vesta has a nearly intact crust of basaltic composition, as determined from ground-based spectra (McCord et al., 1970), and indeed is the likely parent body of the HED basaltic achondrite meteorites (Consolmagno and Drake, 1977; Feierberg and Drake, 1980). Such a crust is the product of bulk compositional differentiation within the asteroid shortly after its formation. Hence, the preservation of this crust places a limit on the intensity of the collisions Vesta has experienced (Davis et al., 1985). For our model to be successful, it must minimize the possibility of the catastrophic fragmentation of Vesta-sized (500 km) bodies, since catastrophic fragmentation, while not destroying Vesta, would likely have disrupted the surface and mixed the crust with underlying material to a degree that would be detectable spectroscopically.

2.1.6 Craters on Asteroids

A final constraint on our model comes from spacecraft observations of asteroids. Four asteroids have been observed by spacecraft—Gaspra and Ida by Galileo and Mathilde and Eros by NEAR—and from these observations the crater population on those asteroids can be measured. Fig. 2.6 shows the crater statistics for Gaspra from Chapman et al. (1996) (their Table I) for smaller craters and from Greenberg et al. (1994) for large craters; for Ida from Belton et al. (1994) (their Fig. 5b) and Chapman et al. (1996) (their Table II); for Mathilde from Chapman et al. (1999)

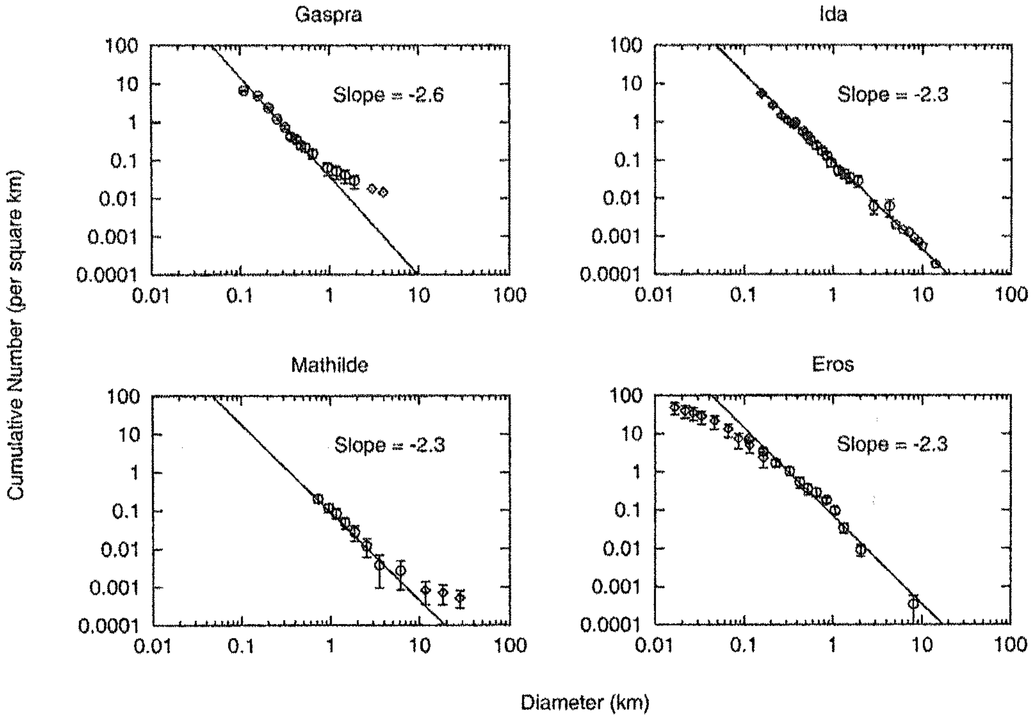

Figure 2.6: Crater populations on asteroids observed by spacecraft. Data is from Chapman et al. (1996) and Greenberg et al. (1994) for Gaspra, Belton et al. (1994) and Chapman et al. (1996) for Ida, Chapman et al. (1999) for Mathilde, and Veverka et al. (2000) and Chapman et al. (2002) for Eros. We plot the original error bars when given in the original sources. For data that were published without error bars, we estimate them based on counting statistics and information given in the original source.

(their Fig. 3); and for Eros from Veverka et al. (2000) (their Fig. 10) and Chapman et al. (2002) (their Fig. 1). Cratering records on asteroids can be used to infer the impacting population (e.g. Greenberg et al. (1994) for Gaspra and Greenberg et al. (1996) for Ida), although given the uncertainty regarding details of impact effects, they do not necessarily yield a unique solution. Asteroid crater records serve as a constraint on the size distribution of asteroids at the very small end, down to about 10 m in diameter for Gaspra and Ida and less than 1 m for Eros.

2.2 Asteroid Strength

There are two generally used definitions of asteroid strength. Q_S is the amount of energy per unit mass of the target required to catastrophically fragment a body, leaving the largest fragment with half the mass of the target. Q_D^* is the amount of energy needed to fragment a body and disperse half of the mass. The notation used here was adopted at the 5th Workshop on Catastrophic Disruption in the Solar System (1998). For bodies smaller than $\sim$ 1 km, Q_S and Q_D^* are equal, since the gravitational binding energy is negligible. For larger targets, Q_D^* is larger than Q_S, since gravity can significantly impede the dispersal of fragments. In that case, Q_D^* is determined primarily by the mass (and hence gravitational field) of the target, the amount of collisional energy partitioned into the collisional fragments, and the mass-velocity relationship amongst the fragments.

Analytical scaling arguments, as well as numerical modeling and laboratory studies, have shown that material strength parameters vary with size. The strength (Q_S and Q_D^*) of asteroids $\lesssim$ 1 km in diameter decreases with increasing size due to a couple of factors (Farinella et al., 1982; Housen and Holsapple, 1990; Holsapple, 1994; Ryan and Melosh, 1998; Housen and Holsapple, 1999; Benz and Asphaug, 1999). The flaw distribution within a material is conventionally given as a Weibull distribution

$$n(\epsilon) = k_w \epsilon^{m_w}, \tag{2.2}$$

where ϵ is the strain, $n(\epsilon)$ is the number density of flaws that have failure strains less than ϵ, and k_w and m_w are positive, material-dependent constants (Jaeger and Cook, 1969). Because larger bodies contain more flaws than smaller bodies, the weakest flaw in a large body is likely to be weaker than the weakest flaw in a smaller body. The weakest flaw dominates the fracture process, so larger bodies are generally weaker than smaller bodies (Fujiwara, 1980). Second, since a large projectile will apply a load to the target for a longer period of time than a smaller projectile, larger projectiles will give those flaws activated by the impact more time to propagate, coalesce, and cause widespread fragmentation (Housen and Holsapple, 1990). The result of these effects is that as the target size increases, the projectile size necessary for fragmentation, as a fraction of the target size, decreases. Thus the strength parameters Q_S and Q_D^* decrease with increasing size. We refer to the portion of the population where this relationship holds (diameter $\lesssim$ 1 km) as the 'strength-scaled regime.' Q_S and Q_D^* are equal in this regime, because, if a body fragments, the gravity is too weak to keep the pieces from escaping.

For asteroids $\gtrsim$ 1 km in diameter, gravity dominates the effective strength of the material. Q_S increases with increasing size because gravitational self-compression makes it more difficult to fragment a target (Davis et al., 1985; Housen and Holsapple, 1990; Housen, 1991; Ryan and Melosh, 1998). Q_D^* increases with increasing size because the stronger gravity of larger targets makes it more difficult to disperse collisional fragments (Davis et al., 1985; Petit and Farinella, 1993; Holsapple, 1994; Love and Ahrens, 1996; Melosh and Ryan, 1997; Benz and Asphaug, 1999). We refer to this portion of the population as the 'gravity-scaled regime.'

In addition to varying with size of the target, Q_S and Q_D^* also vary with the impact angle relative to the target's surface. Most laboratory experiments and numerical models of catastrophic fragmentation and disruption assume head-on impacts, but in reality, impacts occur at all possible angles, from head-on to grazing. As shown in laboratory experiments (e.g. Fujiwara and Tsukamoto (1980)) and numerical hydrocode simulations (e.g. Benz and Asphaug (1999)), the values of Q_S and Q_D^* when averaged over all possible impact angles are about a factor of 3 larger than their values for head-on impacts, due to less efficient coupling of energy and momentum to the target.

Estimates of Q_S and Q_D^* are summarized in Figs. 2.7 and 2.8, respectively. At smaller sizes where gravity is not important, Q_S and Q_D^* are equal. At larger sizes, both Q_S and Q_D^* begin to increase with increasing size, but by definition Q_D^* is larger than Q_S, since it is easier to fragment a large body than it is to give those fragments enough energy to escape from one another to infinity. Note that in these plots, the curves for the Benz and Asphaug (1999) strength law lie above the others. These curves have a higher effective strength because the strength is averaged over all impact angles, whereas the other curves are all calculated for head-on impacts.

The parameter f_{KE} is the fraction of impact energy that is partitioned into fragment kinetic energy. A small f_{KE} implies that the fragments will be difficult to disperse (hence a large Q_D^*), while a large f_{KE} implies easier dispersal and a smaller Q_D^* (see, eg. Davis et al. (1989)). f_{KE} is likely size-dependent. For example, above $\sim$ 1 km in diameter, larger targets, which require a larger projectile/target mass ratio for fragmentation due to increasing Q_S with size, will have larger f_{KE} than smaller targets that have a smaller threshold projectile/target mass ratio (Davis et al., 1989; Melosh and Ryan, 1997). The opposite trend will hold for bodies smaller than $\sim$ 1 km in diameter, for which Q_S decreases with increasing size. This is because for small projectile/target mass ratios, energy is deposited very quickly in a very small spot, while for large projectile/target mass ratios, the energy is deposited in a larger volume of the target over a longer time. For large, 100 km-scale targets, f_{KE} can be larger than 0.1 and for small laboratory scale targets, it

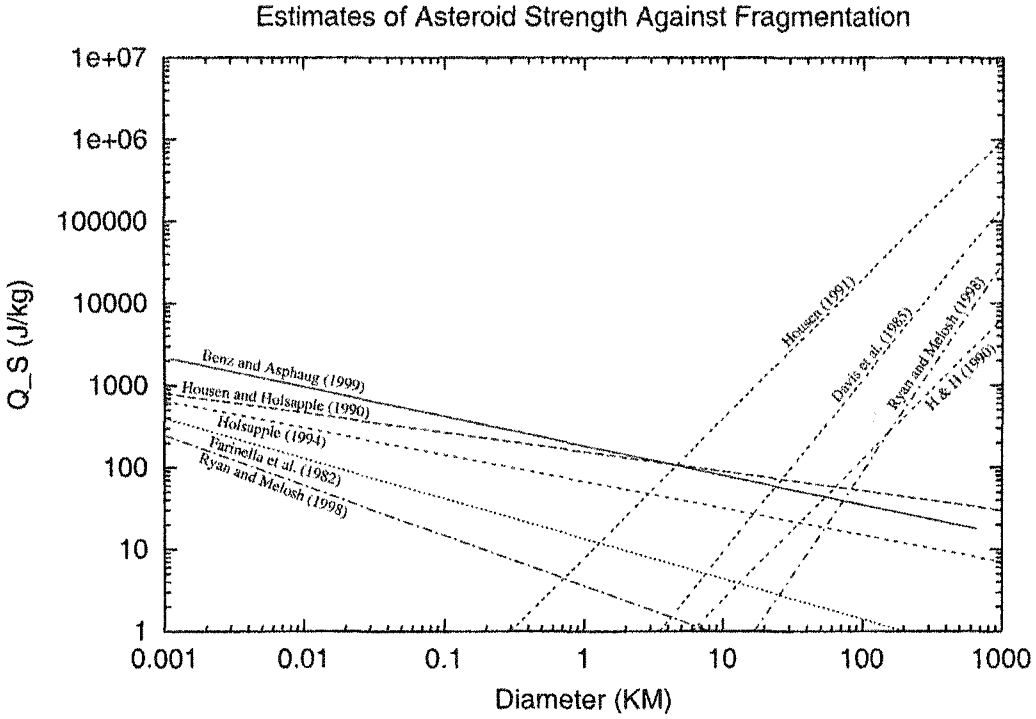

Figure 2.7: Estimates of the strength of asteroids against catastrophic fragmentation Q_S, defined as the amount of energy required to fragment a body such that the largest fragment contains half of the mass of the target.

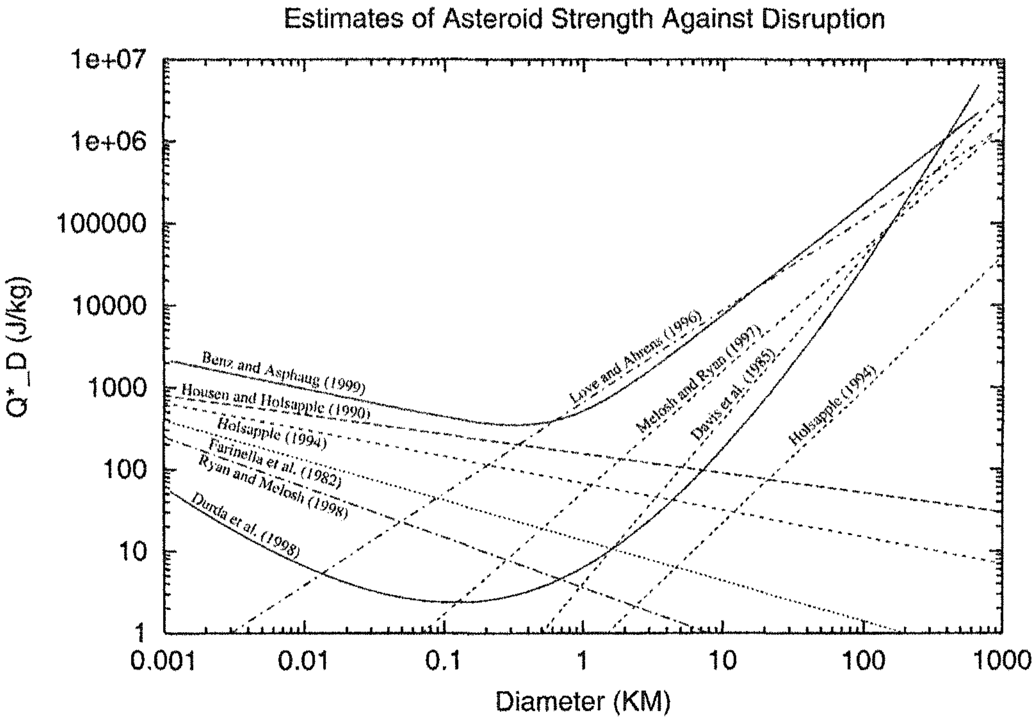

Figure 2.8: Estimates of the strength of asteroids against catastrophic disruption Q_D^*, defined as the amount of energy required to fragment a body and disperse half of its mass.

can be less than 0.01, but the exact values are not well constrained (Davis et al., 1989).

Some recent numerical collisional evolution models (e.g. Durda et al. (1998)) have used Q^*_D as the primary input parameter, as it encapsulates a large amount of collisional physics in a single parameter. The analytical model in Chapter 3 would not be possible without the simplification brought about by using Q^*_D. For numerical simulations, however, that simplification is not necessary, and we have found that using Q^*_D as the primary input parameter is probably an over-simplification. Q^*_D is indeed the primary factor determining the final evolved asteroid population, but as we will show, variations in Q_S and f_{KE}, even if Q^*_D remains the same, can affect the final collisionally evolved population. In fact, the observational constraints on the character of the asteroid population in Section 2.1 cannot be explained unless Q_S and f_{KE} vary in a specific way with size.

CHAPTER 3

Steady-State Size Distributions for Collisional Populations: Analytical Solution with Size-Dependent Strength

This chapter was originally published in *Icarus* as O'Brien and Greenberg (2003). Minor modifications have been made to the text for inclusion in this dissertation.

3.1 Introduction

To interpret the statistics of main-belt asteroids, Dohnanyi (1969) analytically modeled a population of self-similar bodies (same collisional response parameters, such as strength per unit mass) in a collisional cascade and found that the steady-state power-law index of the differential size distribution of such a population is 3.5. That model included debris from both cratering and catastrophic shattering events, but concluded that the effect of cratering debris is negligible. Greenberg and Nolan (1989) constructed a simple analytical model which includes only catastrophic fragmentation that also yields a steady-state population index of 3.5. The value of the population index, 3.5, is independent of many of the parameters describing the fragmentation process, such as the power-law index of the fragment distribution in a catastrophic collision. Even if the fragment distribution varies with impact energy, as is seen in laboratory and numerical experiments (i.e. more energetic collisions on a given body give a steeper fragment distribution), the steady-state population index remains 3.5 (Williams and Wetherill, 1994). Tanaka et al. (1996) showed this to be true for any fragmentation model that is independent of the size of the target. Thus, a value of 3.5 is frequently cited as the expected steady-state power-law index of a collisionally evolved population, such as the asteroid belt.

This value of the population index, however, is based on the assumption that bodies of every size have the same strength per unit mass. As described in Chapter 2, analytical scaling arguments (Davis et al., 1985; Farinella et al., 1982; Housen and Holsapple, 1990; Holsapple, 1994) as well as numerical modeling (Ryan and Melosh, 1998; Love and Ahrens, 1996; Melosh and Ryan, 1997; Benz and Asphaug, 1999) and laboratory studies (Housen and Holsapple, 1999) have shown that material strength is in fact a size-dependent property. For bodies $\lesssim 1$ km in diameter, material properties cause strength to decrease with increasing size. For larger bodies, strength increases with size due to gravitational self-compression and the gravitational reaccumulation of collisional fragments.

Numerical collisional evolution models have found that in general, the power-law index of the population is larger than 3.5 when strength decreases with increasing size and smaller than 3.5 when strength increases with increasing size, hence the small body population where material properties dominate the strength should be steeper than the large body population where gravity dominates (Durda, 1993; Davis et al., 1994; Durda and Dermott, 1997; Durda et al., 1998). In addition, all of these researchers found that the transition between these two different regimes creates waves that propagate through the large body size distribution.

Here we derive those results analytically. In Section 3.2, we derive an expression for the steady-state power-law index of a collisional population in which the material strength varies with size as a single power law and show that the canonical 3.5 value only holds for constant strength. In Section 3.3, we show that if the strength is described by a jointed power law (i.e. decreasing with size for small bodies and increasing with size for large bodies), the population indices in these two regimes are the same as would be calculated in the single-slope case—this result implies that, in terms of the population index, the large body population has no effect on the small body population and vice versa. We also confirm analytically that for the jointed power law case, waves are introduced in the large end of the population as perturbations about a power law, and we derive simple expressions for their amplitude and wavelength.

In Section 3.4, we compare the results of our analytical model with a numerical collisional evolution model and obtain excellent agreement. Finally, in Section 3.5 we use our analytical results to determine the strength law needed to fit the asteroid belt, and compare our results to results in the literature from collisional modeling, analytical theory, and experiments.

3.2 Single-Slope Collisional Model

First consider the steady-state of a colliding population of bodies whose strength is described by a single power law. The population is described by the power law

$$\mathrm{d}N = BD^{-p}\mathrm{d}D, \tag{3.1}$$

where $\mathrm{d}N$ is the incremental number of bodies in the interval $[D, D+\mathrm{d}D]$. Equation 3.1 is referred to as the differential or incremental size distribution. As there are more small bodies than large bodies, the coefficient B should technically be negative. However, in the context of an incremental size distribution, B is defined to be positive to avoid physically unrealistic notion of negative numbers of bodies in a given size interval. p is the power-law index of the population, or simply, the 'population index.' On a log-log plot, Eq. 3.1 would plot as a line with a slope of $-p$. For the Dohnanyi (1969) solution, $p = 3.5$. See Appendix A for how the differential size distribution is related other commonly used representations of the size distribution, such as the cumulative number distribution and the log-incremental distribution.

3.2.1 Collisional Destruction

The criterion for an impact to result in catastrophic disruption is conventionally parameterized by the the critical specific energy Q_D^*, which is defined as the minimum collisional energy per unit mass of the target to fragment the target and disperse half of its mass to infinity (this standard notation was adopted at the 5th Workshop on Catastrophic Disruption in the Solar System, 1998). By definition, an impact occurring with a specific energy of exactly Q_D^* will yield a largest remaining fragment that is a fraction $f_l = 0.5$ of the target mass. Impacts occurring with a specific energy greater than Q_D^* will give a smaller collisional remnant ($f_l < 0.5$). We assume that impacts occurring with a specific energy less than Q_D^* contribute relatively few collisional fragments, consistent with laboratory work indicating that there is a relatively abrupt transition between small crater formation and widespread target damage (Fujiwara et al., 1977). As shown by Dohnanyi (1969), cratering debris has a negligible effect on the steady-state size distribution.

Here we are concerned with defining the rate at which bodies of diameter D are disrupted (in Section 3.2.2 we parameterize the size distribution of small bodies produced by such an event). The diameter D_{dis} of the smallest body that can catastrophically disrupt a target of diameter D can be found by equating the kinetic energy of the projectile to the total energy required for disruption (assuming the same density of projectile and target):

$$\frac{1}{2}\left(\frac{4}{3}\pi\left(\frac{D_{dis}}{2}\right)^3\rho\right)V^2 = \frac{4}{3}\pi\left(\frac{D}{2}\right)^3\rho Q_D^*, \qquad (3.2)$$

where the average collision velocity V is assumed to be independent of size. This yields the relation

$$D_{dis} = \left(\frac{2Q^*_D}{V^2}\right)^{\frac{1}{3}} D. \tag{3.3}$$

Here we consider the case where the impact strength Q^*_D is given by a power law:

$$Q^*_D = Q_o D^s, \tag{3.4}$$

where Q_o is a normalization constant and s is the slope of Eq. 3.4 on a log-log plot. Inserting Q^*_D from Eq. 3.4 into Eq. 3.3 gives

$$D_{dis} = k_{dis} D^{\frac{3+s}{3}}, \tag{3.5}$$

where the constant k_{dis} depends on fixed parameters:

$$k_{dis} = \left(\frac{2Q_o}{V^2}\right)^{\frac{1}{3}}. \tag{3.6}$$

The rate of destruction of targets of a given size range $[D, D + \mathrm{d}D]$ is proportional to the number of disruptors (bodies larger than D_{dis}) times the cross sectional area of the target ($\propto D^2$) times the number of targets $\mathrm{d}N$

$$\left(\frac{\mathrm{d}(\mathrm{d}N)}{\mathrm{d}t}\right)_{dest} \propto -N_{>D_{dis}} D^2 \mathrm{d}N. \tag{3.7}$$

The number of disruptors (bodies greater than or equal to the minimum disruptor size) is given by integrating over the population (Eq. 3.1) for all bodies with a diameter equal to or larger than D_{dis} (given by Eq. 3.5). Because D_{dis} is always much smaller than the target, and hence much smaller than the largest asteroid, we can integrate to ∞ without significantly affecting the result, so long as $p > 1$ (i.e. there are more smaller bodies than larger bodies), which is always the case:

$$N_{>D_{dis}} = \int_{D_{dis}}^{\infty} BD'^{-p}\mathrm{d}D' = \frac{B\left(k_{dis}D^{\frac{3+s}{3}}\right)^{1-p}}{p-1}. \tag{3.8}$$

Inserting Eq. 3.8 into Eq. 3.7 gives

$$\left(\frac{\mathrm{d}(\mathrm{d}N)}{\mathrm{d}t}\right)_{dest} \propto -D^{\frac{3+s}{3}(1-p)}D^2\mathrm{d}N \propto -D^{\frac{9-ps-3p+s}{3}}\mathrm{d}N, \tag{3.9}$$

which can be written as

$$\left(\frac{\mathrm{d}(\mathrm{d}N)}{\mathrm{d}t}\right)_{dest} = -\frac{\mathrm{d}N}{\tau}, \tag{3.10}$$

where τ is the mean collisional lifetime of bodies of diameter D:

$$\tau = KD^{\frac{3p-s+ps-9}{3}} \tag{3.11}$$

and K is a constant of proportionality. Inserting τ and dN (from Eqns. 3.11 and 3.1) into the right hand side of Eq. 3.10 gives the collisional removal rate for bodies of diameter D:

$$\left(\frac{\mathrm{d}(\mathrm{d}N)}{\mathrm{d}t}\right)_{dest} = -\frac{BD^{-p}\mathrm{d}D}{KD^{\frac{3p-s+ps-9}{3}}} = -\frac{B}{K}D^{3-2p-\frac{s(p-1)}{3}}\mathrm{d}D. \tag{3.12}$$

3.2.2 Collisional Production

The size distribution of the fragments produced by the catastrophic disruption of a target of size D_o can be described by a power law of similar form to Eq. 3.1 but with a different power-law index q (Greenberg et al., 1978; Greenberg and Nolan, 1989):

$$\mathrm{d}N = CD^{-q}\mathrm{d}D. \tag{3.13}$$

The actual size distribution of fragments may be more complex than this (eg. Petit and Farinella (1993) and Chapter 6 of this dissertation), but Eq. 3.13 is a fairly good approximation, especially for impacts between bodies that are small enough that the gravitational reaccumulation of fragments is negligible. If the diameter of the largest fragment is bD_o (where b is related to the fractional mass of the largest fragment f_l by $b = f_l^{1/3}$), the normalization constant C is found by requiring the cumulative number of fragments equal to or larger than bD_o to be 1:

$$\int_{bD_o}^{\infty} CD^{-q}\mathrm{d}D = 1, \tag{3.14}$$

which yields

$$C = (q-1)(bD_o)^{q-1}. \tag{3.15}$$

Eq. 3.15 shows that the value of the coefficient C depends strongly on the size of the largest fragment bD_o, and hence on b. What value of b should we adopt? Impacts with barely enough energy to disrupt the target yield $b = (1/2)^{1/3}$. Because the impactor population is a steep power law, most impactors are not much larger than the critical size D_{dis}, but the population of impactors does include larger projectiles that can yield debris with much smaller b for the same target size. Thus the effective 'typical' value of b for any target size is difficult to determine. Here we simply assume that whatever the effective value of b is, it is independent of D_o. We will ultimately show (Section 3.2.3) that our results are independent of the actual value of the effective b, as long as b is independent of D_o.

The relation between the power-law index q of the fragment size distribution and the fractional size b of the largest fragment is found by equating the volume of fragments to the volume of the parent body, where the number of fragments $\mathrm{d}N$ of diameter D is given by Eq. 3.13. The minimum diameter of the fragments is taken to be zero, and the maximum diameter is bD_o, which is by definition the largest fragment produced. We assume here that q is less than 4 so that the total mass of the fragments is finite even though we integrate from $D = 0$. Thus,

$$\begin{aligned} \frac{4}{3}\pi\left(\frac{D_o}{2}\right)^3 &= \int_0^{bD_o} \frac{4}{3}\pi\left(\frac{D}{2}\right)^3 \mathrm{d}N \\ &= \int_0^{bD_o} \frac{4}{3}\pi\left(\frac{D}{2}\right)^3 (q-1)(bD_o)^{q-1}D^{-q}\mathrm{d}D. \end{aligned} \tag{3.16}$$

Integration yields

$$(q-1)(bD_o)^{q-1}\frac{(bD_o)^{4-q}}{4-q} = D_o^3. \tag{3.17}$$

D_o cancels out in Eq. 3.17. Solving Eq. 3.17 for q gives:

$$q = \frac{b^3+4}{b^3+1}, \tag{3.18}$$

just as found by Greenberg and Nolan (1989).

The production rate of fragments of a given diameter D due to the breakup of bodies of diameter D_o is given by the product of the number of fragments of diameter D produced by the breakup of a body of diameter D_o (Eq. 3.13, with C from Eq. 3.15) and the breakup rate of bodies of size D_o (Eq. 3.12)

$$\left(\frac{\mathrm{d}(\mathrm{d}N)}{\mathrm{d}t}\right)_{prod} = (q-1)(bD_o)^{q-1}D^{-q}\mathrm{d}D\frac{B}{K}D_o^{3-2p-\frac{s(p-1)}{3}}\mathrm{d}D_o. \tag{3.19}$$

The total production rate is then given by integrating Eq. 3.19 over all D_o that can produce fragments of size D. Since the largest fragment is given by bD_o, the smallest parent body capable of producing a fragment of diameter D has a diameter of D/b, so that this is the lower limit on the integration. It can be shown (using the relationship that will be given in Eq. 3.24) that the exponent of D_o in the following integral is less than -1 for all q less than 4. Since q must be less than 4 to prevent the total fragment mass from becoming infinite, this integral will always be finite and setting the upper integration limit to ∞ is essentially equivalent to setting it to the diameter of the largest body, as long as most bodies are much smaller than the largest body. Thus,

$$\begin{aligned}\left(\frac{\mathrm{d}(\mathrm{d}N)}{\mathrm{d}t}\right)_{prod} &= (q-1)\frac{B}{K}b^{q-1}D^{-q}\mathrm{d}D\int_{\frac{D}{b}}^{\infty} D_o^{q+2-2p-\frac{s(p-1)}{3}}\mathrm{d}D_o \\ &= \frac{B}{K}\frac{(1-q)}{q+3-2p-\frac{s(p-1)}{3}}b^{2p-4+\frac{s(p-1)}{3}}D^{3-2p-\frac{s(p-1)}{3}}\mathrm{d}D. \qquad (3.20)\end{aligned}$$

3.2.3 Collisional Steady State

In a steady state, the rate of destruction (Eq. 3.12) of bodies of diameter D matches the rate of production (Eq. 3.20) of bodies of diameter D:

$$\frac{B}{K}D^{3-2p-\frac{s(p-1)}{3}} = \frac{B}{K}\frac{(1-q)}{q+3-2p-\frac{s(p-1)}{3}}b^{2p-4+\frac{s(p-1)}{3}}D^{3-2p-\frac{s(p-1)}{3}}. \qquad (3.21)$$

B, K, and D cancel, leaving

$$\frac{(1-q)}{q+3-2p-\frac{s(p-1)}{3}}b^{2p-4+\frac{s(p-1)}{3}} = 1. \qquad (3.22)$$

Rearranging Eq. 3.22 to put p on the left (except where it appears in an exponent), and using Eq. 3.18 to eliminate q gives

$$p = \frac{3}{2+\frac{s}{3}} + \frac{\frac{b^3+4}{b^3+1}}{2+\frac{s}{3}} + \frac{s}{6+s} + \left(\frac{b^3+4}{b^3+1} - 1\right)\frac{b^{2p-4+\frac{s(p-1)}{3}}}{2+\frac{s}{3}}. \tag{3.23}$$

The form of this equation precludes standard algebraic solution techniques for p, which is the steady-state power-law index of the population. However, by inspection we find that Eq. 3.23 is satisfied by

$$p = \frac{7+\frac{s}{3}}{2+\frac{s}{3}}. \tag{3.24}$$

The population index p is independent of b, indicating that the exact nature of the fragmentation process has little effect on the final collisionally evolved population. For $s = 0$, which corresponds to size-independent strength Q^*_D, this gives the classical Dohnanyi steady-state solution of $p = 3.5$. However, if the strength Q^*_D varies with size ($s \neq 0$), p can differ significantly from the Dohnanyi steady-state result, with $p > 3.5$ for $s < 0$ and $p < 3.5$ for $s > 0$. We show in the following section that Eq. 3.24 is a unique solution to Eq. 3.23.

3.2.4 Proof of Uniqueness of Analytical Solution

Here we show that the relation between p and s derived in Sec. 3.2.3 is a unique solution to Eq. 3.23, the equation for a collisional steady state. Equation 3.23 can be rewritten by grouping the terms that do not depend on p into constants C_1 through C_4

$$p = C_1 + C_2 b^{C_3 p - C_4}, \tag{3.25}$$

where

$$\begin{aligned} C_1 &= \frac{3}{2+\frac{s}{3}} + \frac{\frac{b^3+4}{b^3+1}}{2+\frac{s}{3}} + \frac{s}{6+s} \\ C_2 &= \frac{\frac{b^3+4}{b^3+1}-1}{2+\frac{s}{3}} \\ C_3 &= 2+\frac{s}{3} \\ C_4 &= -4-\frac{s}{3}. \end{aligned} \tag{3.26}$$

The left hand side of Eq. 3.25 is a monotonically increasing function of p. Since b (the fractional diameter of the largest fragment) is always between 0 and 1, and the constants C_2 and C_3 are positive for $s > -6$ (where s is unlikely to be much less than -1), the right hand side is a monotonically decreasing function of p (regardless of the sign of C_1 and C_4). Since a monotonically increasing function and a monotonically decreasing function can only intersect at a single point, Eq. 3.24 is the only solution to Eq. 3.23.

3.3 Two-Slope Collisional Model

So far we have only considered the case where a single power law describes the strength Q^*_D. However, as described in Chapter 2, over the size range of bodies in the asteroid belt (1000 km down to sub-meter sizes), material strength is generally believed to be controlled by different effects, depending on the portion of the size range. Asteroids with diameters $\lesssim$ 1 km in diameter are in the 'strength-scaled regime.' Larger asteroids are in the 'gravity-scaled regime.' In these two different regimes, two different power laws (Eq. 3.4) can approximate the Q^*_D vs. size relationship, each with its own slope s. In the strength-scaled regime, s is negative and in the gravity-scaled regime, s is positive. Various estimates of Q^*_D are shown in Fig. 2.8.

In this section, we address the expected size distribution for a population with strength Q_D^* following one power law with slope s_s ('strength-scaled') for bodies smaller than diameter D_t, connected to another power law with slope s_g ('gravity-scaled') for large bodies as shown in Fig. 3.1.

3.3.1 Gravity Scaled Portion of the Population

The gravity scaled portion of the population ($D > D_t$) is fed entirely by collisional fragments from larger bodies (in the gravity-scaled regime), and except for target bodies close to the transition diameter D_t, they are destroyed by bodies within the gravity regime as well. Because the gravity-scaled regime is approximately 'self-contained' in this manner, its population index p_g is simply given by the single-slope solution (Eq. 3.24), with subscript g added to indicate the gravity-scaled regime

$$p_g = \frac{7 + \frac{s_g}{3}}{2 + \frac{s_g}{3}}. \tag{3.27}$$

Since s_g is positive in the gravity-scaled regime, Eq. 3.27 yields a population index p_g less than 3.5 in the gravity-scaled regime

However, some targets in the gravity-scaled regime (those only slightly larger than D_t) will be destroyed by bodies in the strength-scaled regime, where the population may not follow the same power law as in the gravity-scaled regime. Those events will lead to perturbations to the gravity-scaled population. In Section 3.3.3, we show that these perturbations are wavelike oscillations about a power law with an index p_g given by Eq. 3.27, and these perturbations affect neither the destruction rate of bodies in the gravity-scaled regime nor the production rate of bodies smaller than D_t by bodies in the gravity-scaled regime. Therefore, even though the population in the gravity-scaled regime may be perturbed from a strict power law of index p_g, it still follows the general trend of a power law of index p_g and it still behaves (in terms of collisional production and destruction) as if it were

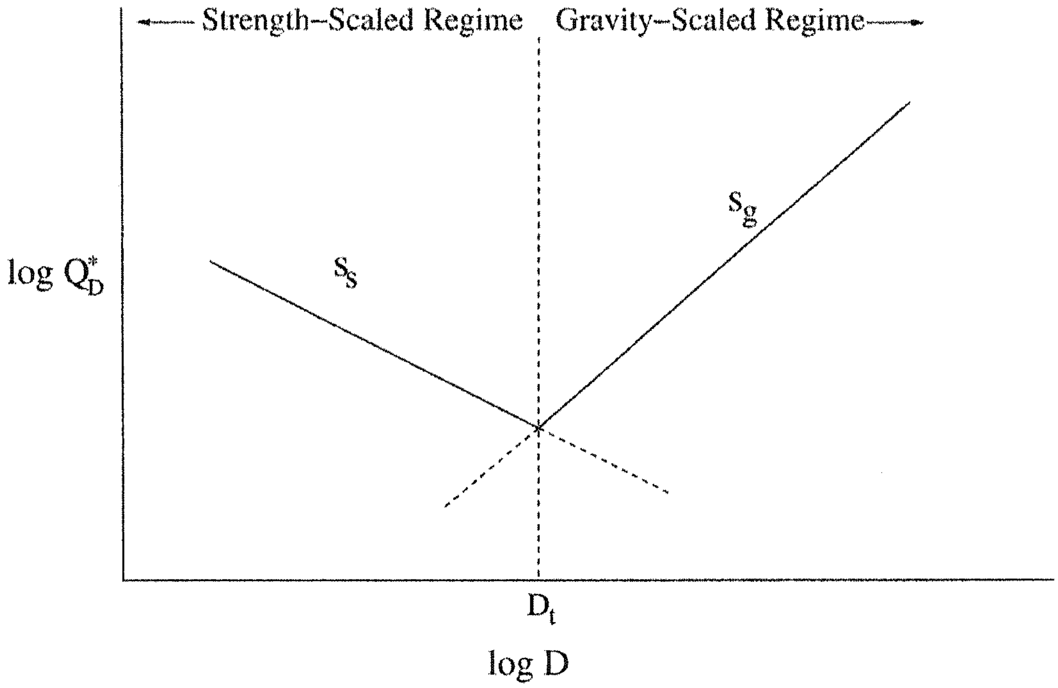
Strength–Scaled Regime
Gravity–Scaled Regime
log Q*D
Ss
Sg
Dt
log D

Figure 3.1: Hypothetical Q_D^* law for a population with different strength properties for large and small bodies (cf. Fig. 2.8). Q_D^* consists of two different power laws with slopes s_s and s_g joined at the transition diameter D_t. In the strength-scaled regime, material properties control the effective strength, while in the gravity-scaled regime, gravity dominates the effective strength through self-compression and gravitational reaccumulation of collisional fragments.

a power-law size distribution with index p_g.

3.3.2 Strength Scaled Portion of the Population

The strength-scaled portion of the population ($D < D_t$) is broken up almost exclusively by bodies within the strength-scaled regime, since the minimum sized impactor for disruption is generally much smaller than the target body in the asteroid belt and there are many more small bodies than large ones. However, the production of new bodies in the strength-scaled regime is due to the fragmentation of larger bodies in both the strength- and gravity-scaled regimes. We assume that strength-scaled portion of the population follows a power law with index p_s, which is likely to be different from the population index p_g in the gravity-scaled regime. Thus, we must explicitly account for the contribution of collisional fragments from both regimes. Equation 3.20 for the production rate of fragments in the single-slope case can be extended to treat a population described by 2 power laws:

$$\begin{aligned}\left(\frac{\mathrm{d}(\mathrm{d}N)}{\mathrm{d}t}\right)_{prod} &= (q-1)\frac{B_s}{K_s}b^{q-1}D^{-q}\mathrm{d}D\int_{\frac{D}{b}}^{D_t} D_o^{q+2-2p_s-\frac{s_s(p_s-1)}{3}}\mathrm{d}D_o \\ &+ (q-1)\frac{B_g}{K_g}b^{q-1}D^{-q}\mathrm{d}D\int_{D_t}^{\infty} D_o^{q+2-2p_g-\frac{s_g(p_g-1)}{3}}\mathrm{d}D_o. \quad (3.28)\end{aligned}$$

Here we ignore the deviation from a power law among bodies with $D > D_t$, which as noted in Section 3.3.1 will have a negligible effect on the production rate of bodies with $D < D_t$. Eq. 3.28 can be integrated and rearranged to give

$$\begin{aligned}\left(\frac{\mathrm{d}(\mathrm{d}N)}{\mathrm{d}t}\right)_{prod} &= \frac{B_s}{K_s}\frac{(1-q)}{q+3-2p_s-\frac{s_s(p_s-1)}{3}}b^{2p_s-4+\frac{s_s(p_s-1)}{3}}D^{3-2p_s-\frac{s_s(p_s-1)}{3}}\mathrm{d}D\\ &+ (1-q)b^{q-1}\left(\frac{D_t}{D}\right)^q\\ &\times \left[\frac{B_g}{K_g}\frac{D_t^{3-2p_g-\frac{s_g(p_g-1)}{3}}}{q+3-2p_g-\frac{s_g(p_g-1)}{3}}-\frac{B_s}{K_s}\frac{D_t^{3-2p_s-\frac{s_s(p_s-1)}{3}}}{q+3-2p_s-\frac{s_s(p_s-1)}{3}}\right]\mathrm{d}D. \qquad (3.29)\end{aligned}$$

A relation between B_s and B_g can be derived from the fact that the numbers of bodies must match at D_t. Following Eq. 3.1,

$$B_g D_t^{-p_g} = B_s D_t^{-p_s}. \qquad (3.30)$$

Similarly, the relation between K_s and K_g can be found by equating the lifetimes (Eq. 3.11) at D_t

$$K_g D_t^{\frac{3p_g-s_g+p_g s_g-9}{3}} = K_s D_t^{\frac{3p_s-s_s+p_s s_s-9}{3}}. \qquad (3.31)$$

Combining Eqns. 3.30 and 3.31 gives

$$\frac{B_g}{K_g} = \frac{B_s}{K_s} D_t^{2(p_g-p_s)-\frac{s_s p_s - s_g p_g}{3}-\frac{s_g-s_s}{3}}. \qquad (3.32)$$

Substituting Eq. 3.32 into Eq. 3.29 gives

$$\begin{aligned}\left(\frac{\mathrm{d}(\mathrm{d}N)}{\mathrm{d}t}\right)_{prod} &= \frac{B_s}{K_s}\frac{(1-q)}{q+3-2p_s-\frac{s_s(p_s-1)}{3}}b^{2p_s-4+\frac{s_s(p_s-1)}{3}}D^{3-2p_s-\frac{s_s(p_s-1)}{3}}\mathrm{d}D\\ &+ (1-q)b^{q-1}\left(\frac{D_t}{D}\right)^q \frac{B_s}{K_s} D_t^{3-2p_s-\frac{s_s(p_s-1)}{3}}\\ &\times \left[\frac{1}{q+3-2p_g-\frac{s_g(p_g-1)}{3}}-\frac{1}{q+3-2p_s-\frac{s_s(p_s-1)}{3}}\right]\mathrm{d}D. \qquad (3.33)\end{aligned}$$

In a steady state, the destruction rate must match the production rate. Equating the destruction rate of bodies in the strength-scaled regime (given by Eq. 3.12, with proper subscripts to indicate that all projectiles and targets are in the strength-scaled regime) with the production rate from Eq. 3.33 (by bodies in both the gravity-scaled and strength-scaled regimes) yields

$$\begin{aligned}\frac{B_s}{K_s} D^{3-2p_s-\frac{s_s(p_s-1)}{3}} &= \frac{B_s}{K_s} \frac{(1-q)}{q+3-2p_s-\frac{s_s(p_s-1)}{3}} b^{2p_s-4+\frac{s_s(p_s-1)}{3}} D^{3-2p_s-\frac{s_s(p_s-1)}{3}} \\ &+ (1-q)b^{q-1}\left(\frac{D_t}{D}\right)^q \frac{B_s}{K_s} D_t^{3-2p_s-\frac{s_s(p_s-1)}{3}} \\ &\times \left[\frac{1}{q+3-2p_g-\frac{s_g(p_g-1)}{3}} - \frac{1}{q+3-2p_s-\frac{s_s(p_s-1)}{3}}\right]. \end{aligned} \tag{3.34}$$

Note that the left hand side and the first term on the right hand side of Eq. 3.34 have the same form as the single-slope expression (Eq. 3.21). The last term depends on both p_s and p_g, and accounts for the fact that the population index p_g in the gravity-scaled regime (given by Eq. 3.27) likely differs from the population index p_s in the strength-scaled regime, and this may affect the production rate. Eq. 3.34 relates p_s, the slope of the population smaller than D_t, to known quantities. The form of Eq. 3.34 precludes a simple algebraic solution. However, note that when we insert p_g from Eq. 3.27, the last term goes to zero if

$$p_s = \frac{7+\frac{s_s}{3}}{2+\frac{s_s}{3}}. \tag{3.35}$$

Moreover, this solution makes the left hand side of Eq. 3.34 match the first term on the right hand side, solving Eq. 3.34 entirely. Since s_s is negative in the strength-scaled regime, Eq. 3.35 yields a population index p_s greater than 3.5 in the strength-scaled regime.

This result shows that the population index in the strength-scaled regime

(Eq. 3.35) is completely independent of the population index and the slope s_g of Q_D^* in the gravity-scaled regime, and indeed has the same form as the solution for a case where strength Q_D^* follows a single power law (Eq. 3.24). Evidently, the production rate of bodies in a colliding population is unaffected by a change in power-law index of that population at larger sizes. This result can be understood as follows: Even though the population index in the gravity-scaled regime is smaller (i.e. the population has a shallower slope) than in the strength-scaled regime and would therefore contain a relatively larger number of bodies than would be predicted if strength-scaling continued to large sizes, the increased strength of bodies in the gravity-scaled regime exactly offsets these increased numbers, such that the total breakup rate of bodies of a given size (and hence the fragment production rate by bodies of a given size) is not affected. For that reason, the last term in Eq. 3.34 goes to zero and the solution for p_s (Eq. 3.35) is independent of p_g and s_g.

3.3.3 Waves in the Size Distribution

The population indices of the two portions of the size distribution (larger and smaller than D_t) are independent of one another, as shown in Sections 3.3.1 and 3.3.2 respectively. In each regime, the index p depends only on the slope s of the Q_D^* law describing the strength for that size range. However, as noted in Section 3.3.1, effects of the transition in strength and population index near D_t introduces some deviation from a strict power law for bodies larger than D_t. In this section, we quantify this deviation and show that it does not affect the general population index p_g in this regime, nor does it have significant effect on the population index for smaller bodies.

In the derivation of the population index p_g in the gravity-scaled regime (Section 3.3.1), we assumed that all asteroids were disrupted by projectiles whose numbers were described by the same power law. However, for those targets just larger than D_t (i.e. near the small end of the gravity-scaled regime), projectiles are mostly smaller than D_t, and hence are governed by the strength-scaled size distribution. Consider the two steady-state power laws describing the population in the strength- and gravity-scaled regimes, joined at the transition diameter D_t (Fig. 3.2a). Let $D_{t_{dis}}$ be the diameter of the body that can disrupt a body of diameter D_t. Due to the transition from the gravity-scaled regime to the strength-scaled regime below D_t, bodies of diameter $D_{t_{dis}}$ are more numerous than would be expected by assuming that all bodies are gravity scaled, leading to a configuration that is not in a steady state.

A steady-state configuration can be achieved by 'sliding' the population in the strength-scaled regime down in number, as shown in Fig. 3.2b. To determine the magnitude of the shift, consider the production and destruction rates of bodies of diameter D_t. Since the destruction rate is proportional to the number of projectiles (Eq. 3.7), an excess $\Delta \log N(D_{t_{dis}})$ of bodies of diameter $D_{t_{dis}}$ that are capable of destroying bodies of diameter D_t causes a proportional increase in the destruction rate of bodies of diameter D_t. However, since the destruction rate is also proportional to the number of targets (Eq. 3.7), a decrease $\Delta \log N(D_t)$ of bodies of diameter D_t results in a proportional decrease in the destruction rate of bodies of diameter D_t. We assume here that the production rate of bodies of diameter D_t stays constant, despite these changes (this was noted in Section 3.3.1, and will be shown to be true later in this section). In a steady-state, the destruction rate of bodies of diameter D_t is equal to the production rate. With the excess $\Delta \log N(D_{t_{dis}})$ of projectiles and the depletion $\Delta \log N(D_t)$ of targets, the destruction rate of bodies of diameter D_t is related to the production rate by

$$\begin{aligned} \log\left(\frac{\mathrm{d}(\mathrm{d}N(D_t))}{\mathrm{d}t}\right)_{dest} &= \log\left(\frac{\mathrm{d}(\mathrm{d}N(D_t))}{\mathrm{d}t}\right)_{prod} \\ &+ \Delta \log N(D_{t_{dis}}) + \Delta \log N(D_t). \end{aligned} \tag{3.36}$$

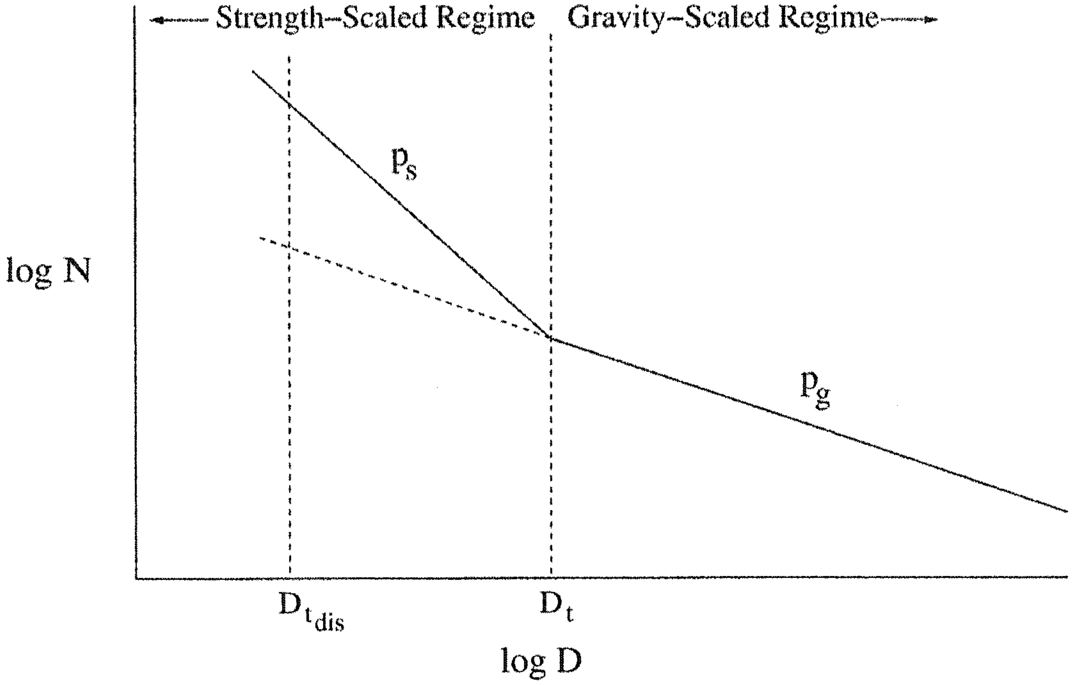
← Strength–Scaled Regime
Gravity–Scaled Regime →
log N
p_s
p_g
$D_{t_{dis}}$
D_t
log D

Figure 3.2a: Beginning of a sequence of figure showing how waves form in the population as a result of a change in strength properties at D_t. For a Q^*_D law such as that shown in Fig. 3.1, the resulting steady-state population is steeper for smaller, strength-scaled bodies (population index p_s) than for larger, gravity-scaled bodies (population index p_g). Thus, impactors capable of destroying bodies of diameter D_t are overabundant relative to what would be expected by extrapolating the gravity regime slope. This configuration is not in a collisional steady state.

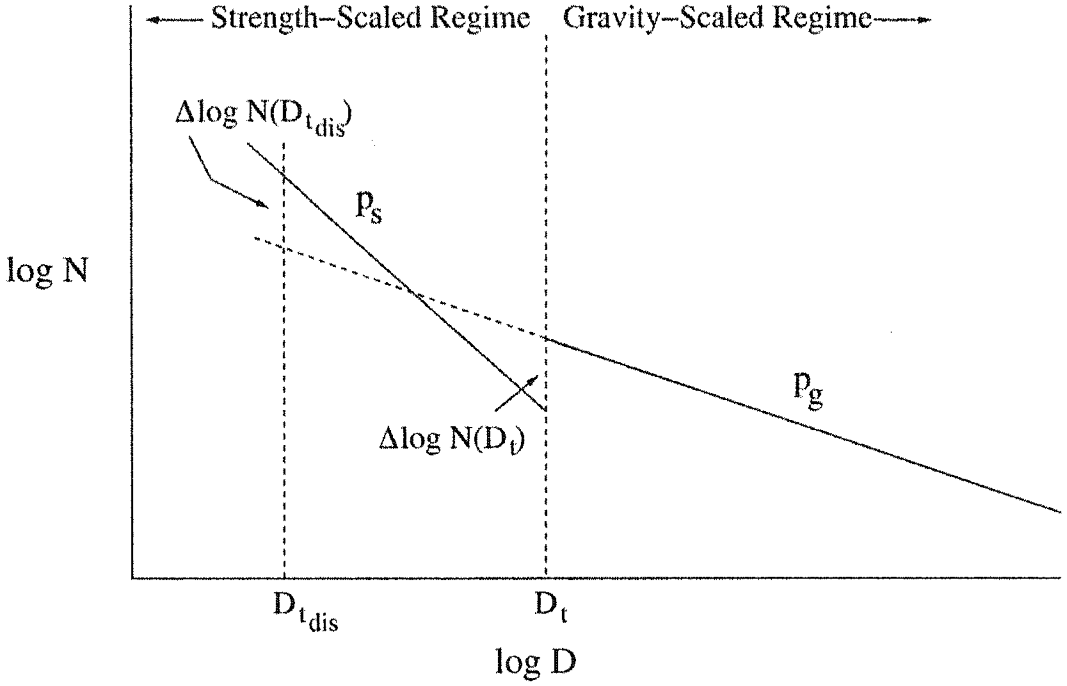
← Strength–Scaled Regime
Gravity–Scaled Regime →
Δlog N(D_{t_dis})
p_s
log N
Δlog N(D_t)
p_g
D_{t_dis}
D_t
log D

Figure 3.2b: To counteract the overabundance of impactors, the number of bodies of diameter D_t and smaller decreases by a factor $\Delta \log N(D_t)$ so that there are fewer 'targets' of diameter D_t and fewer impactors of diameter $D_{t_{dis}}$.

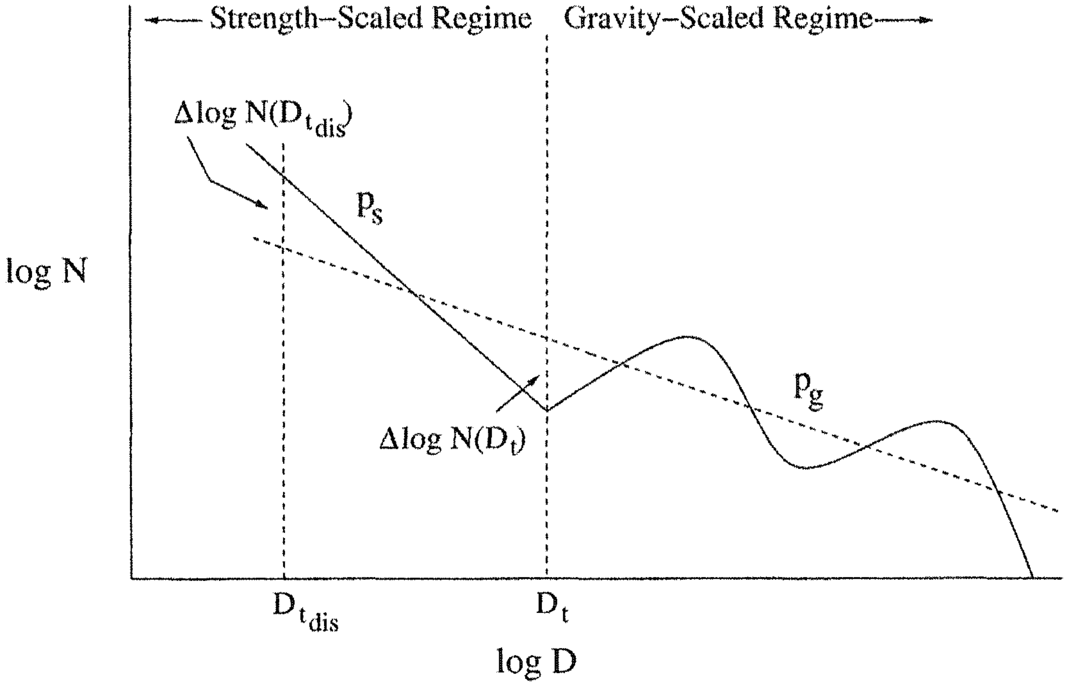
Strength–Scaled Regime
Gravity–Scaled Regime
log N
Δlog N(D_tdis)
p_s
p_g
Δlog N(D_t)
D_tdis
D_t
log D

Figure 3.2c: The decrease in bodies of diameter D_t leads to an overabundance of bodies that can be destroyed by impactors of diameter D_t, which in turn leads to a depletion of larger bodies and so on. Thus, a wave is formed in the large-body population.

From the previous equation, the production and destruction rates are equal (and the system is in a true steady state) when $\Delta \log N(D_{t_{dis}})$ and $\Delta \log N(D_t)$ are equal and opposite, as shown in Fig. 3.2b. To calculate the magnitude of the shift $\Delta \log N(D_t)$, we first find the logarithmic difference between D_t and $D_{t_{dis}}$ (using Eq. 3.3):

$$\Delta \log D = \log D_t - \log D_{t_{dis}} = -\frac{1}{3} \log \left(\frac{2Q_t}{V^2} \right), \tag{3.37}$$

where $Q_t = Q_D^*(D_t)$. Using Eq. 3.37 and the difference between the two population indices p_s and p_g, we calculate

$$\Delta \log N(D_t) = \frac{1}{6} \log \left(\frac{2Q_t}{V^2} \right) (p_s - p_g). \tag{3.38}$$

In reality, the shift in number of bodies at D_t given by Eq. 3.38 does not result in a simple discontinuity as shown in Fig. 3.2b, but instead causes perturbations to the size distribution in the gravity-scaled regime ($D > D_t$). The under-abundance $\Delta \log N(D_t)$ of bodies of diameter D_t (a 'valley') leads to an overabundance of bodies that impactors of diameter D_t are capable of destroying (a 'peak'), which in turn leads to another 'valley' and so on. This results in a wave of amplitude $|\Delta \log N(D_t)|$ that propagates through the large body size distribution as shown in Fig. 3.2c.

The average power-law index p_g of the population in the gravity-scaled regime will not be significantly changed by the initiation of this wave. A 'peak' in the wave will have $|\Delta \log N(D_t)|$ more bodies relative to a straight power law, but the following valley will have $|\Delta \log N(D_t)|$ fewer bodies than a straight power law and so on—the wave oscillates about a power law of slope p_g (given by Eq. 3.27). Likewise, the production rate of smaller bodies ($D < D_t$) by bodies in the gravity-scaled regime will not be significantly affected by the wave. While a 'peak' in the wave may have $|\Delta \log N(D_t)|$ more target bodies than expected from the power-law case, the bodies capable of disrupting those target bodies lie in a 'valley' and are hence lower in number by a factor of $|\Delta \log N(D_t)|$. The increase in number of targets is offset by a decrease in the number of impactors, such that the breakup rate and hence the fragment production rate is unchanged. The opposite is true as well. Bodies that lie in a 'valley' are catastrophically disrupted by bodies at a 'peak'. The end result is that the waviness induced in the gravity-scaled portion of the size distribution does not change the production rate of smaller bodies.

The position of the peaks and valleys of the wave can be found from Eqns. 3.5 and 3.6. Equation 3.6 is written in terms of the normalization constant Q_o, which in this case is the value Q_D^* would have at 1 m or 1 km (depending on the units used for diameter) if it followed a single power law of slope s_g. Using Eq. 3.4, Q_o can be written in terms of the more intuitive values Q_t and D_t as $Q_o = Q_t D_t^{-s_g}$. Given the diameter D_v where there is a valley (such as at D_t), the peak that follows will be at the diameter D_p:

$$D_p = \left(\frac{2Q_t}{V^2}\right)^{-\frac{1}{3+s_g}} D_t^{\frac{s_g}{3+s_g}} D_v^{\frac{3}{3+s_g}}. \tag{3.39}$$

Conversely, when the diameter D_p where a peak occurs is known, the diameter D_v of the valley that follows is given by

$$D_v = \left(\frac{2Q_t}{V^2}\right)^{-\frac{1}{3+s_g}} D_t^{\frac{s_g}{3+s_g}} D_p^{\frac{3}{3+s_g}}. \tag{3.40}$$

Thus, with Eqns. 3.27 and 3.35 we can find the power law indices that describe the strength- and gravity-scaled portions of the population, and with Equations 3.38, 3.39, and 3.40 we can quantify the 'wavy' structure that is superimposed on the power law describing the gravity-scaled portion of the population.

3.4 Comparison to Numerical Results

In this section we compare our analytical results with numerical collisional evolution simulations. Our numerical model tracks a population binned in logarithmic intervals $\mathrm{d}\log D$ in diameter. The number of bodies in each bin is $\mathrm{d}N$. At each timestep, the minimum disruptor diameter D_{dis} for bodies in each bin is calculated by Eq. 3.3, assuming a Q_D^* law and a mean collision velocity (we use $V = 5300$ m/s, from Bottke and Greenberg (1993) and Bottke et al. (1994b)), but the results are not substantially different for values 20% larger or smaller than this). The lifetime of bodies in each bin is calculated by

$$\tau = \frac{4}{N(> D_{dis}) D^2 P_i}, \tag{3.41}$$

where P_i is the intrinsic collisional probability, which is approximately 3×10^{-18} km^{-2} yr for the asteroid belt (Farinella and Davis, 1992; Bottke and Greenberg, 1993; Bottke et al., 1994b; Durda and Dermott, 1997), and $N(> D_{dis})$ is calculated by summing over all bins equal in size to or larger than D_{dis}. The removal rate of bodies from each bin is then calculated from Eq. 3.10, and this is used to calculate the number of bodies removed from each bin during each timestep. For each body removed by catastrophic disruption, fragments are produced according to the distribution given by Eqns. 3.13 and 3.15, and this is used to determine the number of new fragments added to each bin during each timestep. Cratering debris is neglected in this model.

We first performed a series of numerical simulations to determine the variation of population index with the slope of the scaling law Q_D^*. We use an initial population with index 3.5 (the predicted Dohnanyi steady-state value), evolve it in time for 4.5 Gyr with strength law slope s ranging from -1 to 2, and measure the final power-law index p of the population. Fig. 3.3 shows the excellent agreement between our numerical results and the analytical relation given in Eq. 3.24. We performed similar simulations with initial populations having different power-law indices, and found that the results are essentially the same as those shown in Fig. 3.3 (i. e. the final population index does not depend on the starting index). Durda (1993) presented a figure similar to Fig. 3.3, derived entirely from numerical results, for s from -0.3 to 0.3, and a slightly revised figure appeared in Durda and Dermott (1997) in which a "second-order effect" (i.e. a somewhat nonlinear relationship between p and s) was noted. Our more extensive numerical results match those of Durda (1993) and Durda and Dermott (1997), and our analytical results confirm and explain their numerical results, including the second-order effects noted in Durda and Dermott (1997).

Next, we performed a series of simulations with jointed power laws describing the strength law Q^*_D in order to test our analytical predictions. Fig. 3.4 shows the results of such a simulation, comparing the initial population (with a power-law index of 3.5) and the final population 4.5 Gyr later. The curve labeled 'Strength+Gravity Scaling' is evolved with 2 power laws fit to the Benz and Asphaug (1999) Q^*_D scaling law ($s_s = -0.36$, $s_g = 1.36$, $D_t = 0.7\,\mathrm{km}$, and $Q_t = 200\ \mathrm{J/kg}$) (see Fig. 3.5), while the curve labeled 'All Gravity Scaled' has been evolved assuming that even for bodies smaller than D_t, Q^*_D follows a power law with $s_s = s_g = 1.36$. Note the waves that appear in the large body population when there is a transition in the slope of the Q^*_D scaling law. The population is binned and plotted in logarithmic intervals $\mathrm{d}\log D$, so the slopes on the plot are 1 larger than the exponent $-p$ in Eq. 3.1. Thus, for example, the Dohnanyi steady-state power-law index $p = 3.5$ would appear as a slope of -2.5 if plotted in Fig. 3.4 (the relation between the incremental and log-incremental distributions is presented in detail in Appendix A). When referring to our plot, we give the value of p to facilitate comparison to our analytical predictions.

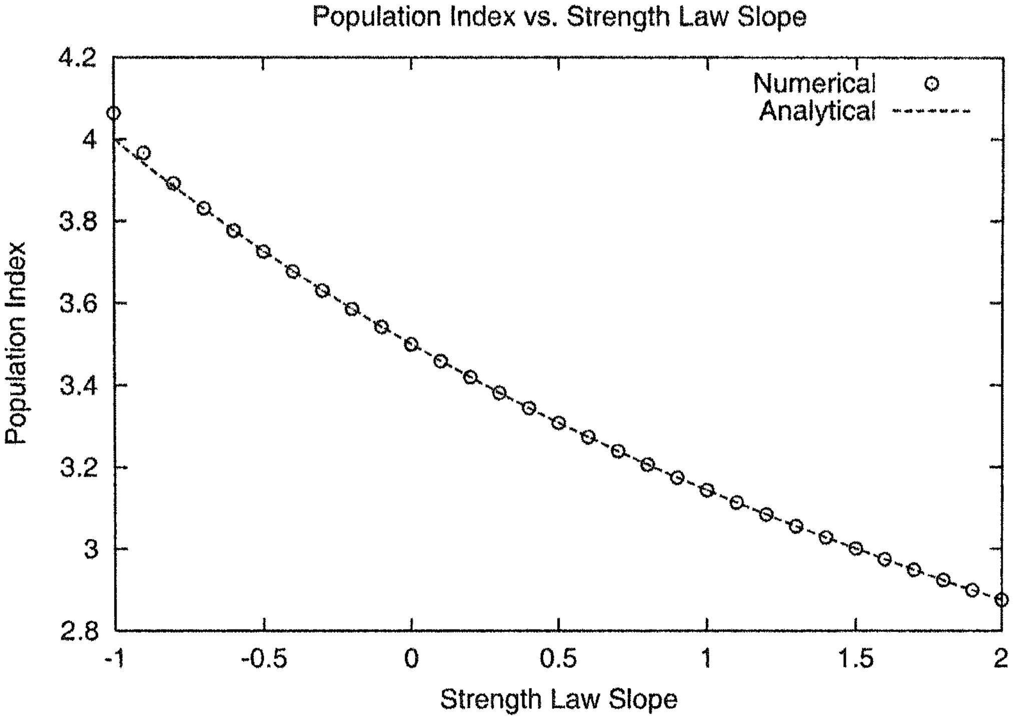

Figure 3.3: Comparison between our analytical relationship between the slope s of the strength law Q_D^* and the steady-state power-law index p of population (Eq. 3.24), and series of numerical simulations. The analytical relationship is shown as a solid line, and the results from numerical simulations are shown as open circles.

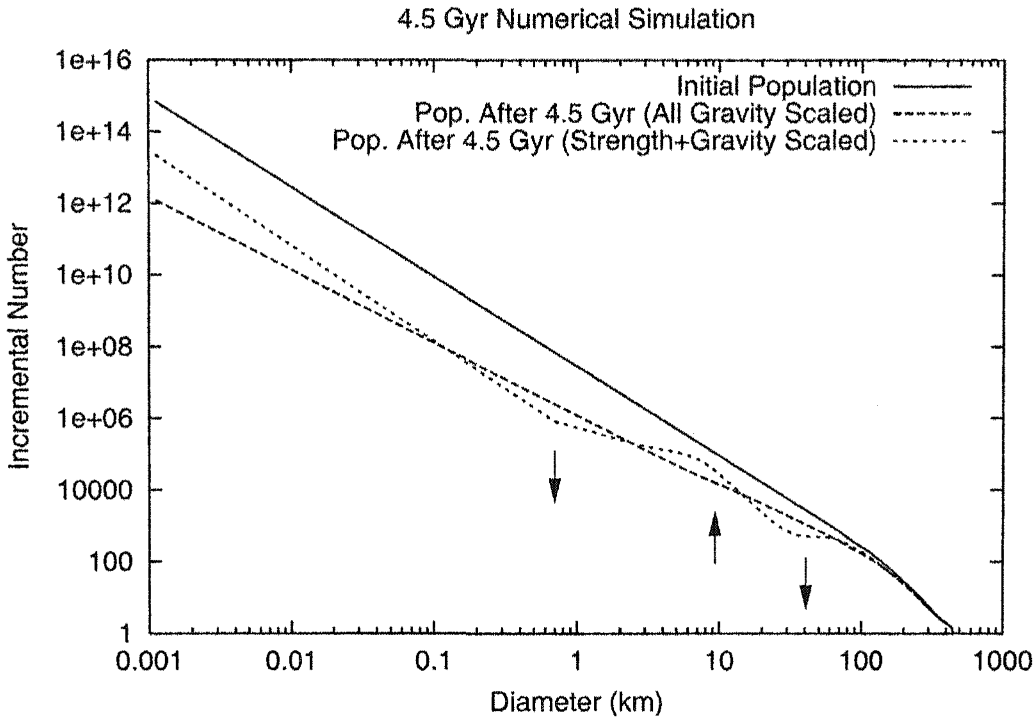

Figure 3.4: Results of a 4.5 Gyr numerical collisional evolution simulation. The solid line is the initial population, the long-dashed line is the final population assuming all bodies have a gravity-scaled Q^*_D, and the short-dashed line is the final population where small bodies have a strength-scaled Q^*_D and large bodies have a gravity-scaled Q^*_D. For the latter case, the transition between the two different strength regimes leads to 'waves' that propagate through the large-body population. Arrows show the positions of the 'peaks' and 'valleys' as predicted by Eqns. 3.39 and 3.40.

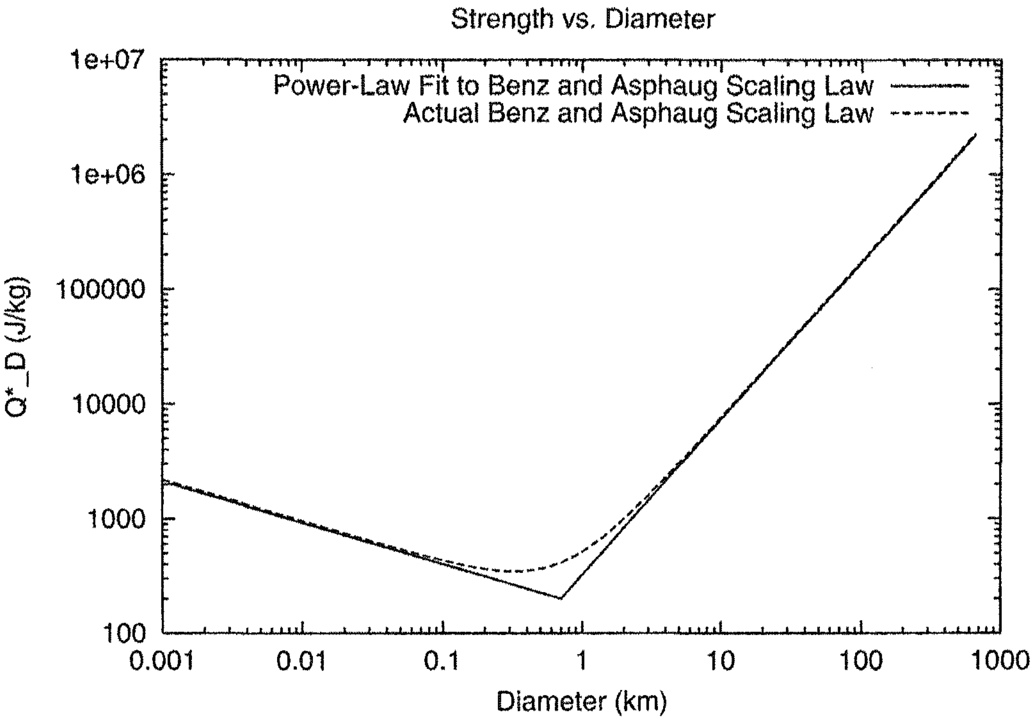

Figure 3.5: Q_D^* law used in the numerical simulation presented in Fig. 3.4, consisting of 2 power laws fit to the Benz and Asphaug (1999) law. The actual Benz and Asphaug (1999) Q_D^* is plotted for comparison. The sharply joined, 2 power-law fit is used in the simulations to make the positions of the peaks and valleys of the wave more clear.

The population evolved with pure gravity scaling has $p_g = 3.04$, which is exactly the value predicted by Eq. 3.27 for $s_g = -1.36$. However, there is some deviation from this slope for bodies $\gtrsim$ 10 km in diameter due to the fact that above $\sim$ 10 km, the mean collisional lifetimes of bodies begin to approach or exceed 4.5 Gyr and hence the population does not have enough time to reach a steady state. Running the simulation for longer times (20 Gyr and 100 Gyr) decreases this deviation but does not completely eliminate it, indicating that even after 100 Gyr, the largest bodies are not fully collisionally relaxed (i.e. not in a collisional steady state).

The exact size below which a collisional steady state is achieved after a given time depends on the specific strength law used. From a large number of numerical simulations performed for the work presented in Chapter 6, a general rule of thumb is that asteroids $\lesssim$ 1 km in diameter reach a collisional steady state within $\sim$ 100 Myr, asteroids $\lesssim$ 10 km in diameter will reach a collisional steady state over the lifetime of the solar system (4.5 Gyr), and bodies $\gtrsim$ 10 km in diameter may approach, but will not fully achieve, a collisional steady state over the age of the solar system.

For the population evolved with both strength and gravity scaling, the index of the strength-scaled portion of the population ($D < D_t$) is $p_s = 3.66$, which is exactly the value predicted by Eq. 3.35 for $s_s = 0.36$. The gravity-scaled portion of the population ($D > D_t$) is wavy, and oscillates about the population evolved with pure gravity scaling ($p_g = 3.04$). This example, along with other simulations we have performed, confirms our predictions that: (1) The population index in the strength-scaled regime is independent of the population index and Q_D^* law in the gravity-scaled regime, and (2) While the gravity-scaled portion of the population is wavy, it follows the general trend of a power law with index p_g that is independent of the population index and Q_D^* law in the strength-scaled regime.

The amplitude of the wave $|\Delta \log N(D_t)|$ in the simulation is found to be 0.48, which is very close to the value of 0.50 from Eq. 3.38. The wave amplitude decreases slightly for the following peak and valley, and there is effectively no peak formed around 100 km because the collisional lifetime of 100 km bodies is so large and there are few larger bodies to resupply new 100 km bodies by collisions. Arrows on Fig. 3.4 show the positions of the peaks and valleys predicted from Eqns. 3.39 and 3.40. The predicted positions overestimate the actual positions by about 30 percent.

When we run longer numerical simulations (20 Gyr and 100 Gyr), we find that there is still some variation in the amplitudes of the peaks and valleys (i.e. they are not all the same as $|\Delta \log N(D_t)|$). In addition, there is still some discrepancy between the predicted positions of the peaks and valleys and the actual positions. This is due in part to the fact that even after 100 Gyr, the largest bodies may not be fully collisionally relaxed. In addition, numerical modeling can more accurately simulate the collisional evolution process, uncovering second-order effects that our analytical model does not account for.

3.5 Summary and Implications

We have analytically derived the steady-state power-law index of a collisional cascade in which the material strength varies as a function of size. Earlier work had only treated collisions that are entirely self-similar, in which every body has the same strength per unit mass. Our results are applicable to actual collisional populations, such as the asteroid belt, where material strength has been shown to be strongly size-dependent.

For the case where a single power law describes the dependence of strength on size, we show that there is a simple analytical relation between the power-law slope s of the Q_D^* law describing the strength and the steady-state power-law index

p of the population (Eq. 3.24). For the self-similar case ($s = 0$), our result yields the classical Dohnanyi result of $p = 3.5$, but for other values of s, the steady-state population may have p quite different from 3.5.

For the case where large ('gravity-scaled') and small ('strength-scaled') bodies are controlled by different power-law expressions for Q_D^*, we find that the steady-state population index p_s in the strength-scaled regime is independent of the steady-state population index p_g and slope s_g of Q_D^* in the gravity-scaled regime and vice versa. The steady-state population index in both regimes can be described by the same relation as in the single-slope case (Eq. 3.24), with p_s depending only on s_s and p_g depending only on s_g. Thus, for a plausible Q_D^* law with $s_s = -0.36$ for bodies < 700 m in diameter and $s_g = 1.36$ for larger bodies (Benz and Asphaug, 1999), the population indices are $p_s = 3.66$ and $p_g = 3.04$. The transition between the different population indices in the strength- and gravity-scaled regimes leads to wavelike perturbations about a power law in the gravity-scaled regime. We have derived simple analytical expressions for the amplitude of these waves (Eq. 3.38) and the spacing of the peaks and valleys of the wave (Eq. 3.39 and 3.40). Our analytical results have been tested and validated by comparison with a numerical simulation.

Our analytical solution provides a tool for interpreting the size distribution of the asteroid belt in order to infer its strength properties. It should be noted, however, that effects not treated in our analytical solution could potentially alter the size distribution of asteroids and lead to discrepancies between our predictions and the actual strength properties of asteroids. For example, a small size cutoff in the size distribution due to Poynting-Robertson drag and solar radiation pressure can potentially introduce a wave in the size distribution (Durda, 1993; Campo Bagatin et al., 1994; Durda and Dermott, 1997). Such a wave would begin in the strength-scaled regime and could interfere constructively or destructively with the waves generated by the transition between strength- and gravity-scaled regimes.

The actual degree to which small particles are removed from the asteroid belt by the Poynting-Robertson effect and solar radiation pressure is not well known, and detailed analysis of such effects can only be done numerically—hence these effects are not treated here. In addition, the actual asteroid population may differ from our analytical predictions if the size distribution of collisional fragments differs significantly from the single power law assumed in Eq. 3.13 or depends significantly on the size of the target. These effects are difficult to model analytically, and hence are not treated here.

A number of recent estimates of the main belt population with $D > 1$ km have been published (Jedicke and Metcalfe, 1998; Ivezić et al., 2001), and cratering records on asteroids such as Gaspra, Ida, Mathilde, and Eros (Greenberg et al., 1994; Greenberg et al., 1996; Chapman et al., 1999; Chapman et al., 2002) can be used to estimate the population of asteroids down to a few meters. Thus, we have estimates of the asteroid size distribution in both the strength- and gravity-scaled regimes.

Greenberg *et al.* (1994, 1996) found that the crater population on both Gaspra and Ida was fit best by an impacting population that had a power-law index of $p = 4$ below 100 m in diameter. These bodies are small enough to be in the strength-scaled regime (Fig. 2.8). Using Eq. 3.35, we find that an index of $p = 4$ for the population implies a slope of $s = -1$ for the Q_D^* scaling law. This is significantly steeper than any predictions for the strength-scaled regime shown in Fig. 2.8, where the steepest predicted slope of the scaling law is $s = -0.61$, a value for weak mortar (Ryan and Melosh, 1998).

For larger asteroids ($3 < D < 30$ km), Jedicke and Metcalfe (1998) find that the population is very wavy and the population index varies significantly with absolute magnitude. These bodies are large enough to be in the gravity-scaled regime (Fig. 2.8). Using their Tables IV and VI, we find that the average value of the population index p_g is between 2.8 and 2.9, which, using Eq. 3.27, corresponds to a slope s_g between 1.9 and 2.3 for the Q^*_D scaling law. The values of s_g we find are consistent with the estimate of Davis et al. (1985) but somewhat steeper than the estimates of Holsapple (1994), Love and Ahrens (1996), Melosh and Ryan (1997) and Benz and Asphaug (1999) (see Fig. 2.8). Since the population in this size range is so wavy, it is possible that the average p_g we use would be different if we included data for larger or smaller bodies than those treated by Jedicke and Metcalfe (1998), hence our estimate of s_g could be skewed. Likewise, if the larger bodies (those around 30 km in diameter) observed by Jedicke and Metcalfe (1998) are not in a collisional steady state, this would also affect our estimate of s_g.

For the near-Earth asteroid (NEA) population, estimates are available down to around 10 m in diameter (Rabinowitz et al., 2000). However, as we discuss in the following chapter, the NEA size distribution is significantly influenced by size-dependent dynamical processes during the delivery of NEAs from the main belt. Inclusion of these dynamical processes in an analytical model is beyond the scope of this work. In Chapter 6 we develop a numerical model to treat the simultaneous collisional and dynamical evolution of the main belt and NEAs.

At the time this work was originally published, the size distribution of trans-Neptunian objects (TNOs) was not well determined below about 100 km in diameter. Recently, Bernstein et al. (2003) released the results of an HST survey of the trans-Neptunian region that extends the size distribution of TNOs down to approximately 10 km. That survey, and the application of this analytical model to it, are discussed in Chapter 8.

CHAPTER 4

Dynamical Link Between the Main Belt, Meteorites and NEAs

In this chapter we review the dynamics involved in the transport of bodies between the main-belt and NEA populations. In Section 4.1 we summarize the 'classical' scenario of the delivery of NEAs and meteorites and review the developments over the past decade that have led to the 'modern' scenario describing the dynamical link between NEAs, meteorites and the main belt. In section 4.2 we focus on the simulations of Bottke et al. (2000, 2002) and summarize the results from those simulations that serve as constraints and input parameters for our numerical simulations.

4.1 Development of the 'Modern' Delivery Scenario

Even before the discovery of the first asteroid, Chladni and Hoppe (1794) suggested that meteorites were of extraterrestrial origin. The similarities between NEAs and main-belt asteroids have been known since the discovery of Eros in 1898, but there was no known mechanism that could transfer bodies from the main belt to near-Earth space. The fact that the Kirkwood gaps in the asteroid belt (Kirkwood, 1867) correspond to mean-motion resonances with Jupiter and the ν_6 secular resonance with Saturn corresponds to the inner boundary of the main belt (Williams, 1969; Williams and Faulkner, 1981), as shown in Figs. 2.5a and 2.5b, indicates that material is probably being removed from the main belt by these resonances, but it was unclear exactly how it was removed, and how it could possibly be transported to near-Earth space. Until relatively recently, comets were seen as a much more likely source of NEAs, given that they were obviously able to reach near-Earth space (Wetherill, 1976).

Over the last 25 years, our understanding of the link between main-belt asteroids and near-Earth asteroids and meteorites has progressed significantly (see Morbidelli (1999) for a review). Wetherill (1979), reporting the work of J. G. Williams, first showed a potential link between the main belt and NEAs. This work showed that the ν_6 secular resonance with Saturn, which occurs when the precession rate ω of an asteroid's perihelion corresponds to the precession rate of Saturn's perihelion, is capable of boosting an asteroid's eccentricity to over 0.25 on timescales of a million years, allowing it to cross the orbit of Mars and be perturbed further into the terrestrial planet region. A few years later, Wisdom (1982, 1983) showed that the 3:1 mean-motion resonance with Jupiter could also perturb asteroids to Mars-crossing orbits on a million year timescale. For detailed reviews of the literature on mean-motion resonances, see Moons (1997), and for secular resonances, see Froeschle and Morbidelli (1994).

Several authors developed models based on these results in order to try and explain the distribution and statistics of the NEAs and the meteorites found on Earth (Greenberg and Chapman, 1983; Wetherill, 1979; Wetherill, 1985; Wetherill, 1987; Wetherill, 1988). For a review of these models, see Greenberg and Nolan (1989). The general idea behind these models is that asteroid collisions inject fragments into a resonance that increases their eccentricities to Mars-crossing or possibly Earth-crossing values. Subsequent encounters with terrestrial planets perturb these fragments out of resonance and cause them to evolve through the terrestrial planet region. The fragments 'die' within about 100 Myr by colliding with a terrestrial planet or being ejected on a Jupiter-crossing orbit.

This 'classical scenario' changed significantly with the availability of faster computers and the development of fast, efficient numerical integration algorithms, such as Wisdom and Holman's (1991) symplectic mapping algorithm, which has been modified to treat close encounters with planets in a widely used orbit integrator by Levison and Duncan (1994). Farinella et al. (1994), using an earlier code, showed that asteroids in the ν_6 and 3:1 resonances can have their eccentricities increased to the point that they collide with the Sun on million-year timescales. Gladman et al. (1997) studied a large number of test bodies in the ν_6, 3:1, and 5:2 resonances and found that they have a median dynamical lifetime[1] of only a few million years. Even the small fraction of bodies that are removed from the resonance and enter the terrestrial planet region have a maximum dynamical lifetime of only $\sim$ 10 Myr.

Applying the results of hundreds of numerical integrations to the problem of meteorite delivery to Earth, Morbidelli and Gladman (1998) found that the orbital distribution of fireballs observed by camera networks in the U.S. and Canada is consistent with the injection of asteroids into the ν_6 and 3:1 resonances. Their model also predicts a PM/AM ratio for meteorite falls, which is an indicator of how orbitally 'mature' the meteorites are (Greenberg and Nolan, 1989)—bodies just becoming capable of colliding with the Earth will have perihelia of 1 AU and will all hit the Earth on its trailing side (12:00 PM - 12:00 AM), while bodies that have evolved further will have a higher chance of colliding with the Earth between 12:00 AM - 12:00 PM. The PM/AM ratio predicted by Morbidelli and Gladman (1998) is 14% smaller than the observed value, which they argue is reasonable given the bias towards observing meteorite falls later in the day or evening.

A significant difference between the Morbidelli and Gladman (1998) model and observations is that the dynamical lifetimes of bodies in their model (a few Myr) are significantly shorter than the CRE ages of meteorites ($\sim$ 20 Myr for stones), implying that meteoroids must have spent most of their lifetimes in the main belt before entering a resonance. This rules out the direct injection of collisional fragments into a resonance as the primary source of meteoritic material.

The most plausible mechanism for allowing fragments to slowly drift into resonances, and accumulate cosmic ray exposure along the way, is the Yarkovsky effect. This effect was first described in a pamphlet written (and evidently lost, since no copies remain) by the Polish/Russian engineer I. O. Yarkovsky around 1900, and developed further by subsequent authors. The Yarkovsky effect is a force on a rotating body orbiting the Sun that is caused by a difference between the direction of absorption of sunlight and the direction of re-emission of thermal radiation. This force can cause a drift in semi-major axis, as well as changes in other orbital elements. Hartmann et al. (1999) give detailed review of the Yarkovsky effect literature and the history of its discovery, and Bottke et al. (2000) gives a good overview of its mathematical formulation.

---

[1] We use the term 'dynamical lifetime' to refer to the length of time for which a body survives before being eliminated, generally by collision with the Sun, collision with a terrestrial planet, or ejection from the inner solar system by an encounter with Jupiter.

The 'classical' effect originally described by Yarkovsky is now generally termed the 'diurnal' effect, and is due to the rotation of a body around its axis. It is maximum when the body's axis is perpendicular to its orbit (zero obliquity) and zero when its axis is parallel to its orbit (90° obliquity). The diurnal effect can cause the semimajor axis to change, with prograde rotation causing an increase and retrograde rotation causing a decrease. Another variant of the Yarkovsky effect, introduced much later by Rubincam (1995), is called the 'seasonal' effect, and is due to the orbit of a body around the sun. It is maximum at 90° obliquity and zero at zero obliquity, and always causes the semimajor axis to decay. In reality, these effects are end-members of a continuum—any real body will experience a Yarkovsky force that is due to both rotation and revolution around the sun, and which is not necessarily an additive combination of the diurnal and seasonal effect.

The Yarkovsky effect is size-dependent, losing effectiveness for bodies that are so small that they become isothermal, or for bodies so large that they are too massive to experience significant drift in semi-major axis. For regolith-free stony bodies, the diurnal effect peaks around 0.1 m or smaller in diameter (depending on the rotation rate) and the seasonal effect peaks around 10 m in diameter. The maximum semi-major axis drift rate $\dot{a}$ can be on the order of $\sim 10^{-3} - 10^{-2}$ AU/Myr for both the seasonal and the diurnal effects (assuming realistic rotation rates). The magnitude of the Yarkovsky effect depends on the thermal conductivity of asteroidal material, such that iron bodies, with high thermal conductivities, will have smaller $\dot{a}$ than stony bodies because they are less able to sustain a thermal asymmetry. The presence of an insulating regolith can also affect the Yarkovsky effect, generally diminishing the seasonal effect and accentuating the diurnal effect. In Chapter 5 we present a simple mathematical description of the Yarkovsky effect and illustrate in more detail the size-dependence of the Yarkovsky effect, its dependence on thermal parameters, and how it relates to the size-dependent removal rate of bodies from the main belt.

The Yarkovsky effect was mostly forgotten after its initial discovery, until it was reintroduced by Öpik (1951) and Radzievskii (1952). Öpik had seen Yarkovsky's pamphlet decades earlier and coined the name 'Yarkovsky Effect' in honor of its original discoverer. It re-appeared again several decades later in its application to the field of meteorite delivery with the work of Peterson (1976) and Rubincam (1995) (as well as a general review of radiation forces in the solar system by Burns et al. (1979)). Both Peterson and Rubincam discuss the fact that the Yarkovsky effect is stronger for stony bodies than iron bodies, and hinted that this may explain the much greater CRE ages of iron vs. stony meteorites—iron meteorites are stronger and drift more slowly in semimajor axis, such that they would be able to drift for longer times before reaching Earth. They generally assumed, however, that meteorites would drift all the way from the main belt to Earth, with only a small discussion of the action of resonances. Afonso et al. (1995) first modeled the dynamics resulting from the combined effects of resonances and the Yarkovsky effect, and demonstrated that the Yarkovsky effect could cause meteoroids to drift to a nearby strong resonance and be captured by it. The resonance would then be able to boost its eccentricity to Earth-crossing values in a much shorter time than it would take to drift the entire distance to Earth under the Yarkovsky force.

Following these early works, there has been a significant increase in our understanding of the Yarkovsky effect as well as its importance. Detailed analytical modeling of the Yarkovsky effect has been performed by Vokrouhlický (1998a, 1998b, 1999), Vokrouhlický and Farinella (1998, 1999) and Vokrouhlický and Brož (1999), and numerical modeling has been done by Spitale and Greenberg (2001, 2002). Recently, the Yarkovsky effect has been shown to best explain the dispersion seen in asteroid families (Bottke et al., 2001), and orbital change has been observationally detected during decade-long tracking of the near-earth asteroid Golevka (Chesley et al., 2003).

Farinella et al. (1998b) and Farinella and Vokrouhlicky (1999) combined a model of the semimajor axis drift rates due to the Yarkovsky effect with a collisional simulation of the asteroid population, in which spin-axis reorientations can change the direction of the diurnal Yarkovsky drift. They found that stony asteroids on the order of a few meters in diameter could drift up to about 0.1 AU during their collisional lifetime; Iron asteroids, while they drift more slowly, survive impacts for much longer and could drift up to 1 AU during their collisional lifetime. This offers a qualitative explanation for the long CRE ages of meteorites (tens of Myr for stony meteorites, 10-100 times longer for irons) relative to their dynamical transport times via resonances (only a few million years), since the Yarkovsky effect can allow a meteoroid to drift in the main belt and accumulate cosmic ray exposure for a significant period of time before encountering a resonance such as the ν_6 or 3:1, which would then quickly send it into near-Earth space. The much lower drift rates of iron meteoroids and their larger strength allows them to drift for a longer time and accumulate more cosmic ray exposure than stony bodies before encountering a resonance. Using a Monte-Carlo model, Vokrouhlický and Farinella (2000) were able to model the meteorite delivery process more quantitatively, and found that they could reproduce the observed CRE age distributions of chondrites. Additionally, they noted that a wide range of asteroids, even those not close to a resonance, have the potential to contribute to Earth's meteorite flux.

Bottke et al. (2000) more rigorously modeled the interaction of resonances with the Yarkovsky effect by using a version of the Levison and Duncan (1994) integrator that they had modified to incorporate Yarkovsky forces. They showed that meter- to hundred-meter-diameter bodies can drift for significant distances in the main belt under the influence of the Yarkovsky effect and can sometimes become temporarily trapped in weak, higher-order resonances or jump between higher-order resonances. Despite such effects, after tens of Myr most of these small asteroids end up being trapped in a strong resonance (eg. the ν_6 or 3:1) and delivered to near-Earth space.

Migliorini et al. (1998) demonstrated that another route is more important for large Earth- and Mars-crossing asteroids (5 km or larger), of which there were 10 Earth-crossers and 354 Mars-crossers known when their paper was written. Given short dynamical lifetimes of bodies in resonances like the ν_6 and 3:1, they noted that the delivery of Mars- and Earth-crossing asteroids through these routes would require the injection of approximately 100 large bodies into those resonances per million years to maintain the population in steady state. Since bodies this large are unlikely to have significant Yarkovsky mobility, and collisional events large enough to create multi-kilometer fragments and inject them into resonance are rare, such routes did not seem viable. In addition, direct delivery through the ν_6 and 3:1 resonances would lead to a significantly higher ratio of Earth-crossers to Mars-crossers than is observed, since those resonances increase the eccentricity so rapidly.

Migliorini et al. (1998) found that weaker resonances probably dominate the delivery process for multi-kilometer asteroids. These weak, high order resonances include the 3:5 and 7:12 with Mars, the 7:2 and 10:3 with Jupiter, and three-body mean motion resonances with Jupiter and Saturn or with Mars and

Jupiter. Nesvorný and Morbidelli (1998) and Morbidelli and Nesvorný (1999) describe these types of resonances in detail, and show that there are on the order of hundreds throughout the entire main belt. Morbidelli and Nesvorný (1999) show that there is a relatively constant 'diffusion background' where essentially every asteroid experiences some eccentricity change, punctuated by 'main diffusion tracks' that correspond to stronger, more chaotic, resonances that give larger eccentricity changes and supply the majority of the Mars-crossers.

Migliorini et al. showed through numerical integrations that such weak resonances can cause asteroids in the inner main-belt (inwards of the 3:1 resonance at 2.5 AU) to slowly increase in orbital eccentricity to Mars-crossing values. In their simulations, which began with asteroids whose eccentricities were high enough to make them near-Mars-crossers, nearly 25% of the asteroids in the inner-main belt reach Mars-crossing eccentricities within 100 Myr. Then, encounters with Mars cause these asteroids to wander in semimajor axis until they enter the ν_6 and 3:1 and become Earth-crossers. Integrating a large number of Mars-crossers in the inner- and central- (between the 3:1 resonance at 2.5 AU and the 5:2 resonance at 2.8 AU) main belt, they find that the Mars-crossing asteroids are capable of supplying the observed number of Earth-crossers. The median time for the largest group of Mars-crossing objects (those below the ν_6 resonance) to become Earth-crossers through this route is on the order of 20 Myr, and the median dynamical lifetime of those bodies is about 25 Myr. Most of them are ejected from the inner solar system by Jupiter encounters or collide with the sun.

The Migliorini et al. theory quantitatively reproduces the observed numbers of Earth- and Mars-crossing asteroids, as it allows for the injection of a much larger amount of material into Mars- and Earth-crossing orbits than direct injection or Yarkovsky drift into the ν_6 and 3:1 resonances. In addition, the Migliorini et al. theory explains the observed ratio of Earth-crossers to Mars-crossers, since asteroids taking this route spend a relatively long time in the Mars-crossing population before being perturbed into Earth-crossing orbits. The material removed from the weak resonances through this route would have to be replenished somehow in order to maintain a steady state. Migliorini et al. suggested that collisional events and/or the Yarkovsky effect provide replenishment: Given the close spacing of the high-order resonances throughout the main belt, small changes in semimajor axis would be sufficient to push a new asteroid into one of these resonances. Farinella and Vokrouhlicky (1999) noted that the Yarkovsky drift rates for multi-km objects (on the order of 0.01 AU over their collisional lifetimes) are consistent with this picture. In addition, Morbidelli and Nesvorný (1999) suggest that low-eccentricity bodies in the asteroid belt, which were not included in the Migliorini et al. simulations, could diffuse to higher eccentricities via weak resonances and resupply some of the bodies that are removed.

4.2 The Bottke et al. Simulations

Bottke et al. (2000, 2002) performed a large number of numerical integrations of test bodies starting in various orbits, including the ν_6 and 3:1 resonances, Mars-crossing orbits, the outer main-belt (which contains numerous strong resonances like the 5:2 as well as numerous three-body resonances) and Jupiter-family comet (JFC) orbits. From these integrations, they constructed maps of the orbital element distribution of bodies evolving from these different source regions. They then compared these results to the orbital and absolute magnitude distribution of NEAs observed by Spacewatch, and working backwards they inferred the relative numbers of bodies in the NEA population coming from each of the different source regions. The ν_6, intermediate-source Mars-crossing (IMC) population (Mars crossers below the ν_6 resonance), and 3:1 resonance are the largest sources of NEAs, with the outer main belt and non-active JFCs being secondary but still important sources.

Bottke et al. (2000, 2002) place strong constraints on both the dynamical removal rate of large (km-scale, or $H > 18$) asteroids from the main-belt, and the dynamical lifetimes of those bodies once they enter the NEA population. Table 4.1 shows the steady-state numbers N_{nea}, injection rates I into the NEA region, and mean dynamical lifetimes $\langle\tau_{nea}\rangle$ in the NEA region for components of the NEA population that originated in each of the primary NEA sources (from Bottke et al. (2002) Table III).

Dynamical Properties of NEA Source Regions

	ν_6	IMC	3:1	OB	JFC	Total
N_{nea} ($H < 18$)	360 ± 90	240 ± 40	220 ± 90	79 ± 12	61 ± 43	960 ± 120
I (Myr^{-1})	55 ± 18	65 ± 15	100 ± 50	570 ± 120	-	790 ± 200
$\langle\tau_{nea}\rangle$ (Myr)	6.54	3.75	2.16	0.14	-	-

Table 4.1: Dynamical properties of bodies coming from the different NEA source regions studied by Bottke et al. (2002).

From Table 4.1, the total injection rate I from the main-belt sources (everything but the JFCs) into the NEA population is 790 ± 200 bodies with $H < 18$ per Myr (Bottke et al. (2002) did not explicitly calculate I and $\langle\tau_{\rm nea}\rangle$ for the JFC population). A simulation by Morbidelli and Vokrouhlický (2003), which explicitly models the injection of asteroids into the ν_6 and 3:1 resonances via the Yarkovsky effect, is consistent with the injection rates I for the ν_6 and 3:1 from Bottke et al. (2002).

In a steady state, the influx rate I from a given source region into the NEA population is equal to the rate of dynamical elimination of those bodies from the NEA population, such that for a given source,

$$I = \frac{N_{nea}}{\langle\tau_{nea}\rangle} \tag{4.1}$$

(Bottke et al., 2002). The mean dynamical lifetime of all bodies in the NEA population coming from main-belt sources is therefore

$$\langle \tau_{nea} \rangle_{mb} = \sum_{mb} N_{nea} \bigg/ \sum_{mb} I, \tag{4.2}$$

where the subscript 'mb' refers to summation over all of the main-belt sources (everything but the JFCs). With the values in Table 4.1, $\langle \tau_{nea} \rangle_{mb}$ is 1.14 Myr. For all main-belt sources except the IMCs, $\langle \tau_{nea} \rangle_{mb-IMC}$ is 0.91 Myr, and for just the IMCs, $\langle \tau_{nea} \rangle_{IMC}$ is 3.75 Myr.

It is likely that $\langle \tau_{nea} \rangle$ is size-dependent, as smaller bodies with larger Yarkovsky drift rates can jump weak resonances and will be preferentially delivered through strong resonances like the ν_6 and 3:1, while larger, less Yarkovsky-mobile bodies will be more likely to come through weak resonances like those in the IMC region. However, the OB region contains both strong and weak resonances, and is unclear from the Bottke et al. (2002) whether or not it would have a preference for small or large bodies.

4.3 Summary and Discussion

In the last decade, the asteroid community has vastly improved its understanding of asteroid dynamics and the link between main-belt asteroids, NEAs, and meteorites. The 'classical' scenario of collisional injection of asteroid fragments into resonances and their subsequent 100 Myr random walk through the terrestrial planet region due to planetary perturbations has been replaced with a new scenario involving the complex interplay between resonances and the Yarkovsky effect. Small asteroids ($\lesssim$ 1 km in diameter), drift rapidly under the action of the Yarkovsky effect, jumping over weak resonances until they are trapped in a strong resonance like the ν_6 or 3:1 and sent to the terrestrial planet region, where they hit a planet, collide with the sun, or are ejected from the solar system within a few Myr. Larger asteroids drift more slowly, and can become trapped in higher-order resonances that are densely packed throughout the asteroid belt. They undergo a slow chaotic diffusion that increases their eccentricity to Mars-crossing values, at which point planetary perturbations can drive them into the NEA region. In addition to an an improved qualitative understanding of this process, our quantitative understanding had improved substantially as well. The work of Bottke et al. (2000, 2002) in particular has determined the debiased orbital distribution of NEAs, the supply rate of NEAs from different source regions within the asteroid belt, and the lifetimes of NEAs coming from different source regions.

One outstanding issue remains, however. While the results of Bottke et al. (2000, 2002) place a strong constraint on the number of large ($H < 18$) bodies removed from the main-belt and their lifetimes as NEAs, the removal rate of smaller bodies and the general size-dependence of the removal rate has not been well-determined. In the next section, we give a review of the Yarkovsky effect and derive an approximate relationship for the removal rate from the main belt as a function of size due to the combined action of the Yarkovsky effect and resonances.

CHAPTER 5

The Yarkovsky Effect and Asteroid Removal

In this chapter, we present a simple mathematical description of the Yarkovsky effect, based on the early analytical models by Peterson (1976) and Burns et al. (1979) as presented in Farinella et al. (1998b). While many derivations of the Yarkovsky effect exist in the literature, they generally don't yield simple analytical expressions for the semimajor axis mobility as a function of size (especially in the case of the 'seasonal' effect). Here, we give a simplified description of the Yarkovsky effect that, while an approximation, yields simple analytical expressions for the rate of change in semimajor axis that agree very well with published results from more complex analytical models (e.g. Farinella et al. (1998b)). Using the expressions we derive, we estimate the removal rate of bodies from the main-belt due to the action of the Yarkovsky effect and resonances. This estimate of the removal rate, while certainly not exact, provides a loose constraint on the actual removal rates from the main belt (i.e. the actual removal rates will likely follow the same general trend and not be wildly different from our estimate here).

We follow the general convention of treating the 'diurnal' and 'seasonal' effects separately, primarily because it is far easier mathematically. In reality, these are end-member cases and the Yarkovsky force experienced by a given body will be due to the simultaneous rotation about its axis and revolution around the Sun. For small eccentricity, Vokrouhlický (1999) showed that the total effect in most cases is well approximated, to within a tenth of a percent, by a linear combination of the diurnal and seasonal effects. Numerical models of the Yarkovsky effect show that, at high eccentricity, this assumption breaks down (Spitale and Greenberg, 2001; Spitale and Greenberg, 2002). This could potentially have profound effects for asteroids once they enter a resonance and have their eccentricities increased to high values.

5.1 Diurnal Yarkovsky Force

The simplest case of the Yarkovsky effect is the 'diurnal' effect originally proposed by Yarkovsky. This force is due to the fact that a rotating body orbiting the Sun absorbs radiation from the Sun, but rotates a bit before that energy is re-emitted as thermal radiation, leading to a longitudinal asymmetry between absorption and re-emission. This situation is analogous to the fact that it is hotter at 2 or 3 PM than at noon on Earth. The radiated energy causes either a positive or negative force along the track of the body's orbit, depending on whether the rotation is prograde or retrograde—prograde rotation causes a positive force, and hence semimajor axis increase, and retrograde rotation gives a negative force that causes semimajor axis decrease. The diurnal effect is maximum at zero obliquity, when the body's spin axis is perpendicular to the orbital plane, and vanishes at 90° obliquity. Figure 5.1 shows the force resulting from the diurnal Yarkovsky effect for the case of prograde rotation and zero obliquity.

Equating the incoming solar flux to the radiated flux from the asteroid and solving for the average temperature T gives

$$\begin{aligned} \pi R^2(1-A)S &= 4\pi R^2 \epsilon\sigma T^4 & (5.1)\\ T &= \left[\frac{(1-A)S}{4\epsilon\sigma}\right]^{\frac{1}{4}}, & (5.2) \end{aligned}$$

where A is the albedo (assumed to be zero), ϵ is the emissivity (assumed to be 1), and S is the solar flux (about 340 W/m^2 at 2 AU and 220 W/m^2 at 2.5 AU). The

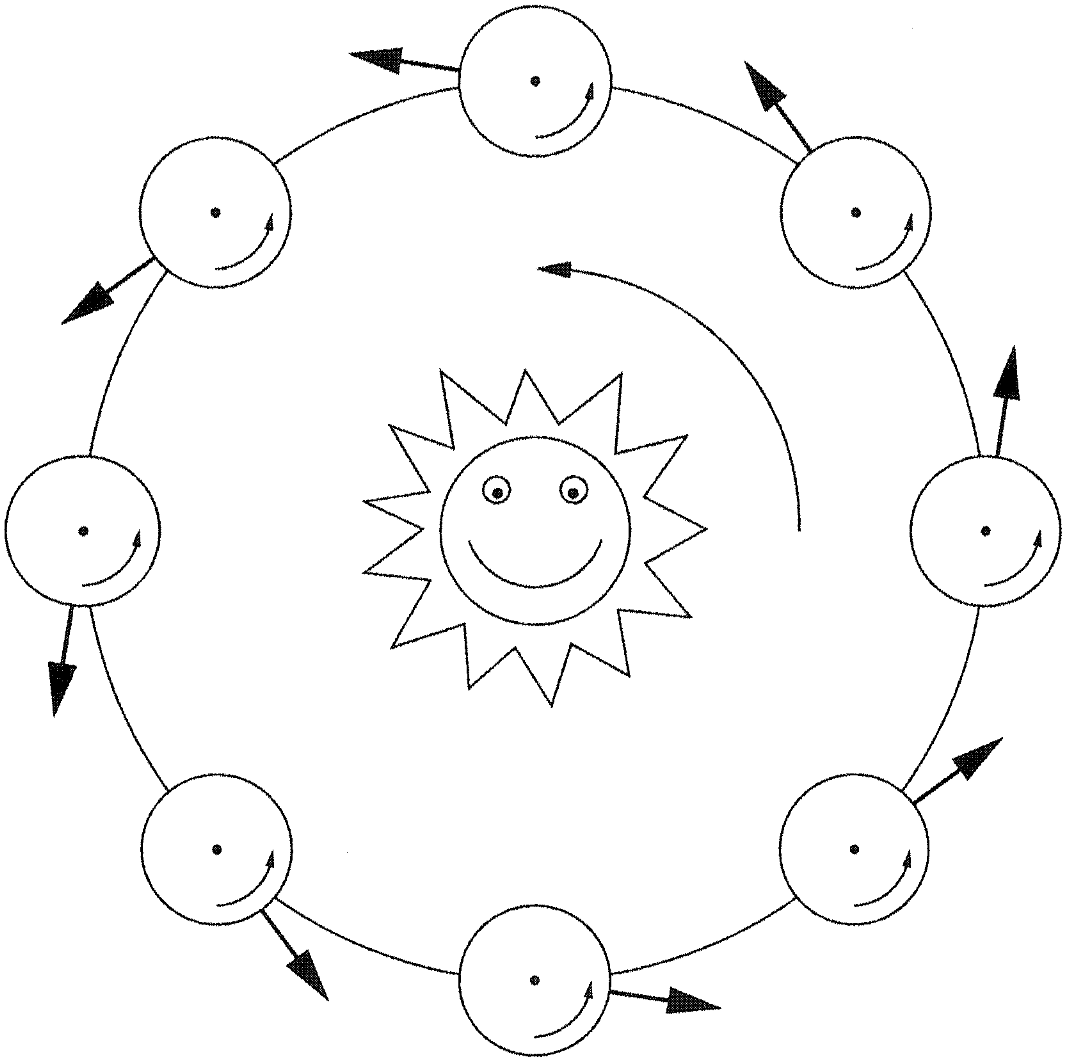

Figure 5.1: Diagram illustrating the 'diurnal' Yarkovsky effect for zero obliquity and prograde rotation. Because of the body's rotation, there is an asymmetry between the direction of absorption of sunlight and the re-emission of thermal radiation. This asymmetry leads to a force, indicated by the dark arrows, that causes the semimajor axis to increase. In the case of retrograde rotation, the semimajor axis will decrease. The effect diminishes as the obliquity tends towards 90°.

diurnal Yarkovsky effect relies on a temperature asymmetry about this mean value T, and hence its effectiveness diminishes when the heating on one side of the body begins to affect the other side. From Farinella et al. (1998b), this occurs when the asteroid's radius is comparable to or less than the thermal penetration depth given by

$$l_d = \sqrt{\frac{K}{\rho C_p \omega}}, \tag{5.3}$$

where K is the thermal conductivity, ρ is the density, C_p is the thermal conductivity, and ω is the rotation frequency ($2\pi/P_{rot}$, where P_{rot} is the rotation period). Assuming P_{rot} of 5 hours, which is reasonable for km-scale asteroids (Binzel et al., 1989), and the material parameters for basalt from Table 5.1, l_d is 5.6 cm. For the case where $P_{rot} = 5$ hr × $(D/1$ km$)$, which yields spin rates for cm-scale bodies that are consistent with laboratory experiments (Farinella et al., 1998b), all bodies larger than about 3 microns are larger than their corresponding l_d.

Thermal Parameters

Material	ρ (kg/m^3)	K (W/(m K))	C_p (J/(kg K))
Basalt	3500	2.65	680
Regolith	1500	0.0015	680
Iron	8000	40	500

Table 5.1: Material parameters for Yarkovsky model, from Farinella et al. (1998b).

The parameter Θ (Farinella et al., 1998b) is the ratio of the thermal emission timescale to the rotation timescale. For large Θ, energy absorbed at one point in the bodies rotation will be re-emitted over a significant fraction of the rotation cycle, such that temperature profile will get 'smeared out'. For small Θ, the absorbed energy will be re-emitted relatively quickly, such that a significant temperature asymmetry is present over the surface. For the diurnal Yarkovsky effect,

$$\Theta_d = \sqrt{\frac{\rho C_p K}{2\pi\epsilon T^3}}\sqrt{\omega} \tag{5.4}$$

where ω is the rotation frequency $2\pi/P_{rot}$. From Farinella et al. (1998b), the along-track Yarkovsky force (per unit mass) is given by

$$F_Y = \frac{2}{\rho R}\frac{\epsilon\sigma T^4}{c}\frac{\Delta T_d}{T}f(\zeta), \tag{5.5}$$

where $f(\zeta)$ is the obliquity term

$$f(\zeta) = \cos(\zeta) \tag{5.6}$$

and $\frac{\Delta T_d}{T}$ is the effective temperature difference between the 'AM' and 'PM' hemispheres given by

$$\frac{\Delta T_d}{T} = \frac{2}{3}\frac{\Theta_d}{1 + 2\Theta_d + 2\Theta_d^2} \tag{5.7}$$

(Farinella et al., 1998b).

5.2 Seasonal Yarkovsky Force

The seasonal Yarkovsky effect is due to latitudinal asymmetries between radiation absorption and re-emission occurring during a body's orbit around the Sun. It is maximum when the body's spin axis lies in the orbital plane (90° obliquity) and vanishes at zero obliquity (the opposite of the diurnal effect). This variant of the Yarkovsky effect is due to the fact that a body illuminated on a given hemisphere will move in its orbit before the energy absorbed is re-radiated as thermal energy. The seasonal effect depends somewhat on rotation, but as long as a body is rotating fast enough to minimize longitudinal temperature variations (as we assume here) the effects of rotation are second-order. The force that results from the seasonal effect is always opposite the direction of orbital motion, and thus always gives a semimajor axis decay. Figure 5.2 shows the seasonal Yarkovsky effect at 90° obliquity.

Since the heating timescales involved in the seasonal effect are significantly longer than for the diurnal effect, the thermal penetration depth l_s of the seasonal thermal wave

$$l_s = \sqrt{\frac{K}{\rho C_p n}}, \tag{5.8}$$

where n is the mean motion ($2\pi/P_{orbit}$), and hence the size of a body below which the seasonal effect diminishes, is larger than for the diurnal effect. Assuming an orbit at 2 AU ($P_{orbit} = 2.83$ yr) and the material parameters for basalt from Table 5.1, l_s is about 4 meters. The results of Farinella et al. (1998b) indicate that the peak seasonal effect occurs when the diameter $D \sim 4l_s$.

The mathematical description of the seasonal effect is somewhat more complicated than for the diurnal effect. However, we find that the seasonal effect (for bodies larger than about $4l_s$ in diameter) can be quite reasonably approximated by treating it like a diurnal effect with frequency n rather than ω and taking into account the fact that the seasonal asymmetry is present for only a fraction of the orbit. The $\frac{\Delta T_s}{T}$ calculated by treating the seasonal effect like the diurnal effect must be multiplied by a factor $\bar{f}_a$ to account for this.

Consider a circular orbit with a rapidly rotating body of radius R whose spin axis lies in the orbital plane, as shown in Fig. 5.3. If the mean anomaly M is zero when the southern hemisphere is fully illuminated and the northern hemisphere is totally dark, then it is easy to calculate the surface area of each hemisphere that is illuminated by the sun as a function of M. What is more important, however, is the

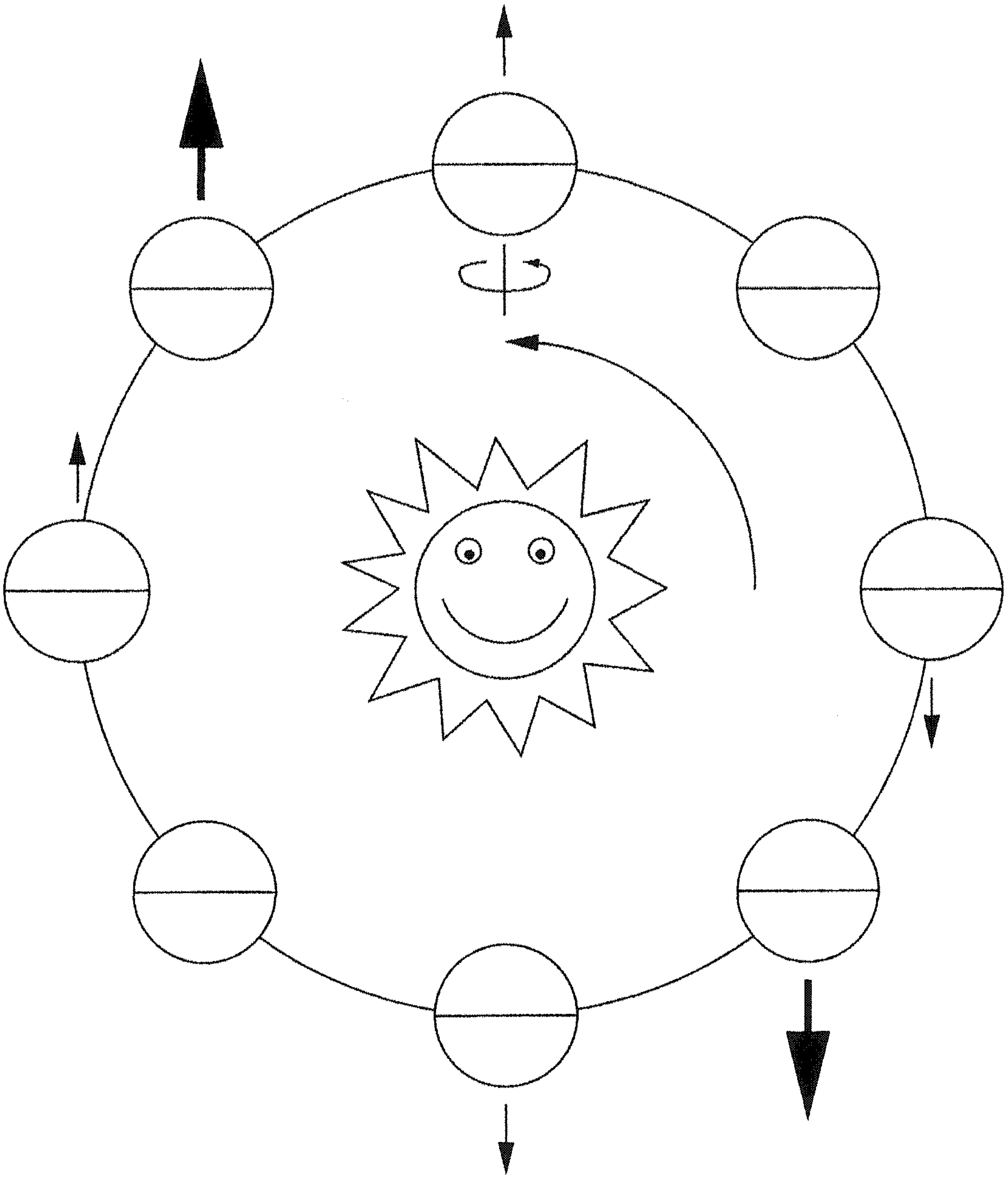

Figure 5.2: Diagram illustrating the 'seasonal' Yarkovsky effect for an obliquity of 90°. Because of the body's motion along its orbit, there is an asymmetry between the direction of absorption of sunlight and the re-emission of thermal radiation. This asymmetry leads to a force, indicated by the dark arrows, that causes the semimajor axis to decrease. The effect diminishes as the obliquity tends towards zero.

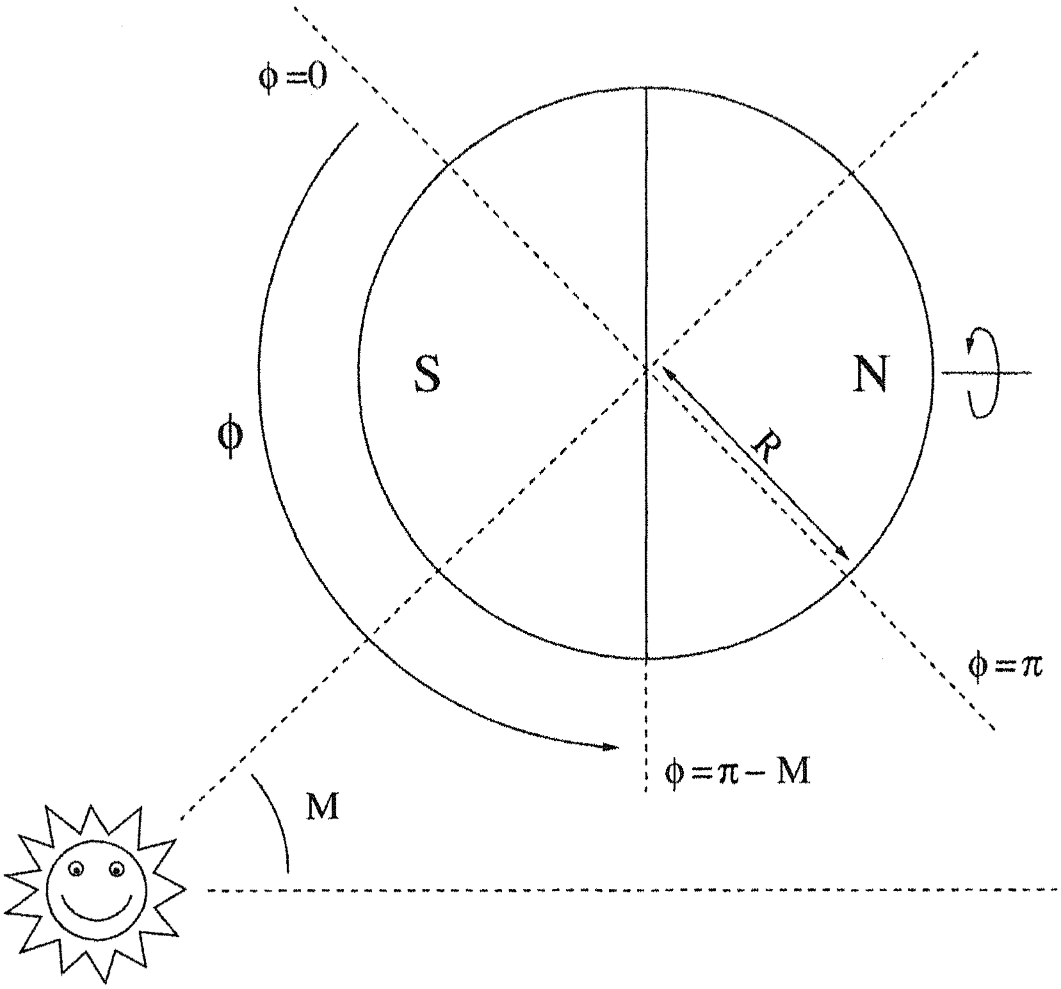

Figure 5.3: Diagram showing the geometry used for calculating the asymmetry factor f_a in our derivation of the magnitude of the seasonal Yarkovsky effect. At a given mean anomaly M in the orbit, the surface spanning the angles $\phi = 0$ to $\phi = \pi - M$ in the southern hemisphere and the angles $\phi = \pi - M$ to $\phi = \pi$ in the northern hemisphere will be illuminated. From this, we can calculate the projected areas of these regions as seen from the sun, and hence the asymmetry of solar heating between the northern and southern hemispheres as described in the text.

projected area illuminated by the sun, which is directly proportional to the amount of heat received by the body. For the northern hemisphere, we find the projected area A_N by integrating over the angle ϕ shown in Fig. 5.3 from 0 to $\pi - M$ (ϕ is like a longitude, but does not correspond to the actual longitude on the body) and the angle θ from 0 to π (θ is like a colatitude, but does not correspond to the actual latitude on the body)

$$A_N = \int_0^{\pi-M} \int_0^{\pi} R\ \mathrm{d}\theta\ R\sin(\theta)\ \mathrm{d}\phi\ \ \sin(\theta)\sin(\phi). \tag{5.9}$$

For the southern hemisphere we integrate the same expression over ϕ from $\pi - M$ to π. The projected area illuminated in each hemisphere as a function of M is then

$$\begin{aligned} A_N &= \frac{\pi R^2}{2}\left(1 - \cos(M)\right) && (5.10) \\ A_S &= \frac{\pi R^2}{2}\left(1 + \cos(M)\right). && (5.11) \end{aligned}$$

We define the asymmetry factor f_a as

$$f_a = \frac{A_S - A_N}{\pi R^2} = \cos(M), \tag{5.12}$$

and the average value $\bar{f}_a$ for a circular orbit is given by

$$\bar{f}_a = \frac{2}{\pi}\int_0^{\pi/2} \cos(M)\ \mathrm{d}M = \left[\frac{2}{\pi}\sin(M)\right]_0^{\pi/2} = \frac{2}{\pi}. \tag{5.13}$$

The seasonal effect can now be calculated in the same manner as the diurnal effect with

$$\Theta_s = \sqrt{\frac{\rho C_p K}{2\pi\epsilon T^3}}\sqrt{n} \tag{5.14}$$

and

$$\frac{\Delta T_s}{T} = \frac{2}{3}\frac{\Theta_s}{1 + 2\Theta_s + 2\Theta_s^2}\bar{f}_a, \tag{5.15}$$

which is multiplied by the asymmetry factor $\bar{f}_a$. Inserting these values into Eqn. 5.5 with the obliquity term

$$f(\zeta) = -\sin^2(\zeta) \tag{5.16}$$

(Farinella et al., 1998b) gives F_Y for the seasonal effect, which is accurate for bodies larger than about $4l_s$ in diameter. Explicitly calculating the seasonal force for bodies smaller than this is mathematically much more difficult. Instead, we assume here that for bodies smaller than $4l_s$, the seasonal $F_Y \propto D^{3/2}$, such that F_Y drops with decreasing size. This assumption is reasonably accurate, as compared to explicit calculations by Farinella et al. (1998b) and Bottke et al. (2000).

5.3 Semi-major Axis Mobility due to the Yarkovsky Effect

The along-track Yarkovsky force per unit mass F_Y can be converted to a semimajor axis change with

$$\dot{a} = \frac{2F_Y}{n} \tag{5.17}$$

(Farinella et al., 1998b), where n is the mean motion $(2\pi/P_{orbit})$.

Figure 5.4 shows a range of cases for comparison with the results presented in Farinella et al. (1998b) and Bottke et al. (2000). Note that, as clarified in Farinella et al. (1998a), the plotted values of the seasonal effect in Farinella et al. (1998b) are a factor of 2 smaller than they should be, due to a numerical error (their mathematical derivations do not contain this error). In Fig. 5.4, the semimajor-axis drift rate $\dot{a}$ of stony bodies at $a = 2$ AU is plotted as a function of diameter for a variety of different cases: Diurnal effect on a regolith-free body with a 5-hour spin period (P_{rot}); Diurnal effect on a regolith-free body with $P_{rot} = 5$ hr × (D/1 km); Diurnal effect on a regolith-covered body with $P_{rot} = 5$ hr × (D/1 km); Seasonal effect on a regolith-free body; And seasonal effect on a regolith-covered body. The obliquity is 0° for the diurnal cases and 90° for the seasonal cases, such that the plotted $\dot{a}$ are the theoretical maximum values. For regolith-free bodies, the material parameters for basalt from Table 5.1 are used. For regolith-covered bodies, material parameters for regolith from Table 5.1 are used except in Eq. 5.5, where the density for basalt is used. Our results agree quite closely with Farinella et al. (1998b) and Bottke et al. (2000) for the diurnal cases, as expected since we use essentially the same derivation as Farinella et al. (1998b). Additionally, our results agree quite well with Farinella et al. (1998b) and Bottke et al. (2000) for the seasonal cases (except for the physically unrealistic case of regolith-covered bodies below ~ 1 m in diameter), indicating that our simplified derivation of the seasonal effect is reasonable.

Figure 5.5 shows the semimajor-axis drift rate $\dot{a}$ of iron bodies at $a = 2$ AU as a function of diameter for a variety of different cases: Diurnal effect on a regolith-free body with a 5-hour spin period (P_{rot}); Diurnal effect on a regolith-free body with $P_{rot} = 5$ hr × (D/1 km); And seasonal effect on a regolith-free body. The obliquity is 0° for the diurnal cases and 90° for the seasonal case. Material parameters for iron from Table 5.1 are used. Our results agree well with Farinella et al. (1998b). Note that the drift rates are nearly a factor of 10 smaller than the corresponding stony cases from Fig. 5.4, a fact invoked to explain the larger CRE ages of iron vs. stony meteorites as discussed in Chapter 4.

Pravec et al. (2002) show that asteroids between ~ 0.15 km and 10 km in diameter have average rotation periods on the order of 6 hours, with bodies $\gtrsim 10$ km

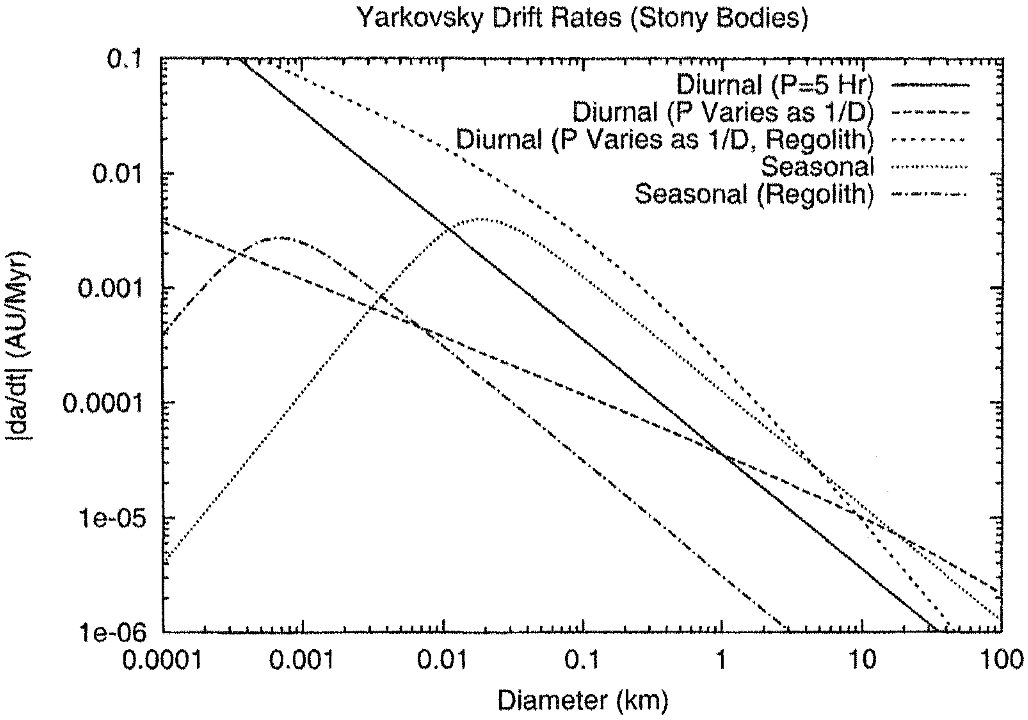

Figure 5.4: Plot of the semimajor-axis drift rate $\dot{a}$ of stony bodies at a=2 AU as a function of diameter for a variety of different cases: Diurnal effect on a regolith-free body with a 5-hour spin period (P_{rot}); Diurnal effect on a regolith-free body with P_{rot} = 5 hr × (D/1 km); Diurnal effect on a regolith-covered body with P_{rot} = 5 hr × (D/1 km); Seasonal effect on a regolith-free body; Seasonal effect on a regolith-covered body. The obliquity is 0° for the diurnal cases and 90° for the seasonal cases. For regolith-free bodies, the material parameters for basalt from Table 5.1 are used. For regolith-covered bodies, material parameters for regolith from Table 5.1 are used except in Eq. 5.5, where the density for basalt is used.

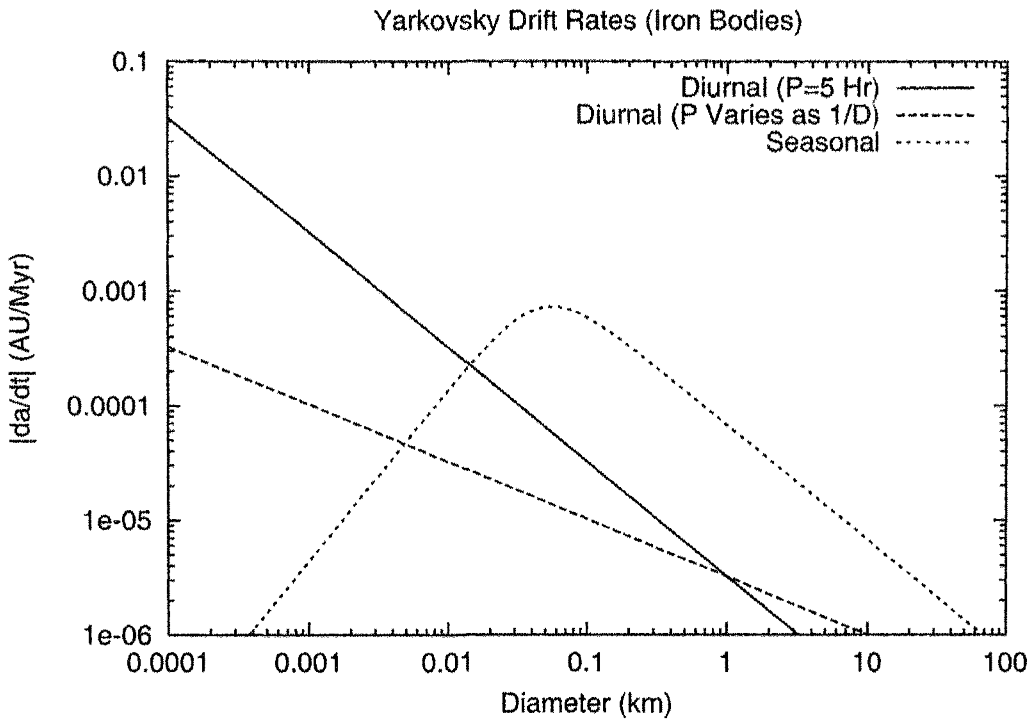

Figure 5.5: Plot of the semimajor-axis drift rate $\dot{a}$ of iron bodies at a=2 AU as a function of diameter for a variety of different cases: Diurnal effect on a regolith-free body with a 5-hour spin period (P_{rot}); Diurnal effect on a regolith-free body with P_{rot} = 5 hr × (D/1 km); Seasonal effect on a regolith-free body. The obliquity is 0° for the diurnal cases and 90° for the seasonal case. Material parameters for iron from Table 5.1 are used. Note that the drift rates are nearly a factor of 10 smaller than the corresponding stony cases from Fig. 5.4.

in diameter having average rotation periods up to a factor of 2 or so longer. These rotation periods are long enough that even if the asteroids were rubble piles with no material strength, they could be kept together purely by gravity. Below ~ 0.15 km in diameter, however, nearly all asteroids that have had their rotation periods measured have rotation periods so short that they must be solid, monolithic bodies or they would be torn apart. As asteroid diameter decreases below ~ 0.15 km, the rotation period seems to decrease as well. The fastest rotator found so far, 2000 DO$_8$, is about 80 meters across and has a spin period of about 1.3 minutes. Rotation statistics for bodies smaller than ~ 0.15 km are biased towards faster rotators, since it is easier to get lightcurves for them. While the transition in rotation period around ~ 0.15 km in diameter is certainly real, the statistics at this point are insufficient to infer the actual P_{rot} vs. D relationship, especially extending down to meter-scale and smaller bodies. As a reasonable estimate of asteroid rotation rates, we use $P_{rot} = 6$ hr for bodies larger than 0.15 km and $P_{rot} \propto D$ (Farinella et al., 1998b) for smaller bodies:

$$\begin{aligned} P_{rot} &= 6 \text{ hr} \times (D/0.15 \text{ km}) \qquad (D < 0.15 \text{ km}), \\ P_{rot} &= 6 \text{ hr} \qquad\qquad\qquad\quad\; (D \geq 0.15 \text{ km}). \end{aligned} \tag{5.18}$$

In addition to a transition in rotation period, the data presented in Pravec et al. (2002) indicate that a diameter of ~ 0.15 km may divide regolith-free bodies from those capable of retaining a significant regolith. Accordingly, we model the Yarkovsky effect for bodies smaller than 0.15 km in diameter using surface thermal parameters (density and thermal conductivity) for bare rock and use regolith thermal parameters for bodies larger than 0.15 km, with these parameters transitioning smoothly around 0.15 km

$$\rho = \rho_{reg} + \frac{\rho_{rock} - \rho_{reg}}{2}\left(1 + \tanh\left(2\log\left(\frac{0.15\ \mathrm{km}}{D}\right)\right)\right) \tag{5.19}$$

$$K = K_{reg} + \frac{K_{rock} - K_{reg}}{2}\left(1 + \tanh\left(2\ \log\left(\frac{0.15\ \mathrm{km}}{D}\right)\right)\right), \tag{5.20}$$

where ρ_{rock} and K_{rock} are the thermal parameters for basalt and ρ_{reg} and K_{reg} are the thermal parameters for regolith from Table 5.1.

Figure 5.5 shows the diurnal and seasonal $\dot{a}$ of stony bodies at $a = 2.5$ AU with P_{rot} given by Eq. 5.18 and ρ and K given by Eqns. 5.19 and 5.20 (except in Eq. 5.5, where the density for basalt is always used). The obliquity is 0° for the diurnal case and 90° for the seasonal case.

5.4 The Yarkovsky Effect and Asteroid Removal

The Yarkovsky semimajor-axis drift rate $\dot{a}$ can be converted to $f_{rem}(D)$, the fraction of bodies of diameter D removed per unit time with

$$f_{rem}(D) = \frac{\dot{a}(D)}{\Delta a}N_{res}, \tag{5.21}$$

where Δa is the effective width of the asteroid belt and N_{res} is the number of resonances in the asteroid belt that are capable of removing asteroids of a given diameter. Since the large majority of asteroids lie between the ν_6 resonance around 2.1 AU (for zero inclination) and the 2:1 resonance around 3.3 AU, Δa is approximately 1.2 AU. Sub-kilometer asteroids, which have drift rates high enough to jump weak resonances, can be removed by 6 strong resonances—the ν_6, 3:1, 5:2, 7:3, 9:4, and 2:1 (Bottke et al., 2002).

Km-scale and larger asteroids drift slowly enough that they can be significantly affected by the weaker resonances in the asteroid belt and be pushed into the

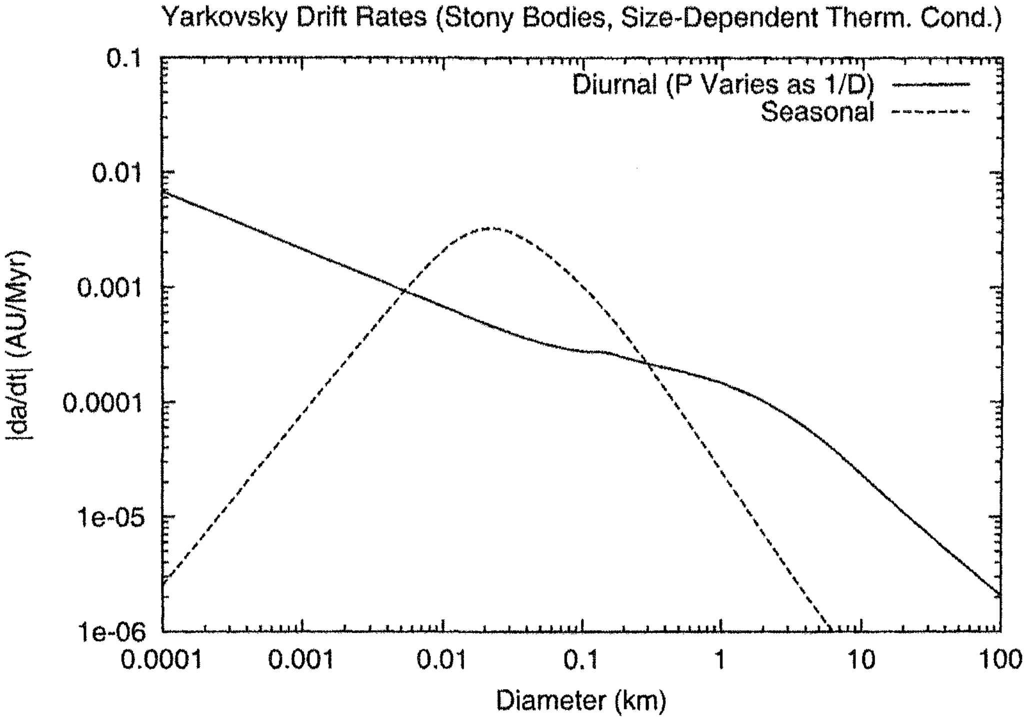

Figure 5.6: Plot of the diurnal and seasonal semimajor-axis drift rate $\dot{a}$ for stony bodies at $a = 2.5$ AU that change smoothly from regolith-free to regolith-covered around 0.15 km in diameter. The spin period P_{rot} is 6 hours for bodies larger than 0.15 km in diameter, and $P_{rot} = 6$ hr $\times$ $(D/0.15$ km$)$ for smaller bodies. The obliquity is 0° for the diurnal case and 90° for the seasonal case.

Mars- and eventually Earth-crossing populations, as described by Migliorini et al. (1998). There are hundreds of these resonances throughout the main belt (Nesvorný and Morbidelli, 1998; Morbidelli and Nesvorný, 1999). Using $N_{res} = 100$ or more with the $\dot{a}$ values from Fig. 5.6, however, gives a removal rate for multi-kilometer bodies that is far larger than estimates by Morbidelli and Nesvorný (1999) of about 4 bodies larger than 5 km per Myr ($f_{rem} \sim 0.0002$ Myr^{-1}) for the inner-main belt (probably a factor of a few larger for the entire main belt). Instead, we use $N_{res} = 25$, which is the number of strong resonances plus the approximate number of 'main diffusion tracks' in the entire main-belt, scaled up from the inner-main belt estimate of Morbidelli and Nesvorný (1999). This approach yields much more reasonable removal rates.

In our calculation of the removal rate, we assume that the weak resonances first become effective for bodies around 0.1 km and all of them are fully effective for bodies 10 km in diameter or larger, such that $N_{res} = 6$ (the number of strong resonances) at $D \leq 0.1$ km and $N_{res} = 25$ at $D \geq 10$ km, with a linear variation between them (in log space).

The effective $\dot{a}$ for Eq. 5.21 is a combination for the seasonal and diurnal effects. The seasonal effect always gives a semimajor axis decrease, but the diurnal can cause either an increase or a decrease depending on the obliquity. The magnitude of both effects depends on the obliquity. The mean absolute values of the obliquity terms $f(\zeta)$ (Eqns. 5.6 and 5.16) can be found by integrating over all possible spin axis directions

$$\langle|f(\zeta)|\rangle = \frac{1}{2\pi}\int_0^{\pi/2}\int_0^{2\pi} |f(\zeta)| \sin(\zeta)\ \mathrm{d}\phi\ \mathrm{d}\zeta, \tag{5.22}$$

which yields

$$\begin{aligned} \langle |f(\zeta)_d| \rangle &= 1/2 && (5.23) \\ \langle |f(\zeta)_s| \rangle &= 2/3. && (5.24) \end{aligned}$$

The maximum and minimum absolute values of $\dot{a}$ are

$$\begin{aligned} |\dot{a}|_{min} &= \mathrm{abs}(2/3\ |\dot{a}_s(\zeta = 90^o)| - 1/2\ |\dot{a}_d(\zeta = 0^o)|) && (5.25) \\ |\dot{a}|_{max} &= \mathrm{abs}(2/3\ |\dot{a}_s(\zeta = 90^o)| + 1/2\ |\dot{a}_d(\zeta = 0^o)|), && (5.26) \end{aligned}$$

and the average value is

$$\langle \dot{a} \rangle = \frac{|\dot{a}|_{min} + |\dot{a}|_{max}}{2}. \tag{5.27}$$

Figure 5.7 shows the removal rate as a function of diameter due to the action of resonances and the Yarkovsky effect, calculated using Eqns. 5.21 and 5.25-5.27, with the $\dot{a}$ values from Fig. 5.6 and the assumptions about the number of effective resonances discussed above. These removal rates do not take into account the effects of collisional reorientation of the spin axis, which can cause the diurnal Yarkovsky effect to switch direction and lead to a random walk in semimajor axis, rather than a continuous drift. Farinella et al. (1998b) estimate that several collisional reorientations should occur for most bodies over their collisional lifetimes, and thus the effective diurnal $\dot{a}$ would be decreased by a factor $1/\sqrt{N}$, where N is the number of collisional reorientation events over a body's collisional lifetime (a factor of 1/2 assuming $N = 4$).

In addition to collisional re-orientation of the spin axis, several other effects can modify the spin state of an asteroid or the magnitude of the Yarkovsky effect.

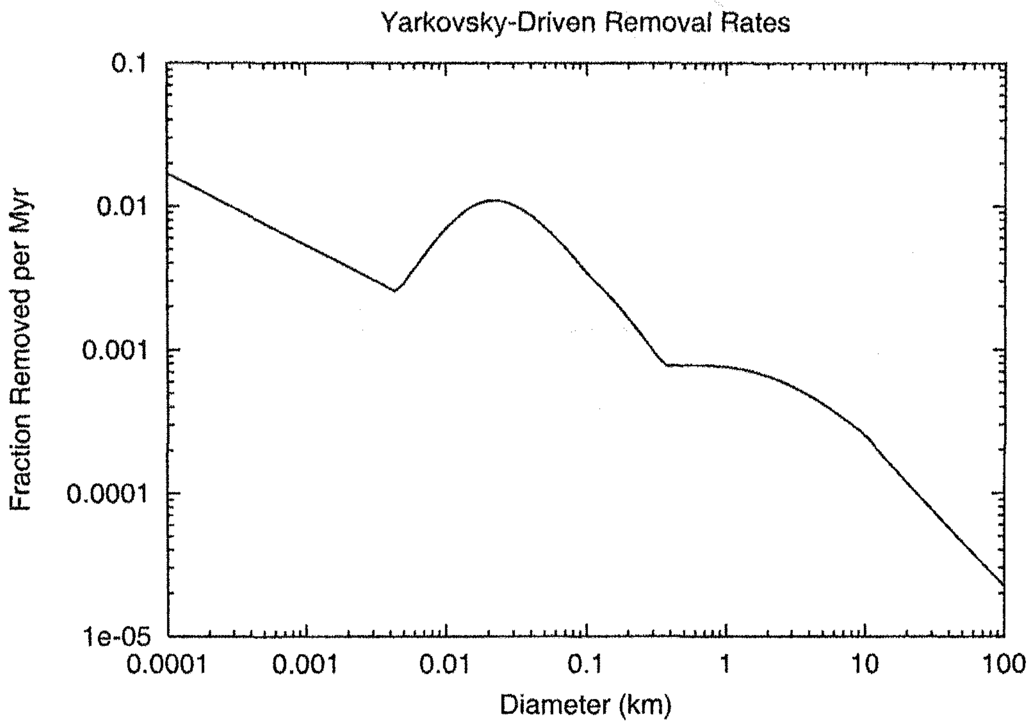

Figure 5.7: Plot of the removal rate as a function of diameter due to the action of resonances and the Yarkovsky effect, calculated using Eqns. 5.21 and 5.25-5.27, with the $\dot{a}$ values from Fig. 5.6 and the assumptions about the number of effective resonances discussed in the text.

The YORP effect, a radiation force that can modify the spin rate and spin-axis orientation of asteroids, can preferentially drive asteroids into certain obliquity states (Rubincam et al., 2002; Vokrouhlický and Čapek, 2002). As discussed in Spitale and Greenberg (2002), most asteroids are not perfect spheres, and it is possible that many asteroids are in a state of non-principal-axis rotation (tumbling or wobbling). As effects such as these are not included in the simple analytical model we present here, the actual removal rate of asteroids from the main belt likely differs somewhat from our estimate, but is likely to follow the same general trends and be of the same order of magnitude. Normalized to the estimates of Bottke et al. (2000, 2002) for the removal rate of $H < 18$ bodies from the main-belt, the estimated removal rate calculated in this section provides a loose constraint on the range of allowable values of $f_{rem}(D)$ that can be used as inputs to the model we describe in the following section.

CHAPTER 6

Numerical Collisional and Dynamical Evolution Model

Our simulation of the evolution of the main-belt and NEA size distributions is based on a modification of Petit and Farinella's (1993) algorithm for calculating collisional outcomes, which in turn is a refinement and extension of earlier models beginning with Greenberg et al. (1978). Our modifications to the Petit and Farinella (1993) algorithm allow for a broken power-law representation of the fragment size distribution (different power-law indices for small- and large-mass bodies) as well as correct for an error in their calculation of the escape velocity. Our modified algorithm, which we describe in Section 6.1.1, computes the fragment distribution resulting from a collision between a given pair of bodies. All types of collisions are treated, from small cratering impacts to super-catastrophic fragmentation events. In Section 6.1.2, we use this algorithm to construct a matrix of all possible collisional outcomes for a given set of input parameters that is then used in a numerical simulation to evolve the entire main-belt and NEA populations under the influence of mutual collisions and dynamical effects. In Section 6.2, we perform a number of simulations to determine the effect of changing the different input parameters to the model. Finally, in Section 6.3, we present the strength law and dynamical parameters that best fit the constraints 1-5 outlined in Chapter 2 and show that our results are consistent with estimates of asteroid strength and dynamical models by other authors.

6.1 NEA and Main Belt Collisional and Dynamical Evolution Model

6.1.1 Outcome of Single Collisional Events

Recall (Section 2.2) that the strength of material against catastrophic fragmentation is generally parameterized as the amount of energy per unit mass Q_S necessary to fragment a body such that the largest intact fragment has half the mass of the original body. Here we use Q_S averaged over all possible impact angles (e.g. Benz and Asphaug (1999)), not just the value for head-on impacts.

The amount of kinetic energy in a collision between two masses M_1 and M_2 is

$$E_{rel} = \frac{1}{2}\frac{M_1 M_2}{M_1 + M_2} V_{rel}^2, \tag{6.1}$$

Assuming that the energy is partitioned equally between the target and the projectile (i.e. each gets $E_{rel}/2$), fragmentation occurs when $E_{rel} > 2Q_S M_i$ (Greenberg et al., 1978; Petit and Farinella, 1993). Below this threshold, cratering occurs. The actual energy partitioning likely depends on factors such as the projectile/target mass ratio, but that dependence is not well-constrained and is therefore not included in our model. There are three possible outcomes of a collision between two bodies: both are catastrophically fragmented; one is cratered and the other is catastrophically fragmented; or (rarely at asteroidal collisional velocities) neither is disrupted, both are cratered, and they potentially stick together. In any case, the size distributions of escaping fragments from both bodies in a collision must be individually calculated and then combined to determine the final fragment distribution.

Catastrophic Fragmentation

In a catastrophic fragmentation event, the fractional mass of the largest fragment is given by

$$f_l = \frac{1}{2}\left(\frac{Q_S M}{E_{rel}/2}\right)^{1.24} \tag{6.2}$$

(Fujiwara et al., 1977). The actual mass of the largest fragment is then $m_{max} = M f_l$, where M is the mass of the body before fragmentation. Petit and Farinella (1993) use a single-slope power law, truncated at a small-mass cutoff, to describe the size distribution of fragments smaller than m_{max}.

Here we introduce a more realistic two-slope power law. Both laboratory fragmentation studies (Fujiwara et al., 1977; Davis and Ryan, 1990; Nakamura and Fujiwara, 1991) and hydrocode models (Melosh et al., 1992; Ryan and Melosh, 1998) find that a two-slope power law is a much more realistic description of the fragments resulting from catastrophic fragmentation. Accordingly, the differential, or incremental, fragment size distribution can be given by the piecewise function

$$\mathrm{d}N = \begin{cases} b_2 B_2 m^{-b_2-1}\mathrm{d}m & m \le m_t \\ b_1 B_1 m^{-b_1-1}\mathrm{d}m + \delta(m - m_{max})\mathrm{d}m & m_t < m \le m_{max} \\ 0 & m > m_{max}, \end{cases} \tag{6.3}$$

where there is a single largest fragment of mass m_{max} and a transition in slope at m_t. b_1+1 and b_2+1 are the large- and small-mass indices, respectively. We define r_b as the ratio b_2/b_1 and r_m as the ratio m_t/m_{max} (both ratios are less than 1, and are fixed as input parameters). Requiring continuity at the transition mass m_t yields the relation

$$B_2 = \frac{b_1}{b_2} B_1 m_t^{b_2 - b_1}. \tag{6.4}$$

From the incremental distribution in Eq. 6.3 we can derive the cumulative distribution

$$\begin{aligned} N(\geq m) &= \int_m^\infty \mathrm{d}N = \int_m^\infty b_1 B_1 m^{-1-b_1} \mathrm{d}m \\ &= B_1 m^{-b_1} \end{aligned} \tag{6.5}$$

for $m > m_t$ and

$$\begin{aligned} N(\geq m) &= \int_m^\infty \mathrm{d}N = \int_m^{m_t} b_2 B_2 m^{-1-b_2} \mathrm{d}m + \int_{m_t}^\infty b_1 B_1 m^{-1-b_1} \mathrm{d}m \\ &= B_2 m^{-b_2} + B_1 m_t^{-b_1} - B_2 m_t^{-b_2} \\ &= B_2 m^{-b_2} - (\frac{b_1}{b_2} - 1) B_1 m_t^{-b_1} \end{aligned} \tag{6.6}$$

for $m \leq m_t$. Since $N(\geq m_{max}) = 1$ by definition, from Eq. 6.5 we find

$$B_1 = m_{max}^{b_1}. \tag{6.7}$$

We can also derive the cumulative mass distribution

$$\begin{aligned} M(< m) &= \int_0^m m \mathrm{d}N = \int_0^m b_2 B_2 m^{-b_2} \mathrm{d}m \\ &= \frac{b_2 B_2 m^{1-b_2}}{1 - b_2} \end{aligned} \tag{6.8}$$

for $m \leq m_t$ and

$$\begin{aligned}
M(<m) &= \int_0^{m_t} m \mathrm{d}N + \int_{m_t}^{m} m \mathrm{d}N = \int_0^{m_t} b_2 B_2 m^{-b_2} \mathrm{d}m + \int_{m_t}^{m} b_1 B_1 m^{-b_1} \mathrm{d}m \\
&= \frac{b_1 B_1 m^{1-b_1}}{1-b_1} + \left(\frac{b_2 B_2 {m_t}^{1-b_2}}{1-b_2} - \frac{b_1 B_1 {m_t}^{1-b_1}}{1-b_1} \right) \\
&= \frac{b_1 B_1 m^{1-b_1}}{1-b_1} + \left(\frac{1}{1-b_2} - \frac{1}{1-b_1} \right) b_1 B_1 {m_t}^{1-b_1} \qquad (6.9)
\end{aligned}$$

for $m > m_t$. See Appendix A for the relations between the distributions presented above and other commonly used representations of the size and mass distributions.

From the cumulative mass distribution, we can derive the relation between f_l and b_1. By definition, $M(< m_{max}) = M(1 - f_l)$, where M is the target mass. Using $M(< m_{max})$ from Eqns. 6.8 and 6.9, along with $r_m = m_t/m_{max}$,

$$\begin{aligned}
M(1 - f_l) &= \frac{b_1 B_1 m_{max}^{1-b_1}}{1-b_1} + \left(\frac{b_1}{1-b_2} - \frac{b_1}{1-b_1} \right) B_1 {m_t}^{1-b_1} \\
&= \left[\frac{b_1}{1-b_1} + \left(\frac{b_1}{1-b_2} - \frac{b_1}{1-b_1} \right) r_m^{1-b_1} \right] B_1 {m_{max}}^{1-b_1}. \qquad (6.10)
\end{aligned}$$

Since $B_1 = m_{max}^{b_1}$ and $m_{max} = M f_l$,

$$M(1 - f_l) = \left[\frac{b_1}{1-b_1} + \left(\frac{b_1}{1-b_2} - \frac{b_1}{1-b_1} \right) r_m^{1-b_1} \right] M f_l. \qquad (6.11)$$

With $r_b = b_2/b_1$, Eq. 6.11 becomes

$$\frac{1-f_l}{f_l} = \frac{b_1}{1-b_1} + \left(\frac{b_1}{1-b_1 r_b} - \frac{b_1}{1-b_1} \right) r_m^{1-b_1}. \qquad (6.12)$$

Given f_l from Eq. 6.2 and the parameters r_m and r_b, Eq. 6.12 can be iteratively solved for b_1.

Cratering Impacts

For impacts below the catastrophic disruption threshold ($E_{rel} < 2Q_SM$) we follow the method of Petit and Farinella (1993) for calculating the mass of cratering debris in terms of the relative kinetic energy E_{rel} and α, the crater excavation coefficient:

$$\begin{aligned} M_{crat} &= \alpha E_{rel} && \text{for} \quad E_{rel} \le \frac{M}{100\alpha}, \\ M_{crat} &= \frac{9\alpha}{200Q_S\alpha - 1} E_{rel} + \frac{M}{10} \frac{1 - 20Q_S\alpha}{1 - 200Q_S\alpha} && \text{for} \quad E_{rel} > \frac{M}{100\alpha}. \end{aligned} \tag{6.13}$$

The parameter α ranges from about 4×10^{-4} to 10^{-5} s^2/m^2 for 'soft' and 'hard' materials, respectively (Stoeffler et al., 1975; Dobrovolskis and Burns, 1984). The normalization in Eq. 6.13 gives a linear variation in M_{crat} with E_{rel} for all E_{rel}, but for large E_{rel} it is normalized such that the largest possible crater contains 1/10 the mass of the target, in agreement with large craters observed on asteroids and hydrocode modeling of large impacts into asteroids (e.g. Greenberg et al. (1994), Nolan et al. (1996)).

Based on modeling of impacts (Melosh et al., 1992) and evidence from actual craters (Melosh, 1989), the fragment distribution from cratering events is best modeled as a single-slope power law, rather than the 2-slope power law used for catastrophic fragmentation. The previously derived expressions for the various number and mass distributions still apply in the cratering case, provided the parameters b_1 and b_2 are set equal to one another (i.e. $r_b = 1$) and the target mass M in those expressions is replaced by M_{crat}. Given b_1, f_l can be calculated from Eq. 6.12:

$$f_l = 1 - b_1. \tag{6.14}$$

We use $b_1 = 0.8$ (Melosh, 1989), which gives $f_l = 0.2$.

Fragment Mass-Velocity Relationship

After solving for the cumulative size distributions (Eqns. 6.5 and 6.6) of fragments from both bodies in a collision, the fragment distributions are binned into arrays F_1 and F_2, with elements spaced in constant logarithmic intervals. For example, the elements can be spaced by a factor of two in mass, such that a given bin centered at m spans the range $[m/\sqrt{2}, m\sqrt{2}]$. The next step is to assign both sets of fragments a velocity distribution. We follow the method of Petit and Farinella (1993) for calculating the fragment mass-velocity relationship, and we have extended their equations to account for the use of a broken power-law fragment size distribution.

One way to express the velocity distribution is as a cumulative velocity distribution with exponent k

$$M(\geq V) \propto V^{-k}. \tag{6.15}$$

Eq. 6.15 has been found to be a good description of crater ejecta with $k = 9/4$ (Gault et al., 1963), as well as the smaller-mass fragments (smaller than m_t) in experimental results with $k \sim 2$, although this may be slightly low due to a systematic bias towards higher velocity fragments from the surface of the target (Nakamura and Fujiwara, 1991). Alternatively, the mass-velocity distribution can be used

$$V = Cm^{-r}. \tag{6.16}$$

Experimental results (Nakamura and Fujiwara, 1991) indicate that even fragment size distributions described by multiple power laws generally have a velocity distribution following a single power law of the form of Eq. 6.16, with an exponent r of $\sim 1/6$. The cumulative velocity exponent k can be related to the exponent r in the mass-velocity distribution in Eq. 6.16 by inserting

$$m(V) = \left(\frac{V}{C}\right)^{-1/r}, \tag{6.17}$$

which is the fragment mass that has the average velocity V, into Eq. 6.8, yielding

$$\begin{aligned} M(\geq V) &= \frac{b_2 B_2}{1-b_2} m(V)^{1-b_2} \\ &= \frac{b_2 B_2}{1-b_2} \left(\frac{V}{C}\right)^{-\frac{1-b_2}{r}} . \end{aligned} \tag{6.18}$$

Comparing Eqns. 6.15 and 6.18 shows that

$$k = \frac{1-b_2}{r}. \tag{6.19}$$

Either k or r can be fixed as an input parameter. If r is fixed, Eq. 6.16 can be used to calculate the mass-velocity relation. If k is fixed, Eq. 6.19 can be used to calculate r as a function of b_2, and this value of r can be used in Eq. 6.16 to calculate the mass-velocity relationship.

The velocity distribution (Eq. 6.16) is given a maximum velocity of V_{max}, which is likely to be on the order of the sound speed in rock (several km/s) (Campo Bagatin et al., 1994). V_{max} corresponds to a mass of

$$m_{V_{max}} = \frac{{V_{max}}^{-1/r}}{C} . \tag{6.20}$$

In the case of a cratering impact, the largest fragment m_{max} is given a velocity

$$V_o = C m_{max}^{-r}, \tag{6.21}$$

while the largest fragment in a catastrophic fragmentation event has negligible kinetic energy, consistent with experimental results (Fujiwara and Tsukamoto, 1980; Nakamura and Fujiwara, 1991). If the energy imparted to the fragments of each body is given by

$$E_{fr} = f_{KE}\frac{E_{rel}}{2}, \tag{6.22}$$

where f_{KE} is the fraction of collisional energy partitioned into kinetic energy of the fragments, then the normalization constant C in Eq. 6.16 can then be found by the iterative solution of

$$\begin{aligned} E_{fr} &= \int_{m_{V_{max}}}^{m_t} \frac{V^2}{2} m\mathrm{d}N + \lim_{\epsilon\to 0}\int_{m_t}^{m_{max}-\epsilon} \frac{V^2}{2} m\mathrm{d}N + \frac{V_{max}^2}{2} M(\le m_{V_{max}}) + \lambda\frac{V_o^2}{2} m_{max} \\ &= \frac{C^2}{2}\frac{b_2B_2}{1-b_2-2r}\left[m_t^{1-b_2-2r} - m_{V_{max}}^{1-b_2-2_r}\right] + \frac{C^2}{2}\frac{b_1B_1}{1-b_1-2r}\left[m_{max}^{1-b_1-2r} - m_t^{1-b_1-2_r}\right] \\ &+ \frac{V_{max}^2}{2}\frac{b_2B_2}{1-b_2} m_{V_{max}}^{1-b_2} + \lambda\frac{C^2}{2} m_{max}^{1-2r} \end{aligned} \tag{6.23}$$

for $m_{V_{max}} \le m_t$ or

$$\begin{aligned} E_{fr} &= \lim_{\epsilon\to 0}\int_{m_{V_{max}}}^{m_{max}-\epsilon} \frac{V^2}{2} m\mathrm{d}N + \frac{V_{max}^2}{2} M(\le m_{V_{max}}) + \lambda\frac{V_o^2}{2} m_{max} \\ &= \frac{C^2}{2}\frac{b_1B_1}{1-b_1-2r}\left[m_{max}^{1-b_1-2r} - m_{V_{max}}^{1-b_1-2_r}\right] \\ &+ \frac{V_{max}^2}{2}\left[\frac{b_2B_2}{1-b_2} m_t^{1-b_2} + \frac{b_1B_1}{1-b_1}\left(m_{V_{max}}^{1-b_1} - m_t^{1-b_1}\right)\right] + \lambda\frac{C^2}{2} m_{max}^{1-2r} \end{aligned} \tag{6.24}$$

for $m_{V_{max}} > m_t$. The parameter λ is 1 for cratered bodies and 0 for catastrophically fragmented bodies, and accounts for the fact that the largest fragment in the fragmentation case has negligible kinetic energy while the largest fragment in the cratering case does not.

Escape and Reaccumulation of Fragments

Once the fragment velocity distribution has been found for both bodies involved in the collision, the next step is to find the effective escape velocity for the fragments resulting from the collision and determine which of those fragments are reaccumulated. We use the method outlined in Petit and Farinella (1993), which we modify to account for the use of a broken power-law fragment size distribution and to fix an error in their calculation.

Following Petit and Farinella (1993), we calculate the escape velocity using the energy balance equation

$$\frac{1}{2}(M_1 - m_{max,1} + M_2 - m_{max,2})V_{esc}^2 + W_{tot} = W_{fr,1} + W_{fr,2} + W_h, \tag{6.25}$$

where W_{tot} is the total gravitational energy just before impact

$$W_{tot} = -\frac{3GM_1^{5/3}}{5Q} - \frac{3GM_2^{5/3}}{5Q} - \frac{GM_1M_2}{QM_1^{1/3} + QM_2^{1/3}}, \tag{6.26}$$

where

$$Q = \left(\frac{4\pi\rho}{3}\right)^{-1/3}. \tag{6.27}$$

W_{fr} is the gravitational potential energy of the fragments resulting from a catastrophic collision

$$\begin{aligned} W_{fr} &= -\frac{3G}{5Q}\int_{m=0}^{m=\infty} m^{5/3}\mathrm{d}N \\ &= -\frac{3G}{5Q}\frac{3b_1B_1m_{max}^{5/3-b_1} - 3b_1B_1m_t^{5/3-b_1}}{5-3b_1} - \frac{3Gm_{max}^{5/3}}{5Q} - \frac{3G}{5Q}\frac{3b_2B_2m_t^{5/3-b_2}}{5-3b_2} \\ &= -\frac{3G}{5Q}\frac{5m_{max}^{5/3} - 3b_1B_1m_t^{5/3-b_1}}{5-3b_1} - \frac{3G}{5Q}\frac{3b_2B_2m_t^{5/3-b_2}}{5-3b_2}, \end{aligned} \tag{6.28}$$

where dN is the differential mass distribution from Eq. 6.3. In the case of a cratering impact, this term is replaced by

$$W_{crat} = \frac{3G}{5Q}\frac{5m_{max}^{5/3} - 3b_1B_1m_t^{5/3-b_1}}{5-3b_1} - \frac{3G}{5Q}\frac{3b_2B_2m_t^{5/3-b_2}}{5-3b_2} - \frac{3G(M-M_{crat})^{5/3}}{5Q}, \tag{6.29}$$

where the last term accounts for the gravitational potential energy of the cratered body. The term W_h is an estimate of the gravitational potential energy of the fragments separated by a distance on the order of the Hill radius, and is given by

$$W_h = -\frac{3G(M_1+M_2)^{5/3}}{5}\frac{(3M_{sun})^{1/3}}{R_o} \tag{6.30}$$

for the case where both bodies are shattered,

$$W_h = -\frac{3G(M_1-M_{crat,1})^{2/3}(M_2+M_{crat,1})}{2}\frac{(3M_{sun})^{1/3}}{R_o} \tag{6.31}$$

for the case where one body is shattered and the other is cratered, and

$$W_h = -\frac{3G(M_1+M_2-M_{crat,1}-M_{crat,2})^{2/3}(M_{crat,1}+M_{crat,2})}{2}\frac{(3M_{sun})^{1/3}}{R_o} \tag{6.32}$$

for the case where both bodies are cratered. M_{sun} is the mass of the sun and R_o is the orbital radius where the collision occurs, which is on the order of 2.5 AU for the asteroid belt. The last two W_h expressions are corrections to the Petit and Farinella (1993) model. They used Eq. 6.30 for all cases, and that expression breaks down at very small projectile/target mass ratios, giving positive values rather than negative and causing V_{esc} to be artificially lowered (to zero in some cases) and therefore allowing many more fragments to escape than should actually be able to. This causes significant problems when used in a full-scale collisional evolution model.

Once the different W terms are calculated, Eq. 6.25 can be solved for the escape velocity V_{esc} and the reaccumulation process can be treated. In the simple deterministic case, the fragment velocities are calculated directly from Eq. 6.16. If the fragments in any element of arrays F_1 and F_2 have a velocity larger than V_{esc}, they escape the gravitational well and stay in the array. If the fragments have a velocity smaller than V_{esc}, they are added to the reaccumulated mass and removed from their respective F_i array..

In a more realistic approach, a probabilistic velocity distribution

$$P(v; V_{rms}) = \sqrt{\frac{2}{\pi}} \frac{3\sqrt{3}v^2}{V_{rms}^3} \exp\left(-\frac{3v^2}{2V_{rms}^2}\right) \tag{6.33}$$

is assumed, where V_{rms} is the RMS velocity of fragments of a given mass (calculated from Eq. 6.16). In the case of a small number of fragments in a given bin, the velocity of each fragment is calculated at random assuming the probability distribution given in Eq. 6.33. Fragments faster than V_{esc} stay in their respective F_i array and the slower ones are removed and added to the reaccumulated mass. For bins with a large number of fragments, the fraction of fragments that escape the gravity well and remain in the array is calculated from

$$
\begin{aligned}
f_{esc} &= \int_0^{V_{esc}} P(v; V_{rms}) \mathrm{d}v \\
&= -\frac{2}{\sqrt{\pi}} \sqrt{\frac{3}{2}} \frac{V_{esc}}{V_{rms}} \exp\left(-\frac{3V_{esc}^2}{2V_{rms}^2}\right) + \operatorname{erf}\left(\sqrt{\frac{3}{2}} \frac{V_{esc}}{V_{rms}}\right),
\end{aligned}
\tag{6.34}
$$

where

$$
\operatorname{erf}(v) = \frac{2}{\sqrt{\pi}} \int_0^v \exp\left(-x^2\right) \mathrm{d}x \tag{6.35}
$$

Once the reaccumulated fragments have been removed from the arrays F_1 and F_2, Eqns. 6.8 and 6.9 are used, along with Eqns. 6.17 and 6.19, to determine the mass below the smallest bin that is reaccumulated (the 'reaccumulated tail' of the distribution). F_1 and F_2 are then merged into a single fragment array F. The reaccumulated fragments are added together, along with the reaccumulated tail and the largest fragments m_{max} in the case of catastrophic fragmentation events and/or the cratered bodies in the case of cratering events, to give a single reaccumulated body of mass M_r that is placed at the appropriate point in the F array. In addition, the initial bodies of masses M_1 and M_2 are subtracted from the F array. The F array, therefore, takes into account all of the bodies removed by a given collision (the initial bodies) as well as all of the new bodies created (the fragments plus the reaccumulated body).

6.1.2 Full Model

The algorithm outlined in the previous section can be used to calculate the outcome of a collision between any pair of bodies. In this section, we describe a full collisional and dynamical model based on this algorithm that is capable of tracking the simultaneous evolution of both the NEA and main-belt populations. To construct such a model, we must know the intrinsic collision probability P_i, which describes how frequently collisions occur, and the mean collision velocity $\langle V \rangle$. Bottke and Greenberg (1993) and Bottke et al. (1994b) calculated P_i and $\langle V \rangle$ for collisions between main-belt asteroids, and Bottke et al. (1994a) calculated these values for collisions between NEAs and between NEAs and main-belt objects. These values are given in Table 6.1. $\langle V \rangle$ for NEA-MB collisions is nearly twice that for collisions in the main belt, and $\langle V \rangle$ for NEA-NEA collisions is even higher, due to the larger eccentricities of NEAs versus main-belt objects.

Collision Velocities and Probabilities

	P_i (km^{-2} yr^{-1})	$\langle V \rangle$ (m/s)
MB-MB	2.86×10^{-18}	5.3×10^3
NEA-MB	2.18×10^{-18}	10.2×10^3
NEA-NEA	15.3×10^{-18}	18.5×10^3

Table 6.1: Collision Velocities and Probabilities from Bottke and Greenberg (1993) and Bottke et al. (1994b) for the main belt and Bottke et al. (1994a) for NEAs.

The intrinsic collision probability has units of km^{-2} yr^{-1}, and can be used to calculate the frequency of collision between a single 'target' of radius r_t and a single 'projectile' of radius r_p with the equation

$$f = P_i(r_t + r_p)^2. \tag{6.36}$$

Multiplying Eq. 6.36 by the number of target-projectile pairs N_{pairs}, and the time interval Δt gives the total number of collisions during Δt

$$n_{coll} = P_i(r_t + r_p)^2 N_{pairs} \Delta t. \tag{6.37}$$

For cases where the targets and projectiles in question are in the same size bin and population (i.e. MB or NEA), their numbers N_t and N_p are equal and

$$N_{pairs} = \frac{N_t(N_p - 1)}{2}. \tag{6.38}$$

For all other cases,

$$N_{pairs} = N_t N_p. \tag{6.39}$$

We start with initial main-belt and NEA population arrays N_{MB} and N_{NEA}, binned in logarithmic increments of 0.1 in diameter (which is about a factor of two in mass). The main-belt population can start in any configuration, but the NEA population always starts with zero bodies. Using the algorithm outlined in the previous section, along with the input parameters such as the size-dependent strength parameters Q_S and f_{KE}, the velocity distribution exponent k, the density ρ, cratering efficiency α, and the fragment distribution ratios r_m and r_b, we generate 3-D matrices $F^{i,j,k}$ that give the fragment distribution resulting from collisions between bodies in any two size bins, where i is the target index, j is the projectile index, and k is the fragment index. The F matrices are symmetrical with regards to target and projectile, such that element (i, j, k) is equal to element (j, i, k). F_{MB} is for collisions between main-belt objects, F_{NEA} is for collisions between NEAs, and F_{MN} is for collisions between main-belt asteroids and NEAs. Additional 2-D matrices $f^{i,j}$ are generated, using Eq. 6.36, that give the frequency of collisions between bodies in any two size bins (f_{MB} for main-belt collisions, f_{NEA} for collisions between NEAs, and f_{MN} for collisions between NEAs and main-belt asteroids). The fragments resulting from an NEA-MB collision are assumed to stay in the NEA population when the NEA is larger then the main-belt asteroid and stay in the main-belt when the main-belt asteroid is larger.

Non-collisional removal processes act in parallel with collisional processes and transfer material from the main belt to the NEA population. f^k_{rem} is the non-collisional removal rate, parameterized as the fraction of bodies in a given size bin removed per unit time. In addition, dynamical processes remove material from the NEA population, such that bodies in the NEA population have a mean lifetime $\langle \tau_{nea} \rangle$, as discussed in Chapter 4.

In a given timestep Δt, the change in the main-belt population due to collisions and non-collisional removal is given by

$$\begin{aligned} \Delta N^k_{MB} &= \sum_{i=1}^{i=n} \sum_{j=1}^{j=i} \Bigg[F^{i,j,k}_{MB} f^{i,j}_{MB} N^i_{MB} \frac{N^j_{MB} - \delta_{ij}}{1 + \delta_{ij}} \\ &+ (F^{i,j,k}_{MN} + \delta_{jk}) f^{i,j}_{MN} N^i_{MB} N^j_{NEA} (1 - \delta_{ij}) - \delta_{jk} f^{i,j}_{MN} N^i_{NEA} N^j_{MB} \\ &- f^k_{rem} N^k_{MB} \Bigg] \Delta t \end{aligned} \tag{6.40}$$

where n is the total number of size bins. The projectile index j ranges from 1 to i rather than 1 to n because of the symmetrical nature of the F matrices. The first term is the change resulting from MB-MB collisions, the terms on the second line are due to MB-NEA collisions, and the term on the last line is due to non-collisional removal. The change in the NEA population due to collisions, the influx of material from the main belt, and dynamical removal is

$$\begin{aligned} \Delta N^k_{NEA} &= \sum_{i=1}^{i=n} \sum_{j=1}^{j=i} \Bigg[F^{i,j,k}_{NEA} f^{i,j}_{NEA} N^i_{NEA} \frac{N^j_{NEA} - \delta_{ij}}{1 + \delta_{ij}} \\ &+ (F^{i,j,k}_{MN} + \delta_{jk}) f^{i,j}_{MN} N^i_{NEA} N^j_{MB} - \delta_{jk} f^{i,j}_{MN} N^i_{MB} N^j_{NEA} (1 - \delta_{ij}) \\ &+ f^k_{rem} N^k_{MB} - \frac{N^k_{NEA}}{\langle \tau_{nea} \rangle} \Bigg] \Delta t. \end{aligned} \tag{6.41}$$

The first term is the change resulting from NEA-NEA collisions, the terms on the second line are due to MB-NEA collisions, and the terms on the last line are due to the influx of material from the main belt and the dynamical removal of NEAs.

A simplified version of these equations, which neglects MB-NEA and NEA-NEA collisions, is

$$\begin{aligned}
\Delta N^k_{MB} &= \sum_{i=1}^{i=n}\sum_{j=1}^{j=i}\left[F^{i,j,k}_{MB} f^{i,j}_{MB} N^i_{MB}\frac{N^j_{MB}-\delta_{ij}}{1+\delta_{ij}} - f^k_{rem}N^k_{MB}\right]\Delta t \qquad (6.42)\\
\Delta N^k_{NEA} &= \sum_{i=1}^{i=n}\sum_{j=1}^{j=i}\left[f^k_{rem}N^k_{MB} - \frac{N^k_{NEA}}{\langle\tau_{nea}\rangle}\right]\Delta t. \qquad (6.43)
\end{aligned}$$

We integrate these equations in time using an adaptive stepsize routine that makes sure that the number of asteroids in any bin doesn't change by more than a certain amount (generally 1%).

Whatever size we choose for the lower limit of the N_{MB} and N_{NEA} arrays, the bodies that can collisionally disrupt the smallest bodies in the arrays are generally smaller than that lower limit. Ignoring the disruption of the smallest bodies leads to 'waves' in the size distribution that would not necessarily be physical (Campo Bagatin et al., 1994; Durda and Dermott, 1997). To prevent this, we fix the lower 2 decades of the main-belt population in our model (generally 1 mm to 10 cm) and use that part of the population only for calculating the collision rates with larger bodies (i.e. we do not collisionally evolve it). The slope and number of bodies in that portion of the population is calculated each timestep by extrapolating from the population of larger bodies that do undergo collisional evolution (generally bodies larger than 10 cm).

Dynamical models (Petit et al., 1999; Petit et al., 2001) indicate that the early asteroid belt may have been hundreds of times more massive than it currently is and was cleared of most of its mass by gravitational interactions with Jupiter and planetary embryos in the early solar system (probably on a timescale of a few Myr). Our model gives the option of multiplying the initial population by a constant factor during the first phase of evolution in order to simulate this.

6.2 Effects of Different Collisional Parameters

In this section, we illustrate the dependence of the final collisionally evolved population on the various input parameters by varying one parameter at a time while holding the others constant. The following default values are used, unless otherwise noted: $\rho = 2700$ kg/m^3, $\alpha = 10^{-4}$ s^2/m^2, $r_b = r_m = 1$, $V_{max} = 3000$ m/s, and $k = 2.25$. The mean collision velocity and intrinsic collision probability are the main-belt values from Table 6.1, and non-collisional removal is not included (i.e. $f_{rem} = 0$ at all sizes). We collisionally evolve all bodies in the size range from 1 m to 1000 km, and as explained in the previous section, we extrapolate the population below 1 m in order to determine the number of projectiles there.

Q^*_D is held constant in all cases. Q^*_D is not an input parameter to our model, but is calculated in our numerical code from the other input parameters, primarily Q_S and f_{KE}. Thus, we adjust Q_S and f_{KE} to get a given Q^*_D, which in the following cases is the Benz and Asphaug (1999) hydrocode Q^*_D law for basalt shown in Fig. 2.8. We parameterize f_{KE} as a power law of the form

$$f_{KE} = f_{KE_o} \left(\frac{D}{1000 \text{ km}} \right)^{\gamma}, \tag{6.44}$$

where γ is on the order of 0.5 (always between 0 and 1) and f_{KE_o}, the value at 1000 km, is generally $\sim$ 0.05-0.3, reasonably consistent with estimates of f_{KE} in large impacts (e.g. Davis et al. (1989)). Note that this function gives an f_{KE} for centimeter-scale targets that is smaller than that found in many laboratory experiments (e.g. Nakamura and Fujiwara (1991)). However, even with a very low value of f_{KE}, the fragments from collisions between bodies smaller than a few hundred meters all still have enough energy to escape, so our approximation, while not necessarily valid at small sizes, does not cause any non-physical results.

Figure 6.1 shows a set of five Q_S curves that, for appropriate f_{KE} values,

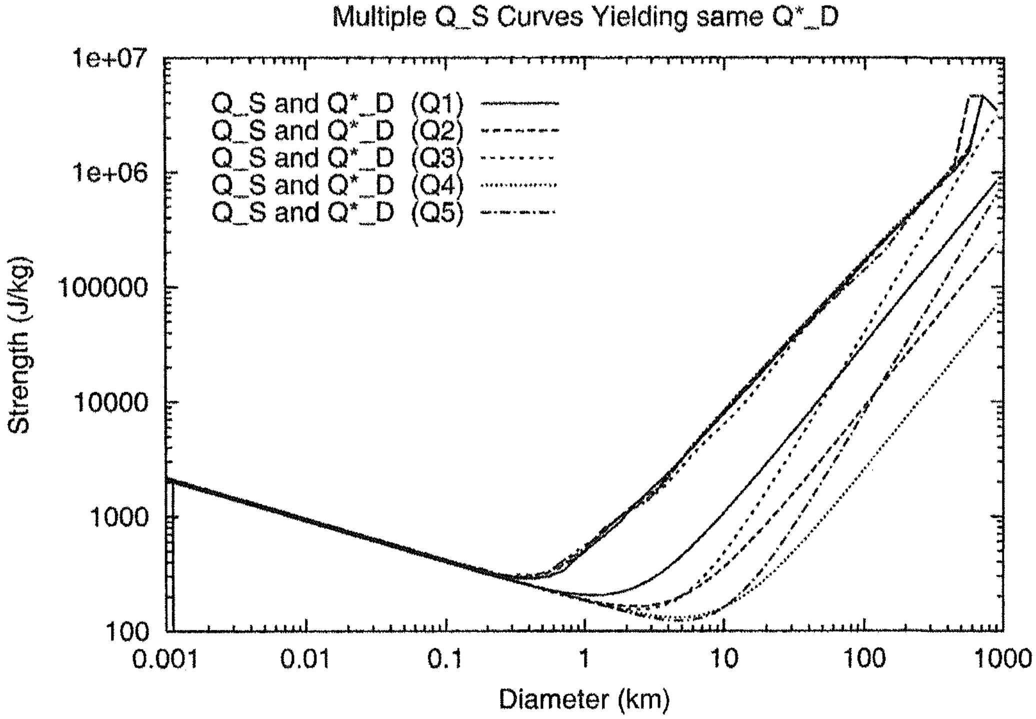

Figure 6.1: Plot of different Q_S curves that yield the same Q^*_D. For each Q_S curve, f_{KE} is defined as a power law with coefficients such that, in our simulations, the combination of Q_S and f_{KE} yields a Q^*_D curve equivalent to the Benz and Asphaug (1999) curve for basalt (see Fig. 2.8). The slight 'jump' in Q^*_D at the largest sizes is not real—it is an artifact of how our code calculates Q^*_D when the size of the projectile necessary to disrupt a given target is larger than the target itself.

yield the Benz and Asphaug (1999) Q_D^* law for basalt. Figure 6.2 shows the results of 4.5 Gyr numerical simulations using those strength parameters. Even though Q_D^* is the same for all cases, the wave amplitude differs significantly between them. In general, simulations with the largest gaps between Q_S and Q_D^* (such as case Q4) have the largest wave amplitude. The positions of the peaks and valleys of the wave, however, remain essentially he same. This indicates that Q_D^* is the primary determining factor for the general shape of the population.

Q_S is important with regards to the Vesta constraint. The smaller Q_S is for 500 km bodies (the diameter of Vesta), the more likely it is that Vesta would be shattered. In case Q2 there is about a 50% chance that Vesta will experience an impact that catastrophically fragments it and in case Q4 the likelihood is almost 100%. Thus, to best satisfy the Vesta constraint, it is necessary to have a high Q_S for 500 km-scale bodies.

Since our simulations treat cratering debris as well as the fragments from catastrophic disruption of bodies, it is necessary to determine the sensitivity of the final population to the cratering efficiency α from Eq. 6.13. Larger α means that the mass of cratering debris will be larger for a given impact. Figure 6.3 shows a plot of the final evolved population after 4.5 Gyr for $\alpha = 10^{-15}$ s^2/m^2, which corresponds to essentially no cratering debris, $\alpha = 10^{-5}$ s^2/m^2 (the value for 'hard' materials like rock (Dobrovolskis and Burns, 1984)), and $\alpha = 10^{-3}$ (larger than estimates for 'soft' materials such as sand (Stoeffler et al., 1975)). The Q_S used is the curve Q1 in Fig. 6.1, and f_{KE} is adjusted to get the Benz and Asphaug Q_D^*. There is minimal difference in the evolved population at large sizes, indicating that cratering debris has a negligible effect in this size range. There is a factor of a few difference at the smallest sizes.

We also performed several simulations to determine the effect of the maximum fragment ejection velocity V_{max} and the exponent k of the fragment velocity

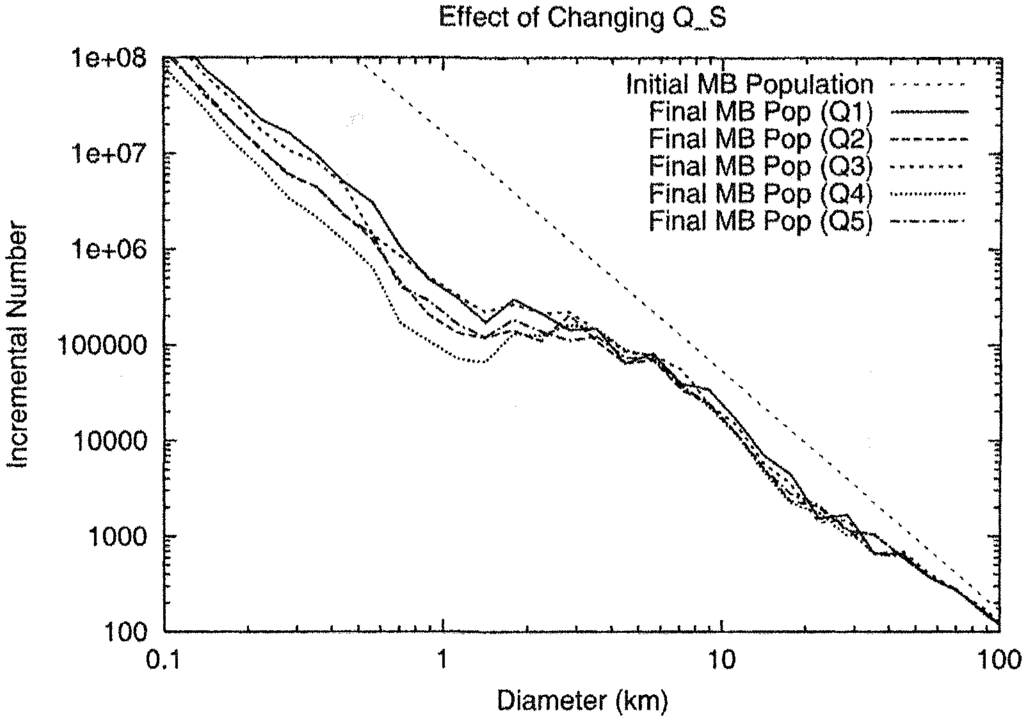

Figure 6.2: Plot of the final evolved asteroid population (after 4.5 Gyr) using the Q_S curves in Fig. 6.1 and their associated f_{KE} values. This figure focuses on the 'wavy' region of the population. Even though Q_D^* is the same for all cases, the wave amplitude differs significantly between them. The position of the peaks and valleys of the wave, however, is essentially the same.

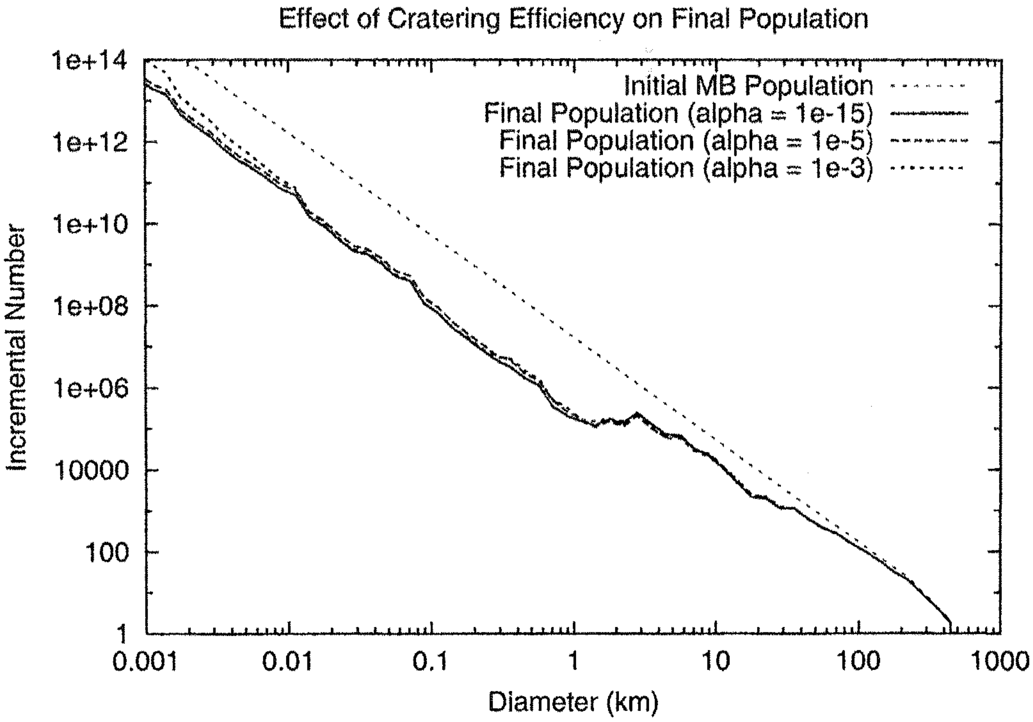

Figure 6.3: Plot of the dependence of the final evolved asteroid population on the cratering efficiency α from Eq. 6.13. The population is evolved for 4.5 Gyr using the Benz and Asphaug (1999) Q_D^* scaling law for basalt at 5 km/s. $\alpha = 10^{-15}$ s^2/m^2 corresponds to essentially no cratering, while $\alpha = 10^{-3}$ s^2/m^2 is larger than the highest estimates in the literature. α has little effect at the large end of the population, but large values of α can increase the numbers of the smallest bodies by a factor of a few.

distribution from Eq. 6.15. Varying V_{max} between 500 and 5000 m/s while keeping Q_D^* fixed causes very little change in the final population after 4.5 Gyr. With curve Q1 in Fig. 6.1 used for Q_S, very little adjustment of f_{KE} is necessary to keep Q_D^* constant. Similarly, varying k from 2.001 to 2.5 while keeping Q_D^* fixed has little effect on the final population. The magnitude f_{KE_o}, but not the slope γ of f_{KE} from Eq. 6.44, was varied by about a factor of 2 to keep Q_D^* constant while varying k.

The initial population is an important input parameter. The largest bodies in the asteroid population (hundreds of km in diameter) have probably not fully reached a collisional steady state due to the difficulty of fragmenting them and the small number of projectiles capable of doing so. Therefore, the slope of the initial population for bodies larger than a few hundred km is likely to be preserved in the current population. Using an initial population with significantly more mass than the current mass of few-hundred-km asteroids increases the likelihood of catastrophically disrupting them, and thus forming too many large asteroid families or destroying Vesta's basaltic crust. In addition, using a steep initial population vs. a shallow initial population can lead to significantly different evolved populations. In the steep case, there are initially a large number of small bodies that are ground down to give the final population. In the shallow case, there are few small bodies until collisions between large bodies occur and create a population of small bodies. After an infinite time, the evolved population in both cases should be essentially identical, but over a finite time, the evolved populations will not necessarily converge. This situation is accentuated when non-collisional removal is included.

6.3 Results

The following default values are used, unless otherwise noted: $\alpha = 10^{-4}$ s^2/m^2, $r_b = r_m = 1$, $V_{max} = 3000$ m/s, and $k = 2.25$. The mean collision velocity and intrinsic collision probability are those given in Table 6.1. We assume that all bodies have $\rho = 2700$ kg/m^3, consistent with the densities of several S-type asteroids that have good density estimates (Belton et al., 1995; Belton et al., 1996; Veverka et al., 2000)[1]. We collisionally evolve all bodies in the size range from 0.1 meter to 1000 km, and as explained previously, we extrapolate the population below 0.1 meter in order to determine the number of projectiles there.

Given the positions of the first peak and valley in the observed main-belt size distribution (Fig . 2.1), we can use the analytical theory in Chapter 3 to find a family of Q_D^* curves that should give those peaks and valleys. For a given D_t, the transition diameter for the Q_D^* law, we numerically solve Eqns. 3.39 and 3.40 to give the gravity regime slope s_g and Q_D^* value at D_t needed to reproduce the peaks and valleys in the size distribution. The slope s_s of Q_D^* in the strength regime is chosen so as to match the strength of targets in laboratory experiments ($\sim 3 \times 10^3 - 4 \times 10^3$ J/kg for 10 cm-scale targets when averaged over all possible impact angles). As noted in Section 3.4, the positions of the peaks and valleys predicted by the analytical model are offset somewhat from the results of numerical models by $\sim$ 30%. We therefore had to iterate somewhat between our numerical simulation and the analytical theory in order assure that the family of curves we found accurately reproduces the observed peak and valley positions. Figure 6.4 shows the family of Q_D^* curves that we calculate.

We tested 5 of the Q_D^* curves from Fig. 6.4, varying Q_S and f_{KE} as necessary to obtain the desired Q_D^*, and the main-belt simulations run with them all fit the observed positions of the peaks and valleys remarkably well, despite varying in slope and wave amplitude. We then incorporated the non-collisional removal rates f_{rem} from Figure 5.7 into our model to treat the full collisional and dynamical evolution of both the MB and NEA populations. For the NEA mean lifetime, we

---

[1] In reality, asteroids span a range of compositions and densities, from porous, low-density C-types like Mathilde (Veverka et al., 1999) to the M-types, many of which may be metallic (Bell et al., 1989).

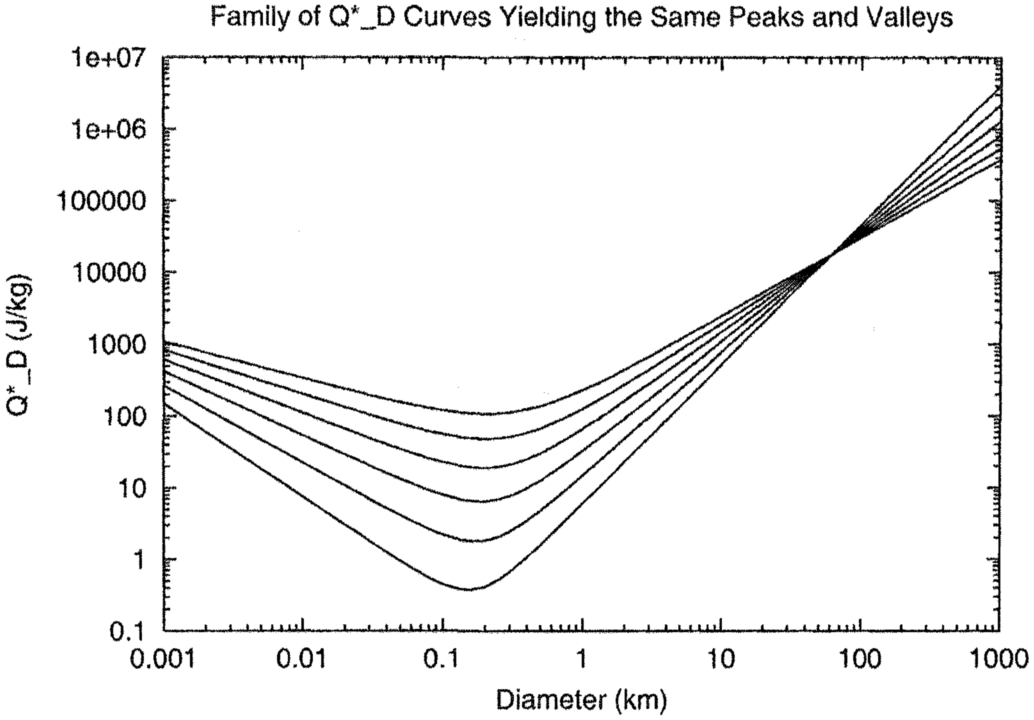

Figure 6.4: Representative members of a family of Q_D^* curves that can potentially reproduce the positions of peaks and valleys in the main-belt size distribution, calculated based on the analytical theory in Chapter 3 as described in the text.

use $\langle\tau_{nea}\rangle = 1.14$ Myr, the average from all main-belt sources from Bottke et al. (2002) as discussed in Chapter 4. We varied f_{rem} somewhat from the values in Fig. 5.7, as those values are only an estimate, albeit a reasonable one. In addition, we varied the parameters Q_S and F_{KE} to explore the range around a given Q_D^* curve.

We compared the output of all of our simulations to constraints 1-5 from Section 2.1: (1) the main-belt and (2) the NEA size-distributions; (3) the lifetimes of meter-sized bodies from meteorite CRE ages; (4) the number of large asteroid families; And (5) the existence of Vesta's basaltic crust. The simulation that we find best fits these constraints is shown in Figs. 6.5-6.9. The main-belt population in our simulation is a good fit to the observed main-belt population, as shown in Fig. 6.5. The Q_D^* and Q_S curves (Fig. 6.6) are reasonable compared to independent estimates of asteroid strength shown in Figs. 2.7 and 2.8. The lifetimes of meter-scale bodies in our simulation, about 8 Myr, are reasonably consistent with CRE ages for stony meteorites (Fig. 6.7). 7 families are formed by the breakup of 200 km or larger bodies, reasonably consistent with the 8 observed large families, and a Vesta-sized body has $\sim$ 70% chance of surviving 4.5 Gyr without being catastrophically fragmented, which is consistent with the observation of an intact basaltic crust on Vesta.

The non-collisional removal rates we use (Fig. 6.8) are consistent with our own estimate from Fig. 5.7. In addition, they result in 810 bodies larger than 1 km being removed from the main-belt per million years, consistent with the estimate of Bottke et al. (2002), and give an NEA population (Fig. 6.9) that is fairly consistent with observational estimates, assuming an albedo p_V of 0.11. Assuming a larger albedo for small NEAs, as discussed in Sec. 2.1.2, decreases the goodness-of-fit. In Fig. 6.9, there is a deficit of large NEAs relative to observational estimates. This is potentially due to our use of a single NEA mean lifetime $\langle\tau_{nea}\rangle = 1.14$ Myr that is the average value for all NEA source regions. As discussed in Chapter 4, the largest NEAs may come preferentially through the IMC source region, which has

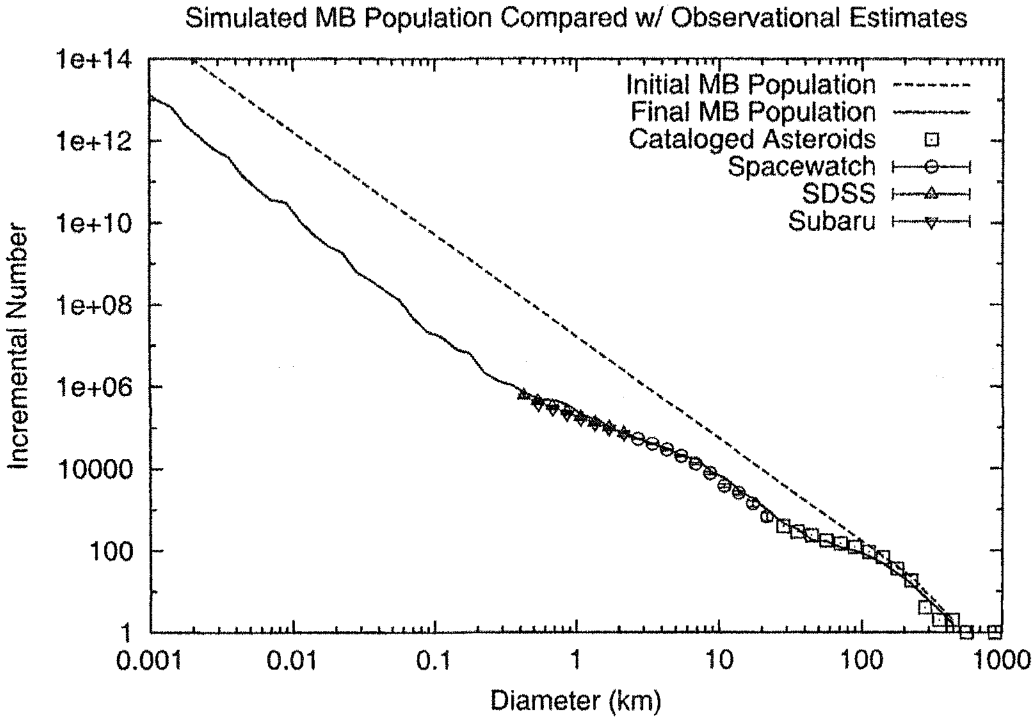

Figure 6.5: Best-fit main-belt population from our simulations. Data points show observational estimates of the actual main-belt population.

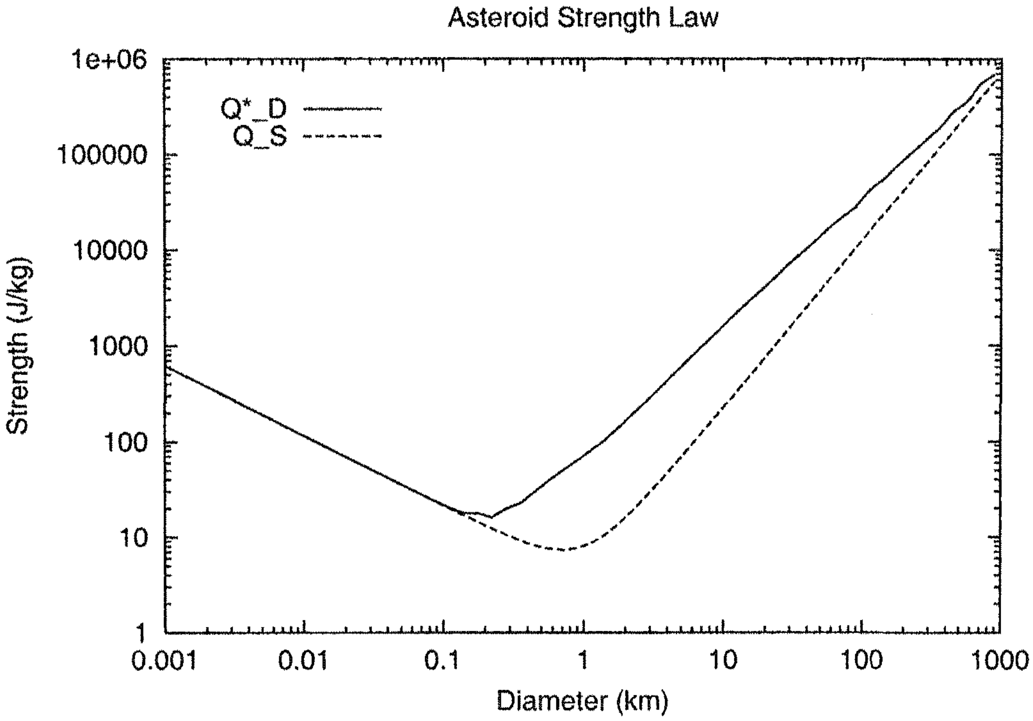

Figure 6.6: Strength law used for the best-fit main-belt population shown in Fig. 6.5

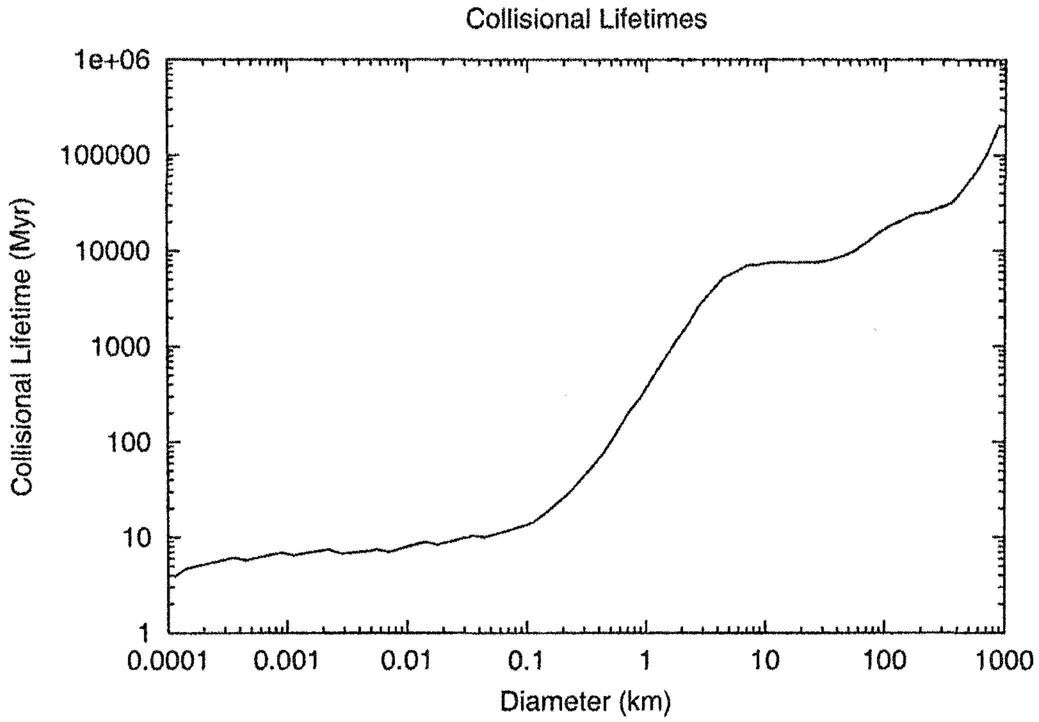

Figure 6.7: Calculated mean collisional lifetimes of bodies in the best fit-population shown in Fig. 6.5. Meter-scale bodies have mean collisional lifetimes around 8 Myr.

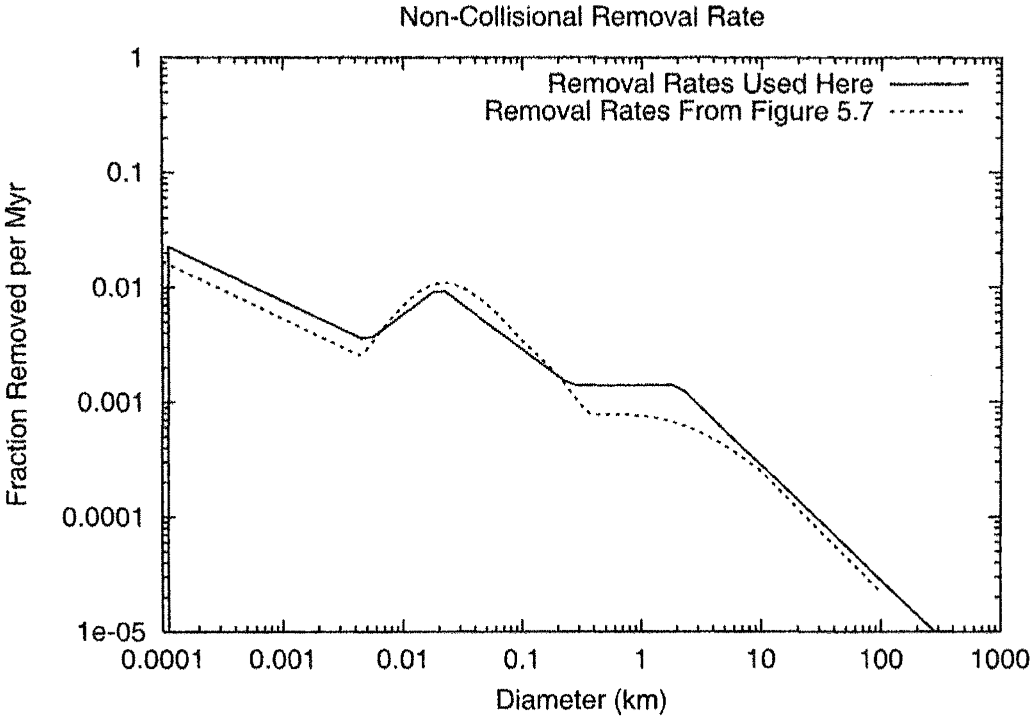

Figure 6.8: Non-collisional removal rates used for best-fit population in Fig. 6.5, compared to our estimate from Fig. 5.7. 810 asteroids larger than 1 km are removed per Myr, consistent with the estimate of Bottke et al. (2002).

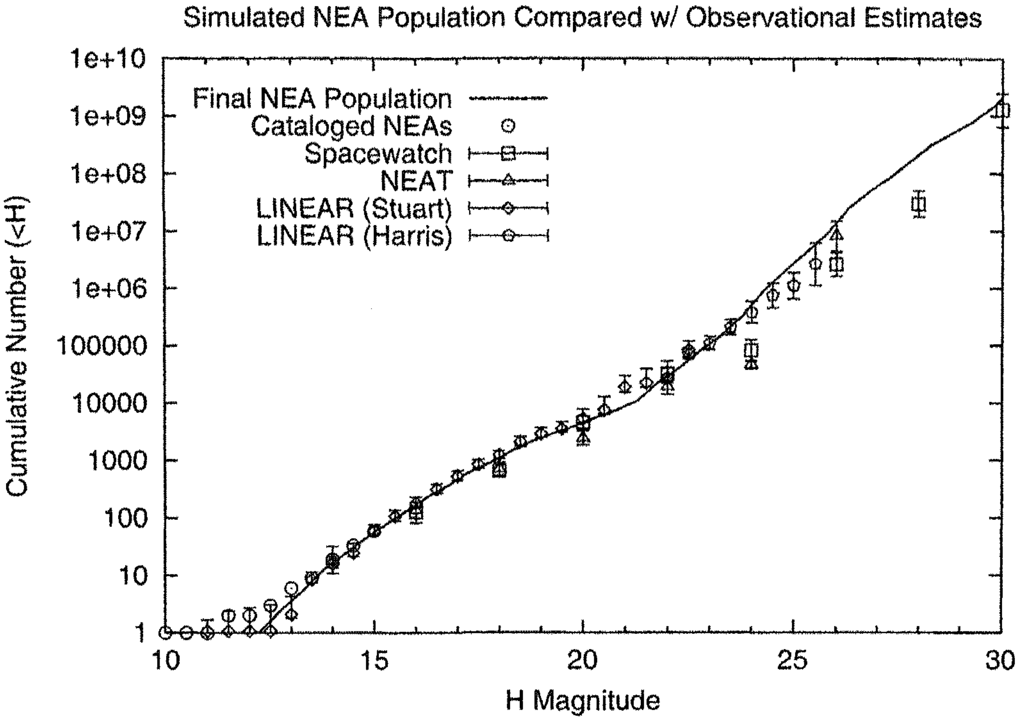

Figure 6.9: Simulated NEA population resulting from non-collisional removal from the main-belt population in Fig. 6.5 at the rates given in Fig. 6.8. Our results are converted from diameter to H magnitude assuming an albedo p_V of 0.11. Data points show observational estimates of the actual NEA population. Assuming a constant albedo, as the H-magnitude of a body increases, its diameter decreases. The deficit of large NEAs relative to observational estimates is potentially due to our use of a single NEA mean lifetime $\langle \tau_{nea} \rangle$ rather than a size-dependent $\langle \tau_{nea} \rangle$, as discussed in the text.

a $\langle\tau_{nea}\rangle$ of 3.75 Myr. Using that value of $\langle\tau_{nea}\rangle$ for the largest NEAs would boost their numbers by a factor of ~ 3.5 in our model, making our results more consistent with the observations.

Our best-fit results were obtained by including a brief period of primordial evolution at the beginning the simulation, as described in Section 6.1.2. The initial population was multiplied by a factor of 250 and collisionally evolved for 5 Myr, then reduced by a factor of 250 and collisionally evolved for the remainder of the 4.5 Gyr. A brief period of intense collisional evolution such as this is predicted by several models (Petit et al., 1999; Petit et al., 2001). The effect in this case is roughly similar to an additional 1.25 Gyr of collisional evolution or a P_i that is about 25% larger.

We used a steep initial population (differential slope of -3.5 below 200 km and -4.5 above), as shown in Fig. 6.5, rather than a very shallow one (-1 slope), as the steep initial population led to the better fit for nearly all of the simulations we ran. Using an initial population significantly more massive than this results in a higher chance of shattering Vesta and the formation of too many large asteroid families. We also found that in nearly all of our simulations, using a broken power-law fragment distribution ($r_b < 1$) resulted in wave amplitudes in the main belt that were far too high to match observations, despite the fact that a broken power-law size distribution is more physically realistic. We will address this again in the conclusion.

The inclusion of non-collisional removal processes based on reasonable estimates of their magnitudes is capable of perturbing the size distribution of the main-belt, and indeed some 'tweaking' of the removal rates is necessary to give the best fit. The effects of including non-collisional removal in our simulations can be seen in a comparison of the best-fit population shown in Fig. 6.5 with Fig. 6.10, which shows the results of a simulation with parameters identical to those used for

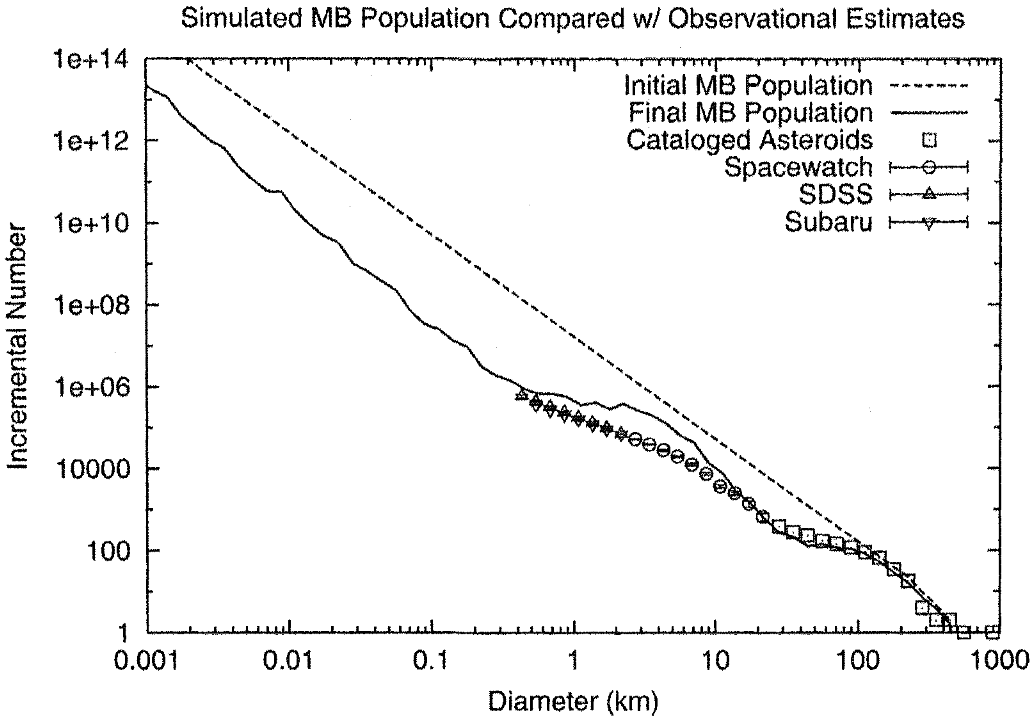

Figure 6.10: Simulation run with the same parameters as the best-fit population in Fig. 6.5, but with no non-collisional removal. Data points show observational estimates of the actual main-belt population.

Fig. 6.5, but with no non-collisional removal. While non-collisional removal can perturb the population, it is not strong enough to give the orders-of-magnitude depletion of small asteroids that has been invoked to explain the lack of small craters on Eros (Chapman et al., 2002) or the steepness of Gaspra's cratering record (Hartmann and Ryan, 1996). Our simulations demonstrate that collisional debris quickly replaces the bodies lost through resonances and the Yarkovsky effect, thus preventing a runaway depletion even for unreasonably large removal rates.

Our simulations also indicate that most meter-scale asteroids, some of which are eventually delivered to Earth as meteorites, are formed from the breakup of large, multi-kilometer to 100 km parent bodies rather than smaller ones. Our finding that meteorite-sized bodies are primarily produced from large parent bodies is consistent with the small number of meteorites that have positively-identified complex CRE histories, as most material in multi-kilometer asteroids would be shielded from cosmic rays until liberated by a collision. Other models, however, predict that complex exposure histories should be common and the immediate precursors of meteorites should therefore be on the order of 10 meters or less in diameter (Wetherill, 1985; Vokrouhlický and Farinella, 2000). It is unclear whether those simulations or our simulation is more correct with regards to the size of meteorite parent bodies.

In the next chapter, we address the final constraint—how well our main-belt population matches the observed cratering records on asteroids.

CHAPTER 7

Comparison to Asteroid Cratering Records

In this chapter we use a model based on Greenberg et al. (1994, 1996) to show that the main-belt asteroid population we have found from our collisional/dynamical evolution modeling in Chapter 6 is consistent with the crater records on Gaspra, Ida, Mathilde, and Eros, the four asteroids that have been observed by spacecraft.

7.1 Properties of Asteroids Observed by Spacecraft

Four asteroids have been observed at fairly high resolution by spacecraft flybys or orbital tours—Gaspra and Ida by the Galileo spacecraft, and Mathilde and Eros by the NEAR spacecraft. Of these all are S-type asteroids except for Mathilde, which is a C-type, and all lie in the main belt except for Eros, which is an NEA. The properties of these asteroids are summarized in Table. 7.1

7.2 Crater Production

Nolan et al. (1996) performed hydrocode simulations to estimate crater size as a function of impactor size for a Gaspra-sized spherical body. The same results, scaled to Ida, appear in Greenberg et al. (1996). The Nolan et al. simulations were performed using half-spaces for impactors smaller than 60 m and spherical targets for larger impactors, with all impacts occurring at 5.3 km/s and assuming a projectile and target density of 2700 kg/m^3. These simulations do not take into account viscosity in the excavation flow, which could serve to reduce the final crater

Physical and Orbital Parameters of Observed Asteroids

Asteroid	Type	Size (km)	$\bar{r}$ (km)	ρ (kg/m^3)	q (AU)	Q (AU)	$\langle V \rangle$ (m/s)	P$_\mathrm{i}$ (km^{-2}yr)
Gaspra	S	19 x 12 x 11	6.1	n/a	1.83	2.59	5.0	2.80
Ida	S	56 x 24 x 21	15.7	2600	2.73	2.99	3.55	3.83
Mathilde	C	66 x 48 x 44	26.4	1300	1.95	3.35	5.3	2.86
Eros	S	34 x 11 x 11	8.46	2670	1.13	1.79	5.3	2.86

Table 7.1: Properties of asteroids that have been observed by spacecraft. Triaxial ellipsoid dimensions are from Belton et al. (1992), Belton et al. (1994), Veverka et al. (1999), and Veverka et al. (2000). Mean radii are from Thomas et al. (1994), Thomas et al. (1996), Veverka et al. (1999), and Thomas et al. (2002). Densities are from Belton et al. (1995) and Belton et al. (1996), Veverka et al. (1999), and Veverka et al. (2000). A density estimate is not available for Gaspra, but is likely similar to the other S-types. The perihelion q and aphelion Q are calculated from the orbital elements in the JPL DASTCOM database. $\langle V \rangle$ and P_i are from Bottke and Greenberg (1993) and Bottke et al. (1994b), which give values for Gaspra and Ida explicitly and main-belt average values that are used for Mathilde and Eros.

diameter somewhat, so the diameters given are an upper limit.

Nolan et al. find two distinct cratering regimes in their simulations. Craters smaller than about 6 meters in diameter form in the 'strength regime', where the crater diameter is linearly proportional to the projectile diameter, indicating that material strength is what limits the final crater diameter (Melosh, 1989). Craters larger than this (up to about 10 km in diameter) form in what they refer to as the 'fracture regime.' In this regime, the shock wave from the impact precedes the excavation flow, fracturing the material such that the excavation flow has no material strength to overcome. The final crater size is determined by the size of the fractured region.

While Nolan et al. do not include gravity in their simulations, they use Pi-group scaling (Holsapple and Schmidt, 1982; Melosh, 1989) to show that craters larger than about 10 km on Gaspra form in the 'gravity regime', where crater size is limited by the amount of material that can be excavated from the crater against gravity. Scaling theories generally deal with craters that form in cases where the curvature of the target is negligible, such as most impacts on the terrestrial planets and large planetary satellites. For large impacts on asteroids, where the impactor diameter can be a significant fraction of the target diameter, these scaling laws likely lose some accuracy. However, better accuracy can only be achieved with computationally intensive numerical simulations or improved scaling theories that don't yet exist, and these are beyond the scope of this paper.

Nolan et al. fit their data assuming a slope of 1 for projectiles below 5.6 m in diameter and a least-squares fit to all points above this, yielding

$$\begin{aligned} D_{crat} &= C_s D_p^{\alpha_s} \qquad (D_p \leq D_{tr}) \\ D_{crat} &= C_f D_p^{\alpha_f} \qquad (D_p > D_{tr}) \end{aligned} \tag{7.1}$$

with $C_s = 35$ and $\alpha_s = 1$ in the strength regime and $C_f = 26.61$ and $\alpha_f = 1.159$ in the fracture regime (The C coefficients assume crater and projectile diameters in meters). The transition between these two regimes occurs at a transition projectile diameter of D_{tr}=5.6 m. For the largest, gravity-scaled craters,

$$D_{crat} = C_g D_p^{\alpha_g} \tag{7.2}$$

with $C_g = 161.4$ and $\alpha_g = 0.78$. The value of C_g used by Nolan et al. (1996) is for the diameter of the transient crater at the original surface level. The rim-to-rim diameter of the final crater would be about 50% larger than this (Melosh, 1989). Figure 7.1 shows the Nolan et al. (1996) hydrocode results, along with the fit to that data described above.

Using pi-group scaling theory (Holsapple and Schmidt, 1982) as presented in Melosh (1989), we can scale the Gaspra results of Nolan et al. (1996) to the other two S-type asteroids, Ida and Eros. With the following dimensionless parameters,

$$\begin{aligned} \pi_D &= D_{at}\left(\frac{\rho_t}{m_p}\right)^{1/3} && (7.3)\\ \pi_2 &= \frac{1.61 g D_p}{v_i^2} && (7.4)\\ \pi_3 &= \frac{Y}{\rho_p v_i^2}, && (7.5) \end{aligned}$$

where D_{at} is the diameter of the transient crater measured at the level of the original surface, ρ_p and ρ_t are the projectile and target densities, m_p is the mass of the projectile, g is the acceleration of gravity, Y is the target strength, v_i is the impact velocity, and D_p is the projectile diameter, the gravity-scaled crater diameter can be found from

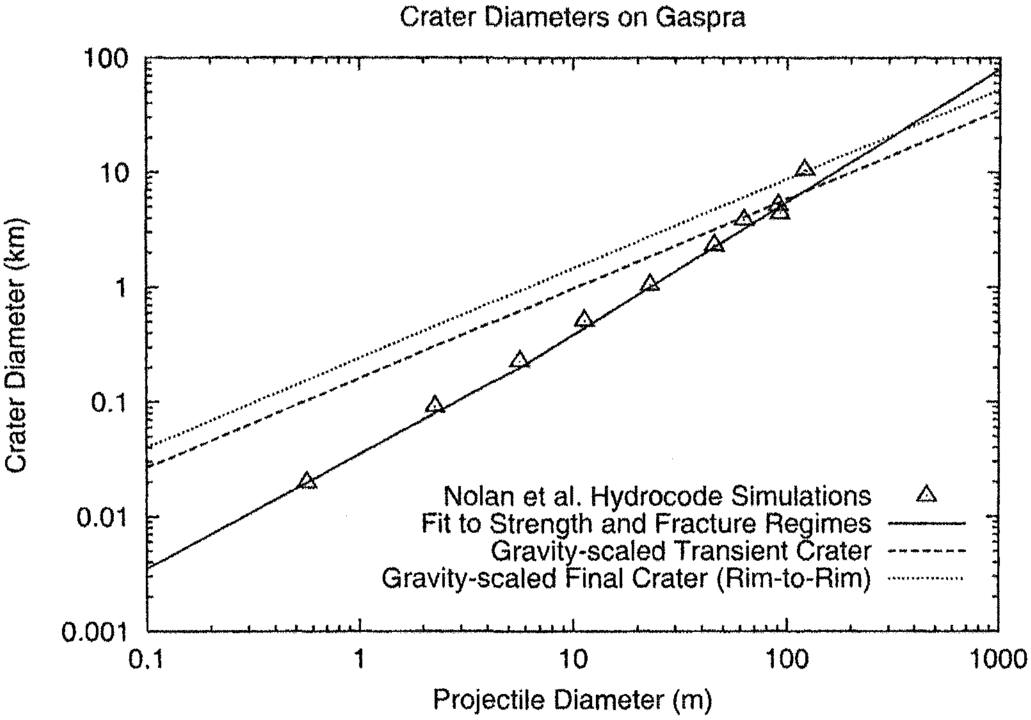

Figure 7.1: Crater diameter vs. projectile diameter for impacts into a Gaspra-sized spherical body at 5300 m/s, from hydrocode simulations by Nolan et al. (1996). The solid line is their least-squares fit to the data points for projectile diameters greater than 5.6 m and follows a slope of 1 for projectiles below 5.6 m, which form craters in the strength regime. The two dashed lines show the gravity-scaled crater diameter, which is an upper limit for the sizes of the largest craters.

$$\pi_D = C_D \pi_2^{-\beta}, \tag{7.6}$$

where β and C_D are constants (see Table 7.2), and the strength-scaled crater diameter can be found from

$$\pi_D = C'_D \pi_3^{-\sigma}, \tag{7.7}$$

where C'_D is a constant and

$$\sigma = \frac{\beta}{1-\beta}. \tag{7.8}$$

Melosh (1989) contains a misprinted version of Eq. 7.8 that is the negative of the correct value given here (Melosh, private communication). The fracture regime is not predicted explicitly by scaling theory, which considers only the effects of material strength and gravity, not the effect of pre-fracturing due to the passage of the shock wave through the target (Nolan et al., 1996).

In the strength regime, Eqns. 7.3, 7.5, and 7.7 imply that

$$D_{at} \propto \rho_t^{-1/3} v_i^{(2\beta/(1-\beta))}. \tag{7.9}$$

Nolan et al. (1996) find that the transition projectile diameter D_{tr} between strength-scaled and fracture-scaled craters is independent of the size of the target (for targets between a few km and a few hundred km in diameter) and always yields the same sized crater for fixed impact velocity and target/projectile densities. Assuming that the crater diameter at which the transition occurs is constant regardless of target density and impact velocity, we can scale the transition projectile diameter D_{tr} using Eqns. 7.3, 7.5, and 7.7:

$$D_{tr} \propto \rho_t^{1/3} v_i^{(-2\beta/(1-\beta))}. \tag{7.10}$$

To preserve continuity at D_{tr}, the fracture regime crater diameter scales as

$$D_{at} \propto \rho_t^{-(1+\alpha_f-\alpha_s)/3} v_i^{(2\beta/(1-\beta))(1+\alpha_f-\alpha_s)} \tag{7.11}$$

Equations 7.9, 7.10, 7.11, along with with the densities and impact velocities in Table 7.1 and Pi-scaling coefficients in Table 7.2, can be used to scale the Gaspra crater relationships for the strength and fracture regimes (Eq. 7.1) to Ida and Eros. Eqns. 7.3, 7.4, and 7.6 can be used to calculate the gravity-scaled transient crater diameter for a given asteroid and impact conditions

Pi-Group Scaling Constants

Material	C_D	β
Competent Rock	1.6	0.22
Loose Sand	1.54	0.165

Table 7.2: Pi-group scaling constants from Melosh (1989). The values for loose sand are an average of the values for Ottowa sand and quartz sand.

Mathilde, a C-type asteroid, is substantially different from the other asteroids (all S-types) observed by spacecraft. Mathilde is about half the density of the S-type asteroids (Table 7.1), implying a substantial internal porosity. In addition, numerous large craters (comparable in size to Mathilde's radius) are well preserved on Mathilde's surface, and their formation seems to have resulted in little damage beyond the crater rims (Chapman et al., 1999). Large craters on the S-type asteroids are not nearly as well preserved. This is taken as an additional indication of a porous internal structure for Mathilde—since porous materials are generally less efficient at transmitting shock waves, the damage from the impact would be confined to a smaller region, rather than causing global destruction of topography.

Because of these differences between Mathilde and the S-types, scaling from the Gaspra simulations to Mathilde is unjustified. Instead, we follow Davis (1999) and use the Pi-group gravity scaling relationship for loose sand (Eqns. 7.3, 7.4, and 7.6, and the values in Tables 7.1 and 7.2). A better estimate than this would require hydrocode simulations that are beyond the scope of this work.

Figure 7.2 shows the crater diameter vs. projectile diameter relationship for Gaspra, Ida, Mathilde, and Eros, calculated from the scaling relationships outlined above. The relationship for Gaspra and Eros are nearly identical, given their similar size and average impact velocity. The relationship for Ida is shifted downwards from these due to its larger size and smaller average impact velocity. Mathilde's curve is substantially different from the curves for the other asteroids.

7.3 Crater Erasure Mechanisms

Craters can be erased by a number of different methods (Greenberg et al., 1994; Greenberg et al., 1996).

7.3.1 Jolt

When a large impact occurs, it can cause global shaking of the asteroid that leads to the erasure of all craters smaller than a given diameter across its surface. This effect was termed 'global jolt' by Greenberg et al. (1994, 1996). Greenberg et al. (1996) give the size of a crater erased by craters of a given diameter due to global jolting on Ida and Gaspra (the Gaspra relationship is a slightly revised version of the one in Greenberg et al. (1994)). Eros is only about 40% larger than Gaspra, and therefore should have a roughly similar jolt relationship. We estimate the jolt relationship for Eros from the Gaspra and Ida jolt relationships by assuming that the jolt relationship varies linearly (in log-space) with the log of the radius of the

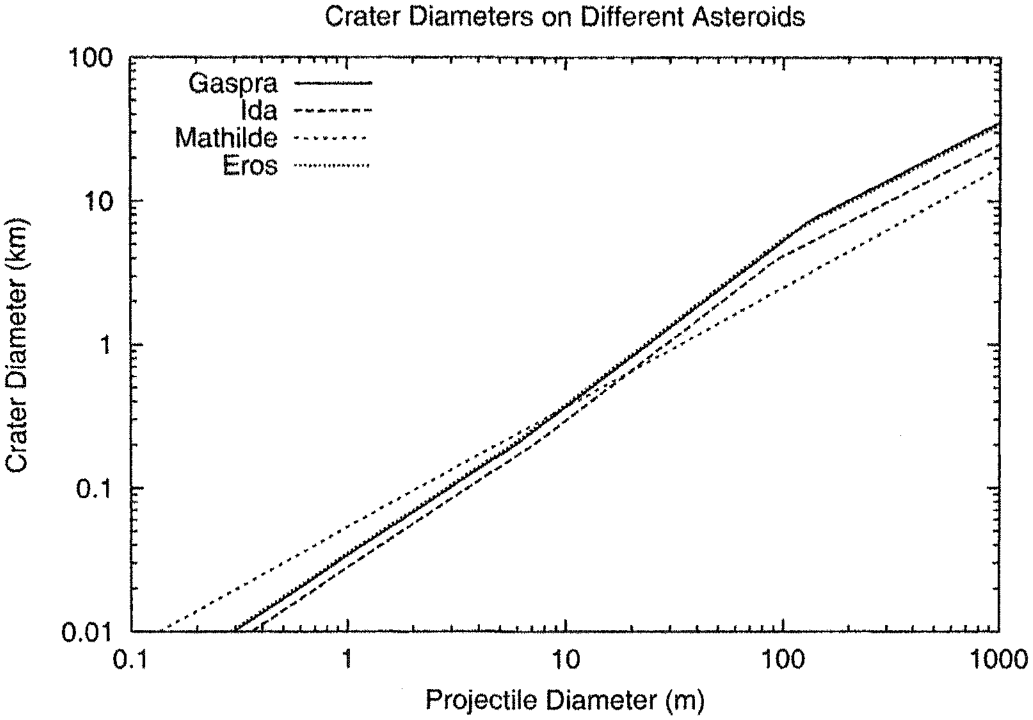

Figure 7.2: Crater diameter vs. projectile diameter curves for impacts on Gaspra, Ida, Mathilde, and Eros. Ida and Eros curves are scaled from the Gaspra simulations shown in Fig. 7.1, as described in the text. The Gaspra and Eros curves nearly overlap. For Mathilde, gravity scaling is assumed for all impacts.

target body. Figure 7.3 shows the size of a crater erased by craters of a given diameter due to global jolting on Gaspra and Ida (from Greenberg et al. (1996)) and our estimate of the Eros jolt relationship. Given the fact that even its largest craters do not significantly destroy topography beyond their rims, we assume that jolt is ineffective on Mathilde.

7.3.2 Overlap of Craters

As more and more craters accumulate on a given surface, a steady state is eventually reached between crater production and erasure due to craters forming on top of one another, such that the size distribution of craters no longer changes (Melosh, 1989). Greenberg et al. (1994, 1996) coined the terms 'sandblasting' for the erasure of large craters by smaller ones and 'cookie-cutter' for the erasure of small craters by larger ones. In either case, we can calculate the number of craters of a given size. If $R(D)$ is the number of craters of a given diameter D produced per unit area per unit time and A is the area taken up by all craters in a given size range per unit area per unit time, we can calculate the number of craters visible after time t by using an analogy to optical depth. Counting back in time from the present ($t = 0$), the incremental number of visible craters is

$$\mathrm{d}N_{vis}(D) = R(D)e^{-At}\mathrm{d}t \tag{7.12}$$

where the optical depth $\tau = At$ is zero at $t = 0$ and increases as more and more craters are formed. Consequently, the freshest craters are all visible, but going back in time, fewer and fewer old craters are visible because they are covered by newer ones. The total number of visible craters can be found by integrating from the present $t = 0$ to the time t when craters of diameter D first began accumulating:

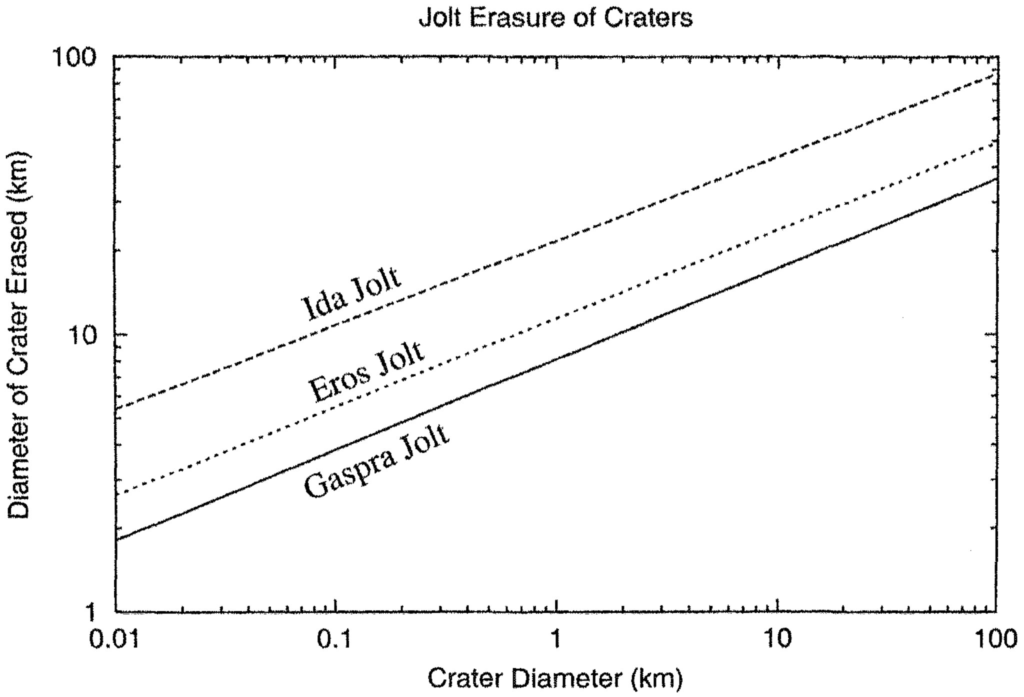

Figure 7.3: Plot showing the diameter of a crater erased by craters of a given diameter due to global jolting.

$$
\begin{aligned}
N_{vis}(D,t) &= \int_0^t R(D)e^{-At'}\mathrm{d}t' \\
&= \frac{R(D)}{A}\left(1-e^{-At}\right)
\end{aligned}
\tag{7.13}
$$

In the case of sandblasting we calculate A_{sb}, the total area taken up by craters smaller than D but larger than some fraction $\sim 1/10$ of D per unit area per unit time. This area is then divided by a factor of ~ 3 to account for the fact that smaller craters are less efficient at erasing larger ones. In the case of cookie-cutter erasure we calculate A_{cc}, the total area taken up by craters larger than D per unit area per unit time. We then combine these two values to give $A = A_{sb} + A_{cc}$, which we use in Eq. 7.13 to give the number of craters of a given diameter remaining after sandblasting and cookie-cutter erasure.

7.3.3 Local Jolt

When a large crater is formed, it may cause seismic effects that extend beyond its rim and can erase craters within a given fraction of its radius. Another way to look at this is that a crater's effective radius when used to calculate A_{cc}, the accumulated crater area per unit area per unit time for cookie-cutter erasure, is larger than its physical radius. Based on the hydrocode modeling of Nolan et al. (1996) and models of the evolution of cratering records on Gaspra and Ida, Greenberg et al. (1994, 1996) find that local jolt probably starts to be effective for craters larger than about 5 km in diameter such that craters ~ 30 km in diameter could have an effective diameter, due to local jolt, of several times their actual diameter.

7.4 Results

We have developed a numerical simulation based on the simulation used by Greenberg et al. (1994, 1996) that we have modified to handle arbitrary (i.e. non-power-law) impacting populations. Crater production is calculated from the impacting population and the crater production curves in Fig. 7.2, and the erasure mechanisms from Sec. 7.3 are all taken into account.

Figure 7.4 shows the results of our simulation using our best-fit main-belt population from Fig. 6.5 as the impacting population. Gaspra's cratering record is reproduced after 140 Myr of exposure following a resetting event that erased all craters larger than ~ 3 km, similar the model proposed by Greenberg et al. (1994). Ida requires either 4.5 Gyr of exposure to the impacting population and a strong local jolt effect (30 km craters are capable of erasing nearly the entire surface), or 500 Myr of exposure with a smaller local jolt effect. The former case is shown in Figure 7.4, but both cases give nearly the same final crater population. Eros requires 300 Myr of exposure and a mild local jolt effect (a 20 km crater can erase out to ~ 2 times its diameter). Finally, Mathilde requires 4.5 Gyr of exposure. The main discrepancies between our model and the observations are that the depletion of Eros's small craters is not explained, and the largest craters on Mathilde are not fully reproduced. We will address these issues in the conclusion.

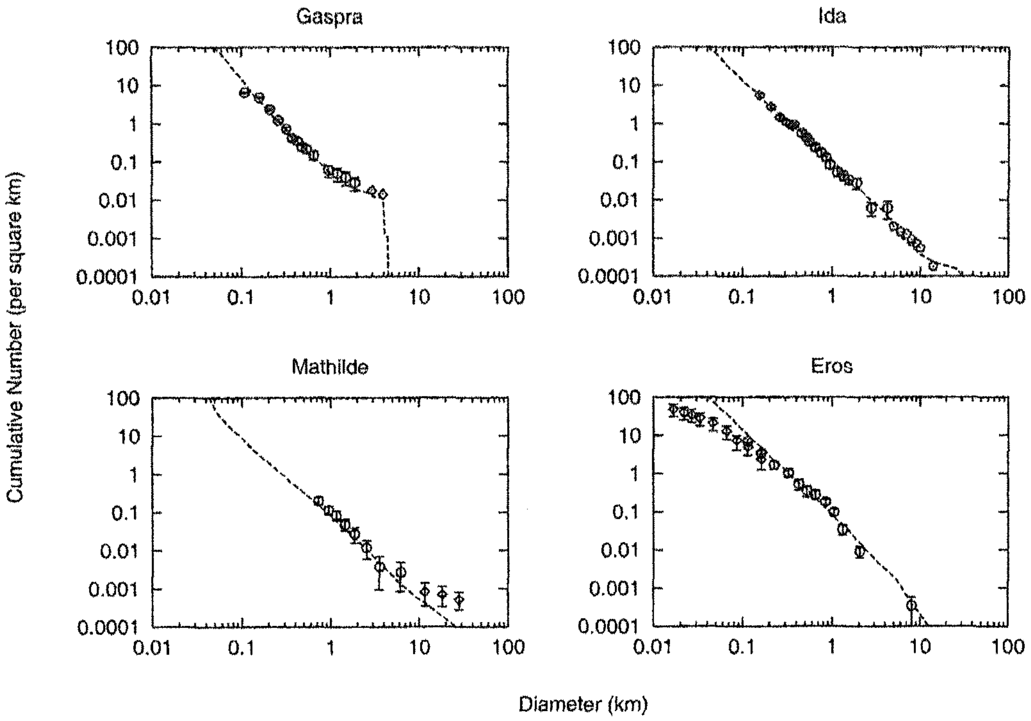

Figure 7.4: Plots showing the cratering records on the four observed asteroids along with the results of our cratering simulation with the main-belt population from Fig. 6.5 as the impacting population. The specific histories of these asteroids are described in the text.

CHAPTER 8

Collisional Evolution of Trans-Neptunian Objects

In this chapter, we apply the analytical and numerical tools that we have developed in Chapters 3 and 6 to the collisional evolution of trans-Neptunian objects.

8.1 Introduction

Edgeworth (1949) and Kuiper (1951) proposed that there may be a disk of icy material beyond the orbit of Neptune, somewhat analogous to the asteroid belt, consisting of material left over from the formation of the solar system that was unable to accrete into a larger planet. Pluto was discovered beyond the orbit of Neptune in 1930 by Clyde Tombaugh at Lowell Observatory, but at the time it was believed to be the 'Planet X' that Percival Lowell proposed as the cause of irregularities in Neptune's orbit. Despite later findings that Pluto was too small to have caused these perturbations, it was generally considered to be a full-fledged planet.

Over 60 years elapsed between Pluto's discovery and the discovery of the next trans-Neptunian object (TNO), 1992 QB_1 (Jewitt and Luu, 1993). In the 10 or so years since the discovery of 1992 QB_1, hundreds of other trans-Neptunian objects have been discovered and cataloged, and recent deep-field surveys have pushed our understanding of the orbital- and size-distribution of trans-Neptunian objects to smaller and smaller sizes. Through analytical theory and extensive numerical simulations, researchers are now beginning to understand the complex dynamical history that the trans-Neptunian region has experienced. In addition to dynamical evolution, it has been shown that, as in the asteroid belt, collisions are an important process governing the evolution of the TNO population.

Much as the main asteroid belt is the ultimate source of most NEAs, the trans-Neptunian region is the the source of most, if not all, short-period comets. Even before the discovery of 1992 QB_1, numerous researchers (e.g. Fernandez (1980), Duncan et al. (1988), Quinn et al. (1990)) demonstrated that the orbital distribution of short-period comets was consistent with a low-inclination disk of material beyond the orbit of Neptune. Subsequently, several authors (Holman and Wisdom, 1993; Levison and Duncan, 1997; Duncan and Levison, 1997; Morbidelli, 1997) performed more detailed simulations that give estimates of the number of precursor bodies that must exist in the trans-Neptunian region in order to explain the observed number of Jupiter-family comets (JFCs), which are a large subclass of short-period comets.

Bernstein et al. (2003)[1] used the Hubble Space Telescope to perform a deep-field search for TNOs down to nearly 29th magnitude (R-band), corresponding to a diameter of about 10 km at a heliocentric distance of 40 AU. They find that the 2 subsets of TNOs in their classification scheme, the 'classical' and 'excited' populations, have different size distributions. Assuming that JFCs have diameters of $\sim$10 km, citing earlier estimates such as Cochran et al. (1995), they find that there are far fewer JFC precursors than seem to be required by dynamical models. Bernstein et al. propose several possible explanations for this discrepancy: The survey results are an extremely unlikely statistical fluctuation or the survey completeness limit has been incorrectly estimated; The dynamical models are incomplete and/or underestimate the escape rate from the TNO region; Large TNOs break up into many smaller ones en-route to becoming JFCs; JFCs are fainter/smaller than generally believed; And/or there is an upturn in the population index below the completeness limit of the survey.

---

[1] The reference used here is a preprint posted to Astro-PH. The final published version was not in press at the time this dissertation was written, but has been accepted for publication in *AJ*

In this chapter, we apply our analytical and numerical collisional evolution models from Chapters 3 and 6 to constrain the evolutionary history of the TNOs. We explore in detail the suggestion by Bernstein et al. that there is an upturn in the population below the completeness limit of their survey. Using the numerical model described in Chapter 6, we show that such an upturn is a natural consequence of any physically plausible strength law, and can help to rectify the discrepancy between the Bernstein et al. survey results and dynamical models of the supply of JFCs.

8.2 The Structure and Dynamical History of the TNO Region

Observations and numerical simulations have identified a number of different subpopulations in the trans-Neptunian region. The Kuiper belt is a population of low-eccentricity bodies ranging in semimajor axis a from ~ 40 to ~ 48 AU, bound by the 3:2 and 2:1 mean-motion resonances with Neptune. Brown (2001) shows that the Kuiper Belt can be subdivided into a 'cold' population with inclinations $i \leq 4^o$ and a 'hot' population with inclinations as large as 30°. The cold Kuiper belt is most similar to what was envisioned by Edgeworth (1949) and Kuiper (1951), and is often termed the 'classical' Kuiper Belt. A number of TNO's are trapped in resonances with Neptune, such as the 3:2 mean-motion resonance at $a = 39.5$ AU ('Plutinos') and the 2:1 resonance at $a = 47.8$ AU ('twotinos'). These resonant populations generally have higher eccentricities and inclinations than the 'classical' Kuiper Belt. Finally, the 'scattered disk' population consists of objects on highly eccentric orbits beyond the orbit of Neptune, but no firm definition exists (Duncan and Levison, 1997). Observational evidence seems to point to an 'edge' to the classical Kuiper Belt around $a = 50$ AU, just outside of the 2:1 resonance with Neptune (Trujillo and Brown, 2001; Allen et al., 2001). Gladman et al. (2001), however, argues that this conclusion may be due to observational biases and a lack of sufficient orbital data.

The different sub-populations of TNOs were likely emplaced in different ways. Malhotra (1995) showed that gravitational interactions with planetesimal early in the history of the solar System could have caused Neptune to migrate outwards, trapping bodies in mean-motion resonances such as the 3:2 and 2:1. As those resonances would be moving outwards as Neptune migrates, bodies trapped in the resonances would be swept outwards as well, forming the 'resonant' populations. Duncan and Levison (1997) showed that during its migration, Neptune would gravitationally scatter some bodies onto highly eccentric and inclined orbits, thus forming the scattered disk population. Gomes (2003) showed that a subset of Neptune-scattered planetesimals could experience resonant effects that reduce their eccentricity and leave them in the Kuiper belt region, albeit with fairly large inclinations, as the hot Kuiper belt population.

Levison and Morbidelli (2003), noting that the cold Kuiper belt is significantly depleted in mass relative to the mass necessary to form 1000 km-scale objects (Stern and Colwell, 1997; Kenyon and Luu, 1998), showed that resonant effects combined with the migration of Neptune could cause planetesimals to migrate outwards under the action of the 2:1 resonance without increasing their inclinations. In addition, the eccentricities of these bodies would not monotonically increase, but would oscillate, giving a range of eccentricities comparable to that seen in the cold Kuiper belt. Since the migration of Neptune is not assumed to be perfectly uniform, there will be jumps in the position of the 2:1 resonance that cause some of the bodies trapped in resonance to be freed, and those bodies that escape form the cold Kuiper belt. A large number of bodies would be lost in this process due to inefficient resonance capture, the probability of being released from resonance, and scattering by Neptune, explaining the observed mass depletion of the cold Kuiper Belt relative to the primordial population. In addition, the Levison and Morbidelli (2003) model provides an explanation for why the classical Kuiper belt may end at the 2:1 resonance with Neptune.

An interesting and important implication of all of these models is that all TNOs—resonant TNOs, the scattered disk, and the hot and cold Kuiper belt—formed well inside their current positions and were pushed outwards by interactions with Neptune. In addition, there was potentially much more mass in the initial TNO population than there is in the current population. This has important implications for modeling the collisional history of TNOs. It is possible that a substantial amount, or even the majority, of the collisional evolution of some of the TNO sub-populations occurred very early on in the history of the solar system and in a different region than those populations currently reside. The timescale for the migration of Neptune, and hence the processes descried above, is on the order of 50-100 Myr (Levison and Morbidelli, 2003; Gomes, 2003).

8.3 The Link Between TNOs and the Jupiter-Family Comets

Jupiter-family comets (JFCs) are defined as those having a Tisserand parameter

$$T = \frac{a_J}{a} + 2\sqrt{(1-e^2)\frac{a}{a_J}}\ \cos(i) \tag{8.1}$$

between 2 and 3 (Levison and Duncan, 1997). These comets can experience low-velocity encounters with Jupiter, and hence their orbital evolution is generally dominated by Jupiter. Numerous authors (e.g. Fernandez (1980), Duncan et al. (1988), Quinn et al. (1990)) demonstrated that a disk of material beyond Neptune is the likely source of JFCs. In more detailed simulations, a number of authors calculated the number of JFC precursors necessary to sustain the observed population of JFCs, assuming different source regions.

Holman and Wisdom (1993), assuming a cold Kuiper belt as the source of JFCs, calculated 4.5×10^9 JFC precursors. Levison and Duncan (1997) refined this value to 7×10^9 JFC precursors in the cold Kuiper belt. Modeling the scattered disk population as the source of JFCs, Duncan and Levison (1997) calculated that there are 6×10^8 JFC precursors in the scattered disk, with 1.4×10^8 of them found at any given time between heliocentric distances of 30-50 AU. Finally, Morbidelli (1997) calculated that if the Plutino population is the source of JFCs, it should contain 4.5×10^8 JFC precursors.

8.4 The Size-Distribution of the TNO Population

Bernstein et al. (2003), using the Hubble Space Telescope Advanced Camera for Surveys (ACS), performed a survey for TNOs over a 0.02 deg^2 region of the sky with a limiting R-band magnitude of 28.8, which is 2 magnitudes deeper than the next closest survey and 3 or more magnitudes better than any others. It represents the current best estimate of the TNO population at small sizes.

The Bernstein et al. (2003) survey did not yield orbital elements, only heliocentric distance. They define TNOs as all bodies found at a heliocentric distance d larger than 25 AU. 'Classical' Kuiper Belt objects are TNOs found at heliocentric distances between 38 and 55 AU and $i \leq 5^o$, and 'excited' TNOs are all other TNOs. While there is a chance that resonant or scattered disk objects could be detected at a heliocentric distance that would classify it as 'classical' under the Bernstein et al. (2003) criteria, this is relatively unlikely. Hence, the 'classical' population from their survey is a good estimate of the cold Kuiper Belt, while the 'excited' sample is a good estimate of the hot Kuiper belt, resonant and scattered disk populations. As no TNOs were found beyond 50 AU in the Bernstein et al. (2003) survey, primarily due to difficulty of detecting small objects at large heliocentric distances, their results are primarily an estimate of the population in the 30-50 AU region. While many scattered disk objects do reside in this region at any given time and all have their perihelia within this region, the heliocentric radii of scattered disk objects can extend hundreds of AU from the sun, and the Bernstein et al. survey is not a good estimate of the population of scattered disk objects that are currently far from their perihelia.

Figure 8.1 shows the Bernstein et al. estimate of the total TNO population between 30 and 50 AU, along with their best-fit 2-segment power law. Figure 8.2 shows the classical and excited subsets of the TNO population from Bernstein et al., along with their best-fit 2-segment power laws. Note that the slope of the best-fit line for small excited objects is negative, indicating a deficit of small excited TNOs, or at the very least a local minimum.

The size distribution of TNOs can be estimated from the R magnitude data assuming that an R-magnitude of 28.5 corresponds to $D \sim 10$ km for an albedo of 4% and a heliocentric distance of 40 AU (Bernstein et al., 2003). As their values are given in number per square degree of sky, the absolute number can be estimated by multiplying the classical population (with inclinations between -5° and $+5^o$) by $360 \times 10 = 3600$ square degrees and the excited population by $360 \times 30 = 10800$ square degrees (Bernstein et al., 2003).

Bernstein et al. (2003) assume that JFC precursors are on the order of 10 km in diameter, citing earlier estimates such as Cochran et al. (1995). Compared to the estimates of the number of JFC precursors in the TNO population discussed in Sec. 8.3, the Bernstein et al. survey estimates 2-4 orders of magnitude too few JFC precursors.

8.5 Application of Analytical Model

The analytical model developed in Chapter 3 can be used to relate the log-log slope s of the strength law Q_D^* (the energy per unit mass required to fragment and disperse a body) to the steady-state power-law index p of the size distribution of a population

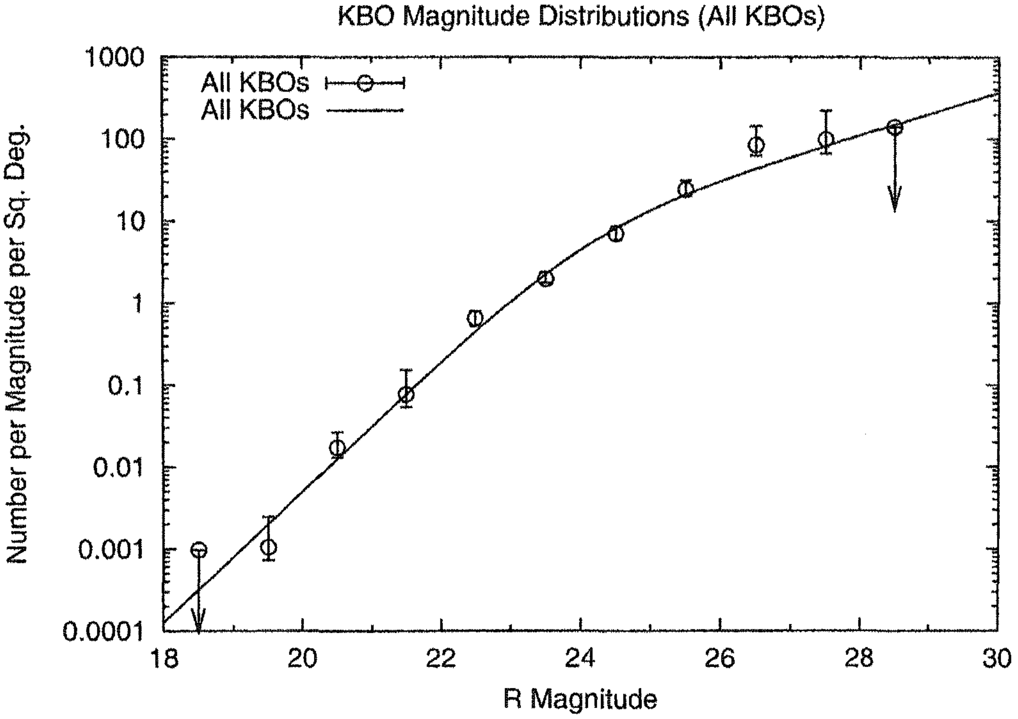

Figure 8.1: Plot of the R-magnitude distribution of the entire TNO population as determined by Bernstein et al. (2003). This population includes all bodies found at heliocentric radii greater than 25 AU. Size decreases with increasing R-magnitude. Symbols with arrows indicate upper limits.

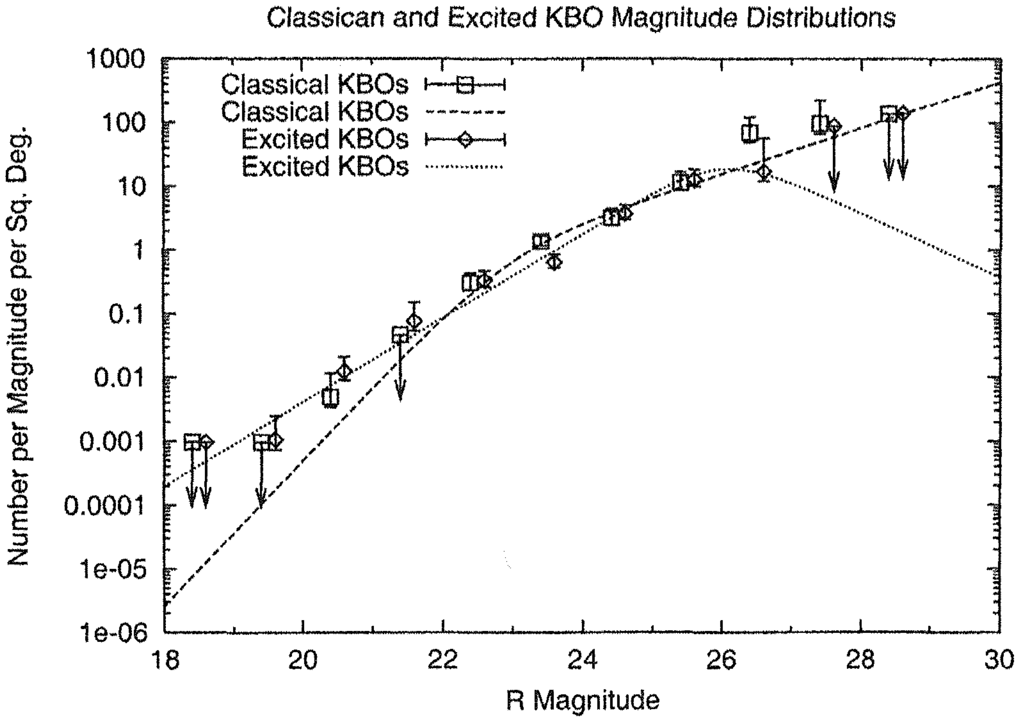

Figure 8.2: Plot of the R-magnitude distribution of the 'classical' and 'excited' TN populations as determined by Bernstein et al. (2003). The 'classical' population is the subset of TNOs found at heliocentric radii between 38 and 55 AU and $i \leq 5°$. The 'excited' population consists of all TNOs that are not in the 'classical' population. Size decreases with increasing R-magnitude. Symbols with arrows indicate upper limits.

of colliding bodies. The population of TNOs larger than $\sim$ 100 km in diameter is likely primordial and not collisionally relaxed (Davis and Farinella, 1997), and thus our analytical model cannot be applied to that portion of the population. The best-fit power laws to the magnitude distributions in Bernstein et al. (2003) have slopes α of 0.26 ($p = 2.3$) for all TNOs between $\sim$ 10 and 100 km in diameter and 0.36 ($p = 2.8$) for the classical population between $\sim$ 10 and 100 km in diameter (see Appendix A for the relation between the magnitude distribution and the size distribution). The excited population was found by Bernstein et al. (2003) to have a negative α (i.e. fewer small bodies than large ones) for bodies $\lesssim$ 50 km in diameter, indicating that it is most likely not in a collisional steady state and thus our analytical model can not be applied to it.

Using Eq. 3.24 to convert the values of p given in the previous paragraph to the slope s of the strength law Q_D^* gives $s = 2.3$ for the classical population and $s = 5.5$ for all TNOs. Both values are significantly larger than estimates of the gravity-regime Q_D^* for icy bodies (Benz and Asphaug, 1999), which indicate $s \approx 1.2 - 1.3$. We can use Eq. 3.24 to calculate the expected steady-state p given $s \approx 1.2 - 1.3$, and that calculation yields $p \approx 3.05 - 3.08$ between $\sim$ 10 and 100 km in diameter in the full TNO population as well as the classical subset.

The fact that the analytical theory does not give reasonable strength estimates from the observed values of p, and likewise does not give values of p consistent with observation when used with a reasonable strength law (Benz and Asphaug, 1999), likely indicates that the population of TNOs between $\sim$ 10 and 100 km in diameter is not in a collisional steady state. Furthermore, the fact that p predicted from the analytical theory using reasonable strength estimates is larger than the observed values of p may indicate that the initial population of TNOs was initially very shallow below $\sim$ 100 km in diameter and is currently evolving upwards (i.e. increasing in steepness) towards a steady state.

8.6 Numerical Simulations

In this section, we apply the numerical collisional evolution model developed in Chapter 6 to the evolution of the TNO population, in order to estimate the size-distribution below the limit of the Bernstein et al. (2003) survey. From this, we can determine whether or not the required number of JFC precursors can be found in the TNO population, and at what size they occur. In addition, we can use our simulations to constrain the initial conditions for the TNO population, such as the initial size distribution, as well as the degree of collisional evolution that that has occured in the TNO population over the age of the solar system.

Davis and Farinella (1997) (their Table I) calculated mean collision velocities $\langle V \rangle$ and intrinsic collision probabilities P_i for bodies in the TNO region with a range of different a, e, and i. From their values for low inclination, low eccentricity bodies around 42-45 AU, we estimate P_i and $\langle V \rangle$ for the classical population. Extrapolating beyond their range of e and i by about a factor of two, we estimate the values of P_i and $\langle V \rangle$ for the excited population. Our estimated values are given in Table 8.1. The collision velocities for the excited population are higher, due to its larger average e and i, but because of these larger e and i values, it occupies a larger volume of space and therefore has a smaller intrinsic collision probability. For the strength law, we choose Q_S and f_{KE} that yield the Benz and Asphaug (1999) Q_D^* for impacts between icy bodies at 500 m/s, as shown in Fig. 8.3.

TNO Collision Velocities and Probabilities

Population	P_i (km^{-2} yr^{-1})	$\langle V \rangle$ (m/s)
Classical	2×10^{-21}	400
Excited	4×10^{-22}	1200

Table 8.1: Mean collision velocity and intrinsic collision probability for classical and excited TNOs between 30 and 50 AU, based on values from Davis and Farinella (1997)

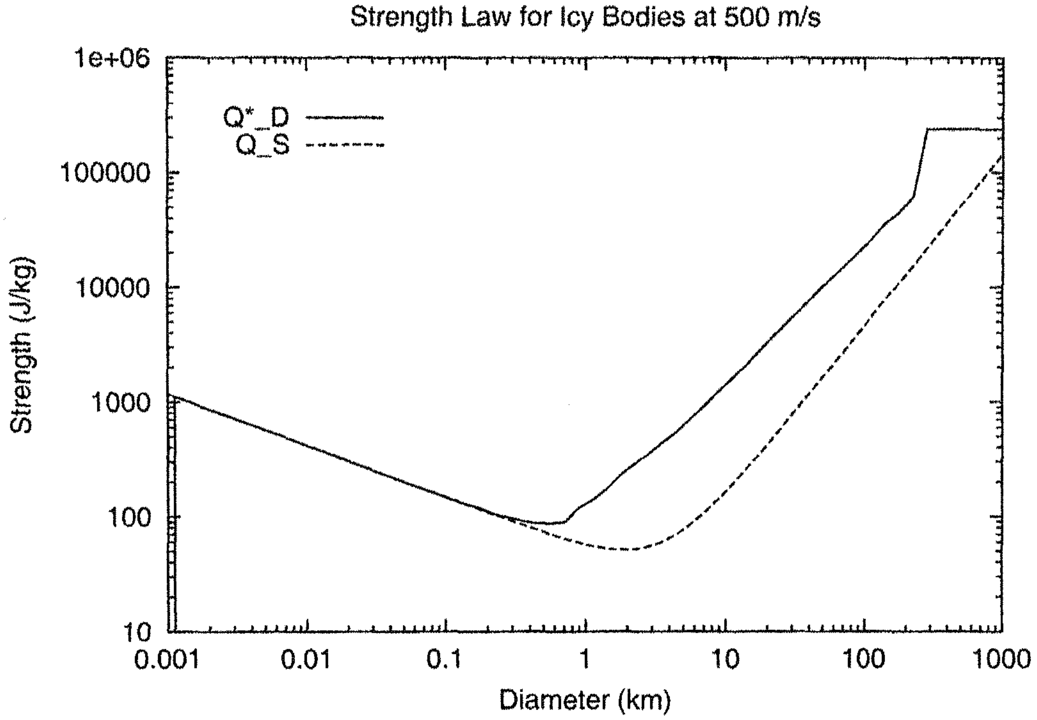

Figure 8.3: Strength of icy bodies. The Q_S law and f_{KE} are chosen to yield Q_D^* for icy bodies at 500 m/s from Benz and Asphaug (1999). The 'jump' in Q_D^* at the largest sizes is not real—it is an artifact of how our code calculates Q_D^* when the size of the projectile necessary to disrupt a given target is larger than the target itself.

We use two different sets of initial populations: (1) shallow initial populations based on the Bernstein et al. (2003) double-power-law fits to the classical and excited populations; or (2) steep initial populations based on the Bernstein et al. (2003) fits for large bodies and a $p = 3.5$ differential power law for smaller bodies. While the classical and excited populations are likely to interact to some degree, we treat them separately here for simplicity. The classical and excited populations are evolved with both steep and shallow initial populations for 3 cases: (1) 4.5 Gyr, (2) 4.5 Gyr with primordial evolution phase at 1000 times the current mass for 100 Myr, and (3) same as case 2 but assuming a broken power-law fragment distribution with $r_b = 0.5$ and $r_m = 0.01$ (see Section 6.1 for a discussion of these parameters). The primordial evolution phase is roughly consistent with estimates of the timescale for the dynamical evolution of the TNO region in the early solar system and the mass depletion during that phase (Levison and Morbidelli, 2003; Gomes, 2003). Figures 8.4-8.7 show the results of our simulations.

It is immediately evident that for the cases with a steep initial population (Figs. 8.4 and 8.5) very little collisional erosion of the population occurs in any of the cases. As Bernstein et al. (2003) detect a roll-over in the population towards small sizes, it seems that either the strength law we are using is very far off, or that it is unlikely that the initial population of either the classical or excited population was steep.

For the cases where the initial population is shallow (Figs. 8.4 and 8.5), an upturn in the population at small sizes (below the Bernstein et al. (2003) detection limit) forms during the 4.5 Gyr of evolution. The upturn occurs at larger sizes when primordial evolution is taken into account (Case 2) and somewhat larger still when a broken power-law fragment distribution is used. Such an upturn could help explain the discrepancy between the Bernstein et al. (2003) estimates of the number of JFC precursors and the number required by dynamical models.

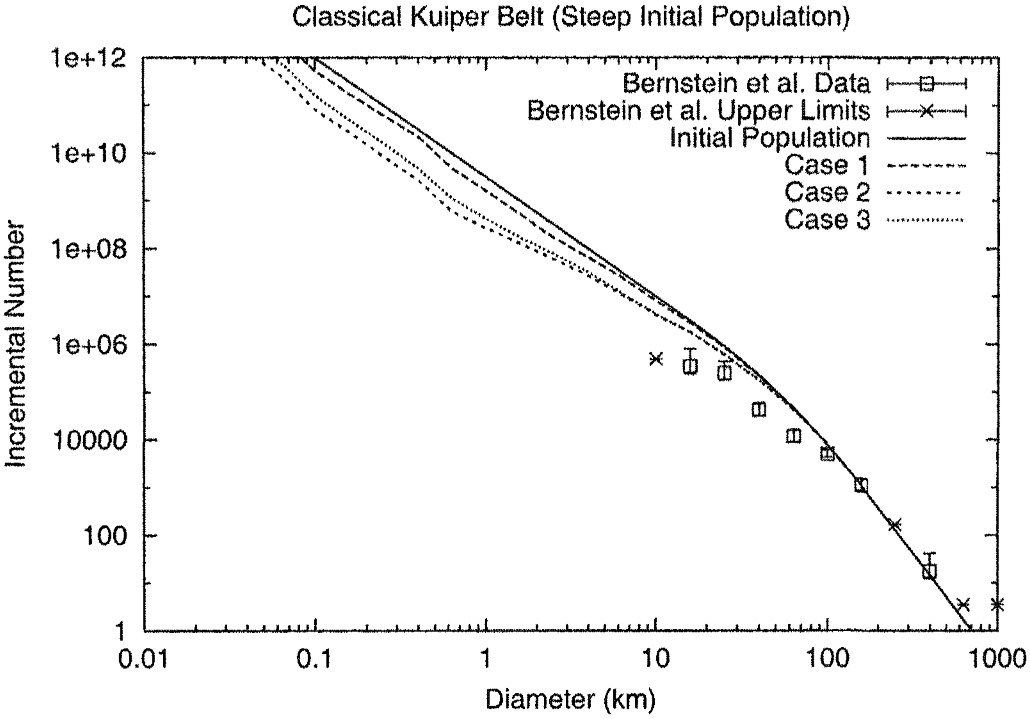

Figure 8.4: Collisional evolution of the classical kuiper belt starting from a steep initial population. (1) 4.5 Gyr, (2) 4.5 Gyr with primordial evolution phase at 1000 times the current mass for 100 Myr, and (3) same as case 2 but assuming a broken power-law fragment distribution with $r_b = 0.5$ and $r_m = 0.01$.

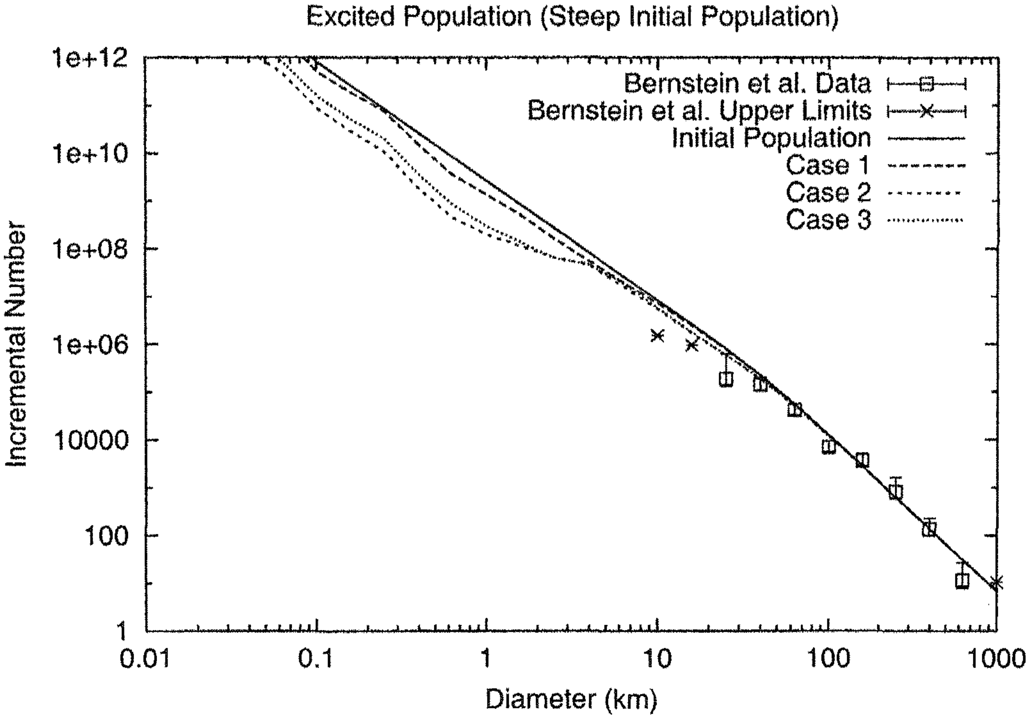

Figure 8.5: Same as Fig. 8.4 but for the excited population.

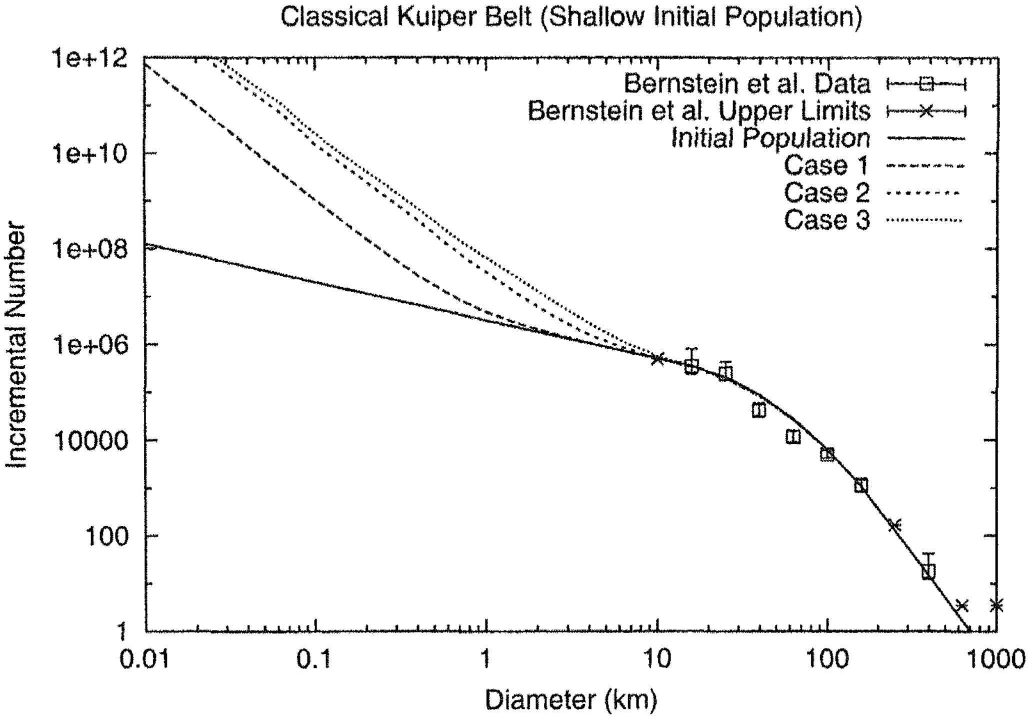

Figure 8.6: Same as Fig. 8.4 but for a shallow initial population.

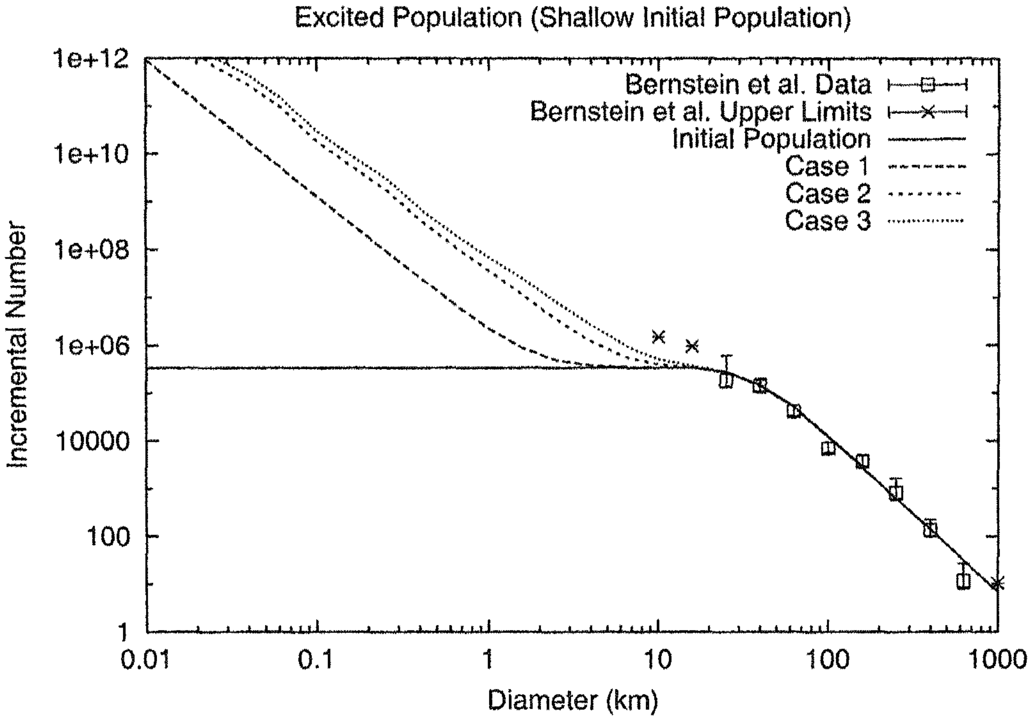

Figure 8.7: Same as Fig. 8.6 but for the excited population.

From excited population sources, Morbidelli (1997) estimates 4.5×10^8 JFC precursors in the Plutino population and Duncan and Levison (1997) estimates 1.4×10^8 in scattered disk between 30-50 AU. For classical sources, Levison and Duncan (1997) estimates 7×10^9 JFC precursors in the cold Kuiper belt. From Fig. 8.6, in the cases where primordial collisional evolution has been taken into account, this would imply that JFCs have diameters of $\sim$ 200 m or so if they come from the classical population. From Fig. 8.7, for the cases where primordial collisional evolution has been taken into account, this implies that JFCs have diameters of $\sim$ 500 m or so in diameter if they come from the excited population.

8.7 Conclusion

We have shown, through numerical collisional evolution simulations, that for reasonable parameter choices, a shallow initial population for the classical and excited TNO populations will experience an upturn at small sizes, increasing the number of possible JFC precursor bodies. Constraining our simulations with observational data from Bernstein et al. (2003) and comparing our results to dynamical models of JFCs, we find that JFCs are on the order of 500 m in diameter if they come from excited sources and about 200 m in diameter if they come from a classical source. Our results are only based on a single strength law, the Benz and Asphaug (1999) for ice, so it is quite possible that other strength laws would yield JFC sizes somewhat larger than our estimates, especially if TNOs are more like 'dirty snowballs' than solid icy bodies.

Bernstein et al. (2003), citing previous work (Cochran et al., 1995), estimate that JFCs are $\sim$ 10 km in diameter, but is this reasonable? Lamy et al., in a preprint version of their Comets II chapter, give sizes for the nuclei of dozens of JFCs, with many of them being a few km or less. With this estimate, and our simulations, it seems that there is much less of an inconsistency between the observationally determined TNO population and the population of JFCs than originally proposed by Bernstein et al. (2003).

Furthermore, our simulations indicate that starting with a steep initial population, there would be insufficient collisional erosion of the population over 4.5 Gyr to match observational estimates of the current TNO population. Both our analytical and numerical models indicate that the TNO population most likely began with a shallow initial population. This places a strong constraint on models of the formation and evolution of the TNO population.

CHAPTER 9

Summary and Discussion

The work presented in this dissertation encompasses both analytical and numerical modeling of the evolution of the major small-body populations in the solar system—the main-belt asteroids, the near-Earth asteroids (NEAs) and the trans-Neptunian objects (TNOs). We have made substantial contributions to the understanding of all of these populations of objects.

In Chapter 3 we develop an analytical model for the steady-state size distribution of a collisional population whose strength varies with size. Our analytical model is a significant improvement over previous models that all treated strength as a size-independent property, contrary to large amounts of experimental and theoretical evidence. Our model is able to reproduce the general features of the main-belt size distribution, such as the difference in average slope between the small and large bodies and the waves formed in the size distribution of the larger asteroids because of that transition in slope. Comparisons between our analytical model and a simple numerical model show that it is quite accurate, and allows for reasonable predictions in many cases that would otherwise require a numerical simulation.

In addition to collisions, dynamical processes, such as the sweeping of bodies into resonances by the Yarkovsky effect, are able to perturb the size distribution of main-belt asteroids and create the NEA population. In Chapter 4, we identify the results of numerical simulations by other authors, primarily those of Bottke et al. (2000, 2002), that help constrain the dynamical removal rate of bodies from the main belt and their lifetime as NEAs. In Chapter 5, we present a simplified mathematical description of the Yarkovsky effect and derive an approximate relation for the removal rate from the main belt, and hence the supply rate of NEAs, as a function of size.

In Chapter 6, we develop a self-consistent numerical simulation for modeling the simultaneous collisional and dynamical evolution of the main-belt and NEA size distributions due to collisional and dynamical effects. Our model is able to fit a wide range of observational and theoretical constraints. Our model can match the observed main-belt and NEA size-distributions, and as shown in Chapter 7 the main-belt population is able to mostly reproduce the observed cratering records on Gaspra, Ida, Mathilde, and Eros. The lifetimes of meter-sized bodies in the main belt are within a factor of 2 of the average CRE ages of stony meteorites. In addition, the number of large asteroid families we form (7) is consistent with the number observed (8), and the basaltic crust of Vesta is preserved. Subsequent to this work, no single model has been able to reconcile all six of these constraints. The strength and non-collisional removal rates we use are consistent with estimates by other authors, as well as our own estimate of the removal rate from Chapter 5.

An important result of our numerical simulations is that non-collisional removal is not strong enough to remove enough bodies to give the orders-of-magnitude depletion that has been invoked to explain the lack of small craters on Eros (Chapman et al., 2002) or the steepness of Gaspra's cratering record (Hartmann and Ryan, 1996). Collisional debris quickly replaces the bodies that are lost through resonances and the Yarkovsky effect, thus preventing a runaway depletion even for unreasonably large Yarkovsky-driven removal rates.

Several outstanding issues remain. We are not able to reproduce the depletion of small craters on Eros. A number of explanations for this depletion have been given, including Yarkovsky depletion of small impactors (Hartmann and Ryan, 1996; Chapman et al., 2002), which we can rule out, seismic effects (Chapman et al., 2002; Richardson et al., 2004), which are currently beyond the scope of our modeling, and the obscuration of small craters by boulders (Greenberg and O'Brien, 2003). We will address the latter two effects in more detail in future work. Our model also predicts about a factor of 2 fewer large craters on Mathilde than are actually seen. As a set of hydrocode runs for crater formation on a Mathilde-like body is unavailable, and there is no consensus on exactly how Mathilde reacts to impacts, we were forced to make simplifying assumptions based on scaling laws that may not be fully accurate in describing crater formation on Mathilde. Should a set of hydrocode results for Mathilde that is comparable to the Nolan et al. (1996) results for Gaspra become available, we will incorporate those results into our model of the evolution of Mathilde's crater population. Finally, the fact that using a 2-slope power law ($r_b < 1$) rather than a less realistic single-slope power law gives a worse fit in our simulations probably points to a limitation of our model, rather than indicating that asteroids break up following a single power-law.

With the increasing power of computers and the availability of fast N-body codes, it will soon be possible to construct a collisional outcome matrix based on numerical impact simulations rather than the semi-analytical algorithm we describe in Chapter 6. Such a model would likely be more realistic than our algorithm, as it can account for effects that our algorithm can not. For example, Michel et al. (2002, 2003) have shown that one of our primary assumptions—that fragments reaccumulate on a common center—is generally not the case. Instead, several smaller reaccumulated bodies often form, leading to a significantly different fragment size-distribution than what we assume in our simulations. Despite its limitations, however, the model we have developed is powerful and has allowed us to reconcile a wide range of observational and theoretical evidence that has thus far not been treated as a whole.

A natural application of the analytical and numerical tools that we have developed for studying asteroids is to model collisional evolution in the trans-Neptunian region. The TNOs, like the asteroid belt, are a population that evolves under the influence of mutual collisions. In Chapter 8, we apply the analytical model developed in Chapter 3 and the numerical model developed in Chapter 6 to the collisional evolution of trans-Neptunian objects. We show that the TNO population likely started with a shallow initial size distribution, and that the population $\gtrsim$ 10 km is probably not in a collisional steady state. In addition, we show that the population in the TNO region below the size range of recent observational surveys ($\lesssim$ 10 km in diameter) is likely large enough to explain the observed numbers of Jupiter-family comets.

APPENDIX A

Power-Law Representations of Size and Mass Distributions

A number of different power-law representations of asteroid size and mass distributions are used in this dissertation and in the general scientific literature. Here we derive the relationships between these different representations. Those relationships are summarized in Table A.1 at the end of this appendix.

The starting point is the 'differential' or 'incremental' size distribution

$$\mathrm{d}N = BD^{-p}\mathrm{d}D, \tag{A.1}$$

where D is the diameter, $\mathrm{d}N$ is the incremental number of bodies in the size range $[D, D + \mathrm{d}D]$, B is a constant, and p is the power-law index. On a log-log plot, Eq. A.1 would plot as a line with a slope of $-p$. If there are $N(> D_o)$ bodies larger than D_o in the population, B is found from

$$\begin{aligned}
\int_{D_o}^{\infty} BD^{-p}\mathrm{d}D &= N(> D_o) && \text{(A.2)}\\
\left[\frac{BD^{1-p}}{1-p}\right]_{D_o}^{\infty} &= N(> D_o) && \text{(A.3)}\\
B &= (p-1)D_o^{p-1}N(> D_o). && \text{(A.4)}
\end{aligned}$$

Note that p must be greater than 1 for the previous integration to yield a finite value. With the value of B from Eq. A.4, the normalized incremental distribution is

$$\mathrm{d}N = (p-1)D_o^{p-1}N(>D_o)D^{-p}\mathrm{d}D. \tag{A.5}$$

If instead of constant intervals $\mathrm{d}D$ the intervals are of a constant logarithmic size $\mathrm{d}\log D$, the relation

$$\frac{\mathrm{d}}{\mathrm{d}D}(\log D) = \frac{\mathrm{d}}{\mathrm{d}D}\left(\frac{\ln D}{\ln 10}\right) = \frac{1}{D\ln 10} \tag{A.6}$$

yields

$$\mathrm{d}D = D\ln 10\,\mathrm{d}\log D, \tag{A.7}$$

which can then be used to convert Eq. A.5 to the log-incremental form

$$\mathrm{d}N = \ln 10\,(p-1)D_o^{p-1}N(>D_o)D^{1-p}\,\mathrm{d}\log D. \tag{A.8}$$

Note that the exponent $1-p$ is 1 larger than the exponent p in the incremental distribution.

Eq. A.5 can be integrated to give the cumulative number distribution $N(>D)$

$$\begin{aligned} N(>D) &= \int_D^\infty (p-1)D_o^{p-1}N(>D_o)D^{-p}\mathrm{d}D && \text{(A.9)} \\ &= \left[\frac{(p-1)D_o^{p-1}N(>D_o)D^{1-p}}{1-p}\right]_D^\infty && \text{(A.10)} \\ &= N(>D_o)\left(\frac{D}{D_o}\right)^{1-p}. && \text{(A.11)} \end{aligned}$$

Note that the exponent $1-p$ is the same as for the log-incremental distribution, and is 1 larger than the exponent p in the incremental distribution.

Using the relation

$$\mathrm{d}M = \frac{\pi\rho D^3}{6}\mathrm{d}N, \tag{A.12}$$

the incremental number distribution Eq. A.5 can be converted to an incremental mass distribution

$$\mathrm{d}M = \frac{\pi\rho}{6}(p-1)D_o^{p-1}N(>D_o)D^{3-p}\,\mathrm{d}D. \tag{A.13}$$

In the case of logarithmic intervals $\mathrm{d}\log D$, Eq. A.7 can be used to convert Eq. A.13 to

$$\mathrm{d}M = \ln 10\,\frac{\pi\rho}{6}(p-1)D_o^{p-1}N(>D_o)D^{4-p}\mathrm{d}\log D. \tag{A.14}$$

The mass contained in bodies of diameter less than D is given by integrating Eq. A.13 to give

$$\begin{aligned} M(<D) &= \int_0^D \frac{\pi\rho}{6}(p-1)D_o^{p-1}N(>D_o)D^{3-p}\mathrm{d}D & \text{(A.15)}\\ &= \left[\frac{\pi\rho}{6(4-p)}(p-1)D_o^{p-1}N(>D_o)D^{4-p}\right]_0^D & \text{(A.16)}\\ &= \frac{\pi\rho}{6(4-p)}(p-1)D_o^{p-1}N(>D_o)D^{4-p}. & \text{(A.17)} \end{aligned}$$

A p greater than 4 will give infinite mass in the previous integration, which places an upper limit of $p = 4$ for the case of a single power law extending to zero size.

The incremental distribution in Eq. A.5 can be converted to a function of mass m rather than diameter using

$$\begin{aligned} m &= \frac{\rho\pi D^3}{6} && \text{(A.18)} \\ \frac{\mathrm{d}m}{\mathrm{d}D} &= \frac{\rho\pi D^2}{2}, && \text{(A.19)} \end{aligned}$$

where ρ is the density. The previous two equations can be solved for D and $\mathrm{d}D$ in terms of m and $\mathrm{d}m$ and inserted into Eq. A.5 to yield

$$\begin{aligned} \mathrm{d}N &= \frac{2}{\rho\pi}(p-1)D_o^{p-1}N(>D_o)D^{-p-2}\mathrm{d}m && \text{(A.20)} \\ &= \frac{2}{\rho\pi}\left(\frac{6}{\rho\pi}\right)^{\frac{-2-p}{3}}(p-1)D_o^{p-1}N(>D_o)m^{\frac{-p-2}{3}}\,\mathrm{d}m. && \text{(A.21)} \end{aligned}$$

The incremental number distribution as a function of mass (Eq. A.21) was used, with a different normalization factor, by Dohnanyi (1969) in his derivation of the collisional steady-state. Dohnanyi found a value of 11/6 for the exponent of the mass in Eq. A.21, which is equivalent to the more commonly quoted result that $p = 3.5$. In the case of logarithmic intervals $\mathrm{d}\log m$, the relation

$$\mathrm{d}m = m \ln 10\, \mathrm{d}\log m, \tag{A.22}$$

which is analogous to Eq. A.7, can be used to convert Eq. A.21 to

$$\mathrm{d}N = \ln 10\, \frac{2}{\rho\pi}\left(\frac{6}{\rho\pi}\right)^{\frac{-2-p}{3}}(p-1)D_o^{p-1}N(>D_o)m^{\frac{1-p}{3}}\,\mathrm{d}\log m. \tag{A.23}$$

The other distributions can be written as functions of mass as well. Equation A.11, the cumulative number of bodies larger than D, can be converted to the number of bodies with a mass larger than m using Eq. A.18

$$N(> m) = \frac{N(> D_o)}{D_o^{1-p}} \left(\frac{6}{\rho\pi}\right)^{\frac{1-p}{3}} m^{\frac{1-p}{3}}. \tag{A.24}$$

Equation A.21, the differential number distribution as a function of m, can be converted to the differential mass distribution by simply multiplying it by m to yield

$$\mathrm{d}M = \frac{2}{\rho\pi} \left(\frac{6}{\rho\pi}\right)^{\frac{-2-p}{3}} (p-1) D_o^{p-1} N(> D_o) m^{\frac{1-p}{3}} \,\mathrm{d}m. \tag{A.25}$$

In the case of logarithmic intervals $\mathrm{d}\log m$, Eq. A.22 can be used to convert Eq. A.25 to

$$\mathrm{d}M = \ln 10 \,\frac{2}{\rho\pi} \left(\frac{6}{\rho\pi}\right)^{\frac{-2-p}{3}} (p-1) D_o^{p-1} N(> D_o) m^{\frac{4-p}{3}} \,\mathrm{d}\log m. \tag{A.26}$$

Finally, Eqn. A.17, the cumulative mass in bodies smaller than D, can be converted to the cumulative mass of bodies with mass smaller than m using Eq. A.18

$$M(< m) = \left(\frac{6}{\rho\pi}\right)^{\frac{4-p}{3}} \frac{\pi\rho}{6(4-p)} (p-1) D_o^{p-1} N(> D_o) m^{\frac{4-p}{3}}. \tag{A.27}$$

The cumulative number and mass distributions as a function of mass (Eqns. A.24 and A.27) are used, with different normalization factors and modifications to allow for different large- and small-mass slopes, in the collisional algorithm outlined in Sec. 6.1.1.

If the absolute magnitude H is used instead of diameter D, the exponent of the magnitude distribution can be related to the differential power-law index p. The magnitude scale is logarithmic and a decrease of 5 magnitudes corresponds to an increase in brightness by a factor of 100, which, assuming a constant albedo, corresponds to an increase in projected area by a factor of 100 or an increase in diameter by a factor of 10:

$$D \propto 10^{-H/5}. \tag{A.28}$$

Taking the logarithm of Eq. A.28 and then differentiating it gives

$$\mathrm{d}\log D = -\frac{\mathrm{d}H}{5}. \tag{A.29}$$

If the H magnitude distribution is

$$\mathrm{d}N \propto 10^{\alpha H}\,\mathrm{d}H, \tag{A.30}$$

Eq. A.29 indicates that the factor α in the exponent of Eq. A.30 is related to the exponent $1 - p$ of the log-incremental distribution (Eq. A.8) by

$$-5\alpha = 1 - p, \tag{A.31}$$

which, with Eq. A.30, gives the relation

$$\mathrm{d}N \propto 10^{\frac{H(p-1)}{5}}\,\mathrm{d}H. \tag{A.32}$$

In the case of magnitudes that are not absolute, such as the R magnitude used for trans-Neptunian objects (TNOs) in Chapter 8, the magnitude cannot be directly related to size without knowing the heliocentric distance, Earth-object distance, and Earth-object-Sun angle. However, in the case of TNOs, if all bodies are assumed to be at the same average heliocentric distance, Earth-object distance, and Earth-object-Sun angle, the above relations can still be used to relate the magnitude distribution to the power-law index of the size distribution.

The different size and mass distributions are summarized in Table A.1, along with the values of their exponents assuming $p = 3.5$, the classical Dohnanyi result for self-similar collisional systems.

Power-Law Representations of Size and Mass Distributions

Distribution	Power-Law Expression	Exponent for $p = 3.5$
$\mathrm{d}N/\mathrm{d}D$	$\mathrm{d}N \propto D^{-p}\,\mathrm{d}D$	-3.5
$\mathrm{d}N/\mathrm{d}\log D$	$\mathrm{d}N \propto D^{1-p}\,\mathrm{d}\log D$	-2.5
$N(>D)$	$N(>D) \propto D^{1-p}$	-2.5
$\mathrm{d}M/\mathrm{d}D$	$\mathrm{d}M \propto D^{3-p}\,\mathrm{d}D$	-0.5
$\mathrm{d}M/\mathrm{d}\log D$	$\mathrm{d}M \propto D^{4-p}\,\mathrm{d}\log D$	0.5
$M(<D)$	$M(<D) \propto D^{4-p}$	0.5
$\mathrm{d}N/\mathrm{d}m$	$\mathrm{d}N \propto m^{(-p-2)/3}\,\mathrm{d}m$	-11/6
$\mathrm{d}N/\mathrm{d}\log m$	$\mathrm{d}N \propto m^{(1-p)/3}\,\mathrm{d}\log m$	-5/6
$N(>m)$	$N(>m) \propto m^{\frac{1-p}{3}}$	-5/6
$\mathrm{d}M/\mathrm{d}m$	$\mathrm{d}M \propto m^{(1-p)/3}\,\mathrm{d}m$	-5/6
$\mathrm{d}M/\mathrm{d}\log m$	$\mathrm{d}M \propto m^{(4-p)/3}\,\mathrm{d}\log m$	1/6
$M(<m)$	$M(<m) \propto m^{\frac{4-p}{3}}$	1/6
$\mathrm{d}N/\mathrm{d}H$	$\mathrm{d}N \propto 10^{\frac{H(p-1)}{5}}\,\mathrm{d}H$	0.5

Table A.1: Different power-law representations of size and mass distributions. The value of the exponent of each of the power-law functions is given for $p = 3.5$, the classical Dohnanyi equilibrium value. For the H magnitude distribution, the value of the coefficient of H in the exponent is given.

REFERENCES

Afonso, G. B., R. S. Gomes, and M. A. Florczak (1995). Asteroid fragments in Earth-crossing orbits. *Planet. Space Sci.* **43**, 787–795.

Allen, R. L., G. M. Bernstein, and R. Malhotra (2001). The Edge of the Solar System. *ApJ* **549**, L241–L244.

Bell, J. F., D. R. Davis, W. K. Hartmann, and M. J. Gaffey (1989). Asteroids - The big picture. In *Asteroids II*, pp. 921–945.

Belton, M., C. Chapman, P. Thomas, M. Davies, R. Greenberg, K. Klaasen, D. Byrnes, L. D'Amario, S. Synnott, W. Merline, J.-M. Petit, A. Storrs, and B. Zellner (1995). The bulk density of asteroid 243 Ida from Dactyl's orbit. *Nature* **374**, 785–788.

Belton, M. J. S., C. R. Chapman, J. Veverka, K. P. Klaasen, A. Harch, R. Greeley, R. Greenberg, J. W. Head, A. McEwen, D. Morrison, P. C. Thomas, M. E. Davies, M. H. Carr, G. Neukum, F. P. Fanale, D. R. Davis, C. Anger, P. J. Gierasch, A. P. Ingersoll, and C. B. Pilcher (1994). First Images of Asteroid 243 Ida. *Science* **265**, 1543–1547.

Belton, M. J. S., B. E. A. Mueller, L. A. D'Amario, D. V. Byrnes, K. P. Klaasen, S. Synnott, H. Breneman, T. V. Johnson, P. C. Thomas, J. Veverka, A. P. Harch, M. E. Davies, W. J. Merline, C. R. Chapman, D. Davis, T. Denk, G. Neukum, J. Petit, R. Greenberg, A. Storrs, and B. Zellner (1996). The Discovery and Orbit of 1993 (243)1 Dactyl. *Icarus* **120**, 185–199.

Belton, M. J. S., J. Veverka, P. Thomas, P. Helfenstein, D. Simonelli, C. Chapman, M. E. Davies, R. Greeley, R. Greenberg, and J. Head (1992). Galileo encounter with 951 Gaspra - First pictures of an asteroid. *Science* **257**, 1647–1652.

Benz, W. and E. Asphaug (1999). Catastrophic Disruptions Revisited. *Icarus* **142**, 5–20.

Bernstein, G. M., D. E. Trilling, R. L. Allen, M. E. Brown, M. J. Holman, and R. Malhotra (2003). The Size Distribution of Trans-Neptunian Bodies. *AJ, Submitted (AstroPH/0308467 v.1).*

Binzel, R. P., P. Farinella, V. Zappala, and A. Cellino (1989). Asteroid rotation rates - Distributions and statistics. In *Asteroids II*, pp. 416–441.

Bottke, W. F. and R. Greenberg (1993). Asteroidal collision probabilities. *Geophys. Res. Lett.* **20**, 879–881.

Bottke, W. F., R. Jedicke, A. Morbidelli, J. Petit, and B. Gladman (2000). Understanding the Distribution of Near-Earth Asteroids. *Science* **288**, 2190–2194.

Bottke, W. F., A. Morbidelli, R. Jedicke, J. Petit, H. F. Levison, P. Michel, and T. S. Metcalfe (2002). Debiased Orbital and Absolute Magnitude Distribution of the Near-Earth Objects. *Icarus* **156**, 399–433.

Bottke, W. F., M. C. Nolan, R. Greenberg, and R. A. Kolvoord (1994a). Collisional Lifetimes and Impact Statistics of Near-earth Asteroids. In *Hazards Due to Comets and Asteroids*, pp. 337–357.

Bottke, W. F., M. C. Nolan, R. Greenberg, and R. A. Kolvoord (1994b). Velocity distributions among colliding asteroids. *Icarus* **107**, 255–268.

Bottke, W. F., D. P. Rubincam, and J. A. Burns (2000). Dynamical evolution of main belt meteoroids: Numerical simulations incorporating planetary perturbations and Yarkovsky thermal forces. *Icarus* **145**, 301–331.

Bottke, W. F., D. Vokrouhlický, M. Brož, D. Nesvorný, and A. Morbidelli (2001). Dynamical Spreading of Asteroid Families by the Yarkovsky Effect. *Science* **294**, 1693–1696.

Bowell, E., B. Hapke, D. Domingue, K. Lumme, J. Peltoniemi, and A. W. Harris (1989). Application of photometric models to asteroids. In *Asteroids II*, pp. 524–556.

Brown, M. E. (2001). The Inclination Distribution of the Kuiper Belt. *AJ* **121**, 2804–2814.

Brown, P., R. E. Spalding, D. O. ReVelle, E. Tagliaferri, and S. P. Worden (2002). The flux of small near-Earth objects colliding with the Earth. *Nature* **420**, 294–296.

Burns, J. A., P. L. Lamy, and S. Soter (1979). Radiation forces on small particles in the solar system. *Icarus* **40**, 1–48.

Caffee, M. W., R. C. Reedy, J. N. Goswami, C. M. Hohenberg, and K. Marti (1988). Irradiation records in meteorites. In *Meteorites and the Early Solar System*, pp. 205–245.

Campo Bagatin, A., A. Cellino, D. R. Davis, P. Farinella, and P. Paolicchi (1994). Wavy size distributions for collisional systems with a small-size cutoff. *Planet. Space Sci.* **42**, 1079–1092.

Campo Bagatin, A., P. Farinella, and J.-M. Petit (1994). Fragment ejection velocities and the collisional evolution of asteroids. *Planet. Space Sci.* **42**, 1099–1107.

Chapman, C. R., W. J. Merline, and P. Thomas (1999). Cratering on Mathilde.

Icarus **140**, 28–33.

Chapman, C. R., W. J. Merline, P. C. Thomas, J. Joseph, A. F. Cheng, and N. Izenberg (2002). Impact History of Eros: Craters and Boulders. *Icarus* **155**, 104–118.

Chapman, C. R., E. V. Ryan, W. J. Merline, G. Neukum, R. Wagner, P. C. Thomas, J. Veverka, and R. J. Sullivan (1996). Cratering on Ida. *Icarus* **120**, 77–86.

Chapman, C. R., J. Veverka, M. J. S. Belton, G. Neukum, and D. Morrison (1996). Cratering on Gaspra. *Icarus* **120**, 231–245.

Chesley, S. R., S. J. Ostro, D. Vokrouhlický, D. Čapek, J. D. Giorgini, M. C. Nolan, J. Margot, A. A. Hine, L. A. M. Benner, and A. B. Chamberlin (2003). Direct Detection of the Yarkovsky Effect by Radar Ranging to Asteroid 6489 Golevka. *Science* **302**, 1739–1742.

Chladni, E. F. F. and G. Hoppe (1794). *Uber den kosmischen Ursprung der Meteorite und Feuerkugeln.* Leipzig: Geest & Portig, 1979. 1. Aufl.

Cochran, A. L., H. F. Levison, S. A. Stern, and M. J. Duncan (1995). The Discovery of Halley-sized Kuiper Belt Objects Using the Hubble Space Telescope. *ApJ* **455**, 342–346.

Consolmagno, G. J. and M. J. Drake (1977). Composition and evolution of the eucrite parent body - Evidence from rare earth elements. *Geochim. Cosmochim. Acta* **41**, 1271–1282.

Davis, D. R. (1999). The Collisional History of Asteroid 253 Mathilde. *Icarus* **140**, 49–52.

Davis, D. R., C. R. Chapman, S. J. Weidenschilling, and R. Greenberg (1985). Collisional history of asteroids: Evidence from Vesta and the Hirayama families. *Icarus* **63**, 30–53.

Davis, D. R. and P. Farinella (1997). Collisional Evolution of Edgeworth-Kuiper Belt Objects. *Icarus* **125**, 50–60.

Davis, D. R. and E. V. Ryan (1990). On collisional disruption - Experimental results and scaling laws. *Icarus* **83**, 156–182.

Davis, D. R., E. V. Ryan, and P. Farinella (1994). Asteroid collisional evolution: Results from current scaling algorithms. *Planet. Space Sci.* **42**, 599–610.

Davis, D. R., S. J. Weidenschilling, P. Farinella, P. Paolicchi, and R. P. Binzel (1989). Asteroid collisional history - Effects on sizes and spins. In *Asteroids II*, pp. 805–826.

Delbó, M., A. W. Harris, R. P. Binzel, P. Pravec, and J. K. Davies (2003). Keck observations of near-Earth asteroids in the thermal infrared. *Icarus* **166**, 116–130.

Dobrovolskis, A. R. and J. A. Burns (1984). Angular momentum drain - A mechanism for despinning asteroids. *Icarus* **57**, 464–476.

Dohnanyi, J. S. (1969). Collisional models of asteroids and their debris. *J. Geophys. Res.* **74**, 2531–2554.

Duncan, M., T. Quinn, and S. Tremaine (1988). The origin of short-period comets. *ApJ* **328**, L69–L73.

Duncan, M. J. and H. F. Levison (1997). A scattered comet disk and the origin of Jupiter family comets. *Science* **276**, 1670–1672.

Durda, D. D. (1993). The Collisional Evolution of the Asteroid Belt and Its Contribution to the Zodiacal Cloud. *Ph.D. Thesis, University of Florida.*

Durda, D. D. and S. F. Dermott (1997). The Collisional Evolution of the Asteroid Belt and Its Contribution to the Zodiacal Cloud. *Icarus* **130**, 140–164.

Durda, D. D., R. Greenberg, and R. Jedicke (1998). Collisional Models and Scaling Laws: A New Interpretation of the Shape of the Main-Belt Asteroid Size Distribution. *Icarus* **135**, 431–440.

Edgeworth, K. E. (1949). The origin and evolution of the Solar System. *MNRAS* **109**, 600–609.

Farinella, P. and D. R. Davis (1992). Collision rates and impact velocities in the Main Asteroid Belt. *Icarus* **97**, 111–123.

Farinella, P., C. Froeschle, C. Froeschle, R. Gonczi, G. Hahn, A. Morbidelli, and G. B. Valsecchi (1994). Asteroids falling onto the Sun. *Nature* **371**, 315–317.

Farinella, P., P. Paolicchi, and V. Zappala (1982). The asteroids as outcomes of catastrophic collisions. *Icarus* **52**, 409–433.

Farinella, P. and D. Vokrouhlicky (1999). Semimajor axis mobility of asteroidal fragments. *Science* **283**, 1507–1510.

Farinella, P., D. Vokrouhlicky, and W. K. Hartmann (1998a). Erratum: Meteorite Delivery via Yarkovsky Orbital Drift [Volume 132, Number 2, pages 378-387 (1998)]. *Icarus* **134**, 347.

Farinella, P., D. Vokrouhlicky, and W. K. Hartmann (1998b). Meteorite Delivery via Yarkovsky Orbital Drift. *Icarus* **132**, 378–387.

Feierberg, M. A. and M. J. Drake (1980). The meteorite-asteroid connection - The infrared spectra of eucrites, shergottites, and Vesta. *Science* **209**, 805–807.

Fernandez, J. A. (1980). On the existence of a comet belt beyond Neptune. *MNRAS* **192**, 481–491.

Froeschle, C. and A. Morbidelli (1994). The Secular Resonances in the Solar System. In *IAU Symp. 160: Asteroids, Comets, Meteors 1993*, pp. 189–204.

Fujiwara, A. (1980). On the mechanism of catastrophic destruction of minor planets by high-velocity impact. *Icarus* **41**, 356–364.

Fujiwara, A., G. Kamimoto, and A. Tsukamoto (1977). Destruction of basaltic bodies by high-velocity impact. *Icarus* **31**, 277–288.

Fujiwara, A. and A. Tsukamoto (1980). Experimental study on the velocity of fragments in collisional breakup. *Icarus* **44**, 142–153.

Gault, D. E., E. M. Shoemaker, and H. J. Moore (1963). Spray ejected from the Lunar surface by meteoroid impact. *NASA Tech. Note* **D-1767**.

Gladman, B., J. J. Kavelaars, J. Petit, A. Morbidelli, M. J. Holman, and T. Loredo (2001). The Structure of the Kuiper Belt: Size Distribution and Radial Extent. *AJ* **122**, 1051–1066.

Gladman, B. J., F. Migliorini, A. Morbidelli, V. Zappala, P. Michel, A. Cellino, C. Froeschle, H. F. Levison, M. Bailey, and M. Duncan (1997). Dynamical lifetimes of objects injected into asteroid belt resonances. *Science* **277**, 197–201.

Gomes, R. S. (2003). The origin of the Kuiper Belt high-inclination population. *Icarus* **161**, 404–418.

Greenberg, R., W. F. Bottke, M. Nolan, P. Geissler, J. Petit, D. D. Durda, E. Asphaug, and J. Head (1996). Collisional and Dynamical History of Ida. *Icarus* **120**, 106–118.

Greenberg, R. and C. R. Chapman (1983). Asteroids and meteorites - Parent bodies and delivered samples. *Icarus* **55**, 455–481.

Greenberg, R., W. K. Hartmann, C. R. Chapman, and J. F. Wacker (1978). Planetesimals to planets - Numerical simulation of collisional evolution. *Icarus* **35**, 1–26.

Greenberg, R. and M. C. Nolan (1989). Delivery of asteroids and meteorites to the inner solar system. In *Asteroids II*, pp. 778–801.

Greenberg, R., M. C. Nolan, W. F. Bottke, R. A. Kolvoord, and J. Veverka (1994). Collisional history of Gaspra. *Icarus* **107**, 84–97.

Greenberg, R. and D. P. O'Brien (2003). Boulders and craters on Eros: Mutually consistent size distributions. *AAS/Division for Planetary Sciences Meeting* **35**, 960.

Harris, A. W. (2002). A New Estimate of the Population of Small NEAs. *Bulletin of the American Astronomical Society* **34**, 835.

Hartmann, W. K., P. Farinella, D. Vokrouhlicky, S. J. Weidenschilling, A. Morbidelli, F. Marzari, D. R. Davis, and E. Ryan (1999). Reviewing the Yarkovsky effect: New light on the delivery of stone and iron meteorites from the asteroid belt . *Meteoritics and Planetary Science* **34**, 161–167.

Hartmann, W. K. and E. V. Ryan (1996). Possible Evidence of Yarkovsky Depletion of Debris from the Asteroid Belt and Effects on Asteroid Surfaces. *Bulletin of the American Astronomical Society* **28**, 1103.

Hirayama, K. (1918). A possible explanation of the gaps in the distribution of the mean motions of the asteroids. *Annals of the Tokyo Astronomical Observatory* **5**, 185–188.

Holman, M. J. and J. Wisdom (1993). Dynamical stability in the outer solar system and the delivery of short period comets. *AJ* **105**, 1987–1999.

Holsapple, K. A. (1994). Catastrophic disruptions and cratering of solar system bodies: A review and new results. *Planet. Space Sci.* **42**, 1067–1078.

Holsapple, K. A. and R. M. Schmidt (1982). On the scaling of crater dimensions. II - Impact processes. *J. Geophys. Res.* **87**, 1849–1870.

Housen, K. R. (1991). Laboratory simulations of large-scale fragmentation events. *Icarus* **94**, 180–190.

Housen, K. R. and K. A. Holsapple (1990). On the fragmentation of asteroids and planetary satellites. *Icarus* **84**, 226–253.

Housen, K. R. and K. A. Holsapple (1999). Scale Effects in Strength-Dominated Collisions of Rocky Asteroids. *Icarus* **142**, 21–33.

Ivezić, Ž., S. Tabachnik, R. Rafikov, R. H. Lupton, T. Quinn, M. Hammergren, L. Eyer, J. Chu, J. C. Armstrong, X. Fan, K. Finlator, T. R. Geballe, J. E. Gunn, G. S. Hennessy, G. R. Knapp, S. K. Leggett, J. A. Munn, J. R. Pier, C. M. Rockosi, D. P. Schneider, M. A. Strauss, B. Yanny, J. Brinkmann, I. . Csabai, R. B. Hindsley, S. Kent, D. Q. Lamb, B. Margon, T. A. McKay, J. A. Smith, P. Waddel, D. G. York, and the SDSS Collaboration (2001). Solar System Objects Observed in the Sloan Digital Sky Survey Commissioning Data. *AJ* **122**, 2749–2784.

Jaeger, J. C. and N. G. W. Cook (1969). *Fundamentals of Rock Mechanics.* Chapman and Hall, London.

Jedicke, R. and T. S. Metcalfe (1998). The Orbital and Absolute Magnitude Distributions of Main Belt Asteroids. *Icarus* **131**, 245–260.

Jewitt, D. and J. Luu (1993). Discovery of the candidate Kuiper belt object 1992 QB1. *Nature* **362**, 730–732.

Kenyon, S. J. and J. X. Luu (1998). Accretion in the Early Kuiper Belt. I. Coagulation and Velocity Evolution. *AJ* **115**, 2136–2160.

Kirkwood, D. (1867). *Meteoric astronomy: a treatise on shooting-stars, fireballs, and aerolites.* Philadelphia, J. B. Lippincott & co., 1867.

Knežević, Z., A. Lemaître, and A. Milani (2002). The Determination of Asteroid Proper Elements. *Asteroids III*, 603–612.

Knežević, Z. and A. Milani (2003). Proper element catalogs and asteroid families. *A&A* **403**, 1165–1173.

Kuiper, G. P. (1951). On the Origin of the Solar System. In J. A. Hynek (Ed.), *Proceedings of a topical symposium, commemorating the 50th anniversary of the Yerkes Observatory and half a century of progress in astrophysics*, pp. 357–424. New York: McGraw-Hill.

Levison, H. F. and M. J. Duncan (1994). The long-term dynamical behavior of short-period comets. *Icarus* **108**, 18–36.

Levison, H. F. and M. J. Duncan (1997). From the Kuiper Belt to Jupiter-Family Comets: The Spatial Distribution of Ecliptic Comets. *Icarus* **127**, 13–32.

Levison, H. F. and A. Morbidelli (2003). The formation of the Kuiper belt by the outward transport of bodies during Neptune's migration. *Nature* **426**, 419–421.

Love, S. G. and T. J. Ahrens (1996). Catastrophic Impacts on Gravity Dominated Asteroids. *Icarus* **124**, 141–155.

Malhotra, R. (1995). The Origin of Pluto's Orbit: Implications for the Solar System Beyond Neptune. *AJ* **110**, 420–429.

Marti, K. and T. Graf (1992). Cosmic-ray exposure history of ordinary chondrites. *Annual Review of Earth and Planetary Sciences* **20**, 221–243.

Marzari, F., P. Farinella, and D. R. Davis (1999). Origin, Aging, and Death of Asteroid Families. *Icarus* **142**, 63–77.

McCord, T. B., J. B. Adams, and T. V. Johnson (1970). Asteroid Vesta: Spectral reflectivity and compositional implications. *Science* **178**, 745–747.

Melosh, H. J. (1989). *Impact cratering: A geologic process.* Oxford University Press, New York.

Melosh, H. J. and E. V. Ryan (1997). NOTE: Asteroids: Shattered but Not Dispersed. *Icarus* **129**, 562–564.

Melosh, H. J., E. V. Ryan, and E. Asphaug (1992). Dynamic fragmentation in impacts - Hydrocode simulation of laboratory impacts. *J. Geophys. Res.* **97**, 14735–14759.

Michel, P., W. Benz, and D. C. Richardson (2003). Disruption of fragmented parent bodies as the origin of asteroid families. *Nature* **421**, 608–611.

Michel, P., P. Tanga, W. Benz, and D. C. Richardson (2002). Formation of Asteroid Families by Catastrophic Disruption: Simulations with Fragmentation and Gravitational Reaccumulation. *Icarus* **160**, 10–23.

Migliorini, F., P. Michel, A. Morbidelli, D. Nesvorny, and V. Zappala (1998). Origin of Multikilometer Earth- and Mars-Crossing Asteroids: A Quantitative Simulation. *Science* **281**, 2022–2024.

Moons, M. (1997). Review of the dynamics in the Kirkwood gaps. *Celestial Mechanics and Dynamical Astronomy* **65**, 175–204.

Morbidelli, A. (1997). Chaotic Diffusion and the Origin of Comets from the 2/3 Resonance in the Kuiper Belt. *Icarus* **127**, 1–12.

Morbidelli, A. (1999). Origin and Evolution of Near Earth Asteroids. *Celestial Mechanics and Dynamical Astronomy* **73**, 39–50.

Morbidelli, A. and B. Gladman (1998). Orbital and temporal distributions of meteorites originating in the asteroid belt. *Meteoritics and Planetary Science* **33**, 999–1016.

Morbidelli, A. and D. Nesvorný (1999). Numerous Weak Resonances Drive Asteroids toward Terrestrial Planets Orbits. *Icarus* **139**, 295–308.

Morbidelli, A. and D. Vokrouhlický (2003). The Yarkovsky-driven origin of near-Earth asteroids. *Icarus* **163**, 120–134.

Nakamura, A. and A. Fujiwara (1991). Velocity distribution of fragments formed in a simulated collisional disruption. *Icarus* **92**, 132–146.

Nesvorný, D. and A. Morbidelli (1998). Three-Body Mean Motion Resonances and the Chaotic Structure of the Asteroid Belt. *AJ* **116**, 3029–3037.

Nolan, M. C., E. Asphaug, H. J. Melosh, and R. Greenberg (1996). Impact Craters on Asteroids: Does Gravity or Strength Control Their Size? *Icarus* **124**, 359–371.

O'Brien, D. P. and R. Greenberg (2003). Steady-state size distributions for collisional populations:analytical solution with size-dependent strength. *Icarus* **164**, 334–345.

Öpik, E. J. (1951). Collision probability with the planets and the distribution of planetary matter. *Proc. R. Irish Acad. Sect. A* **54**, 165–199.

Peterson, C. (1976). A source mechanism for meteorites controlled by the Yarkovsky effect. *Icarus* **29**, 91–111.

Petit, J. and P. Farinella (1993). Modelling the outcomes of high-velocity impacts between small solar system bodies. *Celestial Mechanics and Dynamical Astronomy* **57**, 1–28.

Petit, J., A. Morbidelli, and J. Chambers (2001). The Primordial Excitation and Clearing of the Asteroid Belt. *Icarus* **153**, 338–347.

Petit, J., A. Morbidelli, and G. B. Valsecchi (1999). Large Scattered Planetesimals and the Excitation of the Small Body Belts. *Icarus* **141**, 367–387.

Piotrowski, S. I. (1953). The collisions of asteroids. *Acta Astronomica* **6**, 115–138.

Piotrowski, S. L. (1952). The collisions of asteroids. *AJ* **57**, 23–24.

Pravec, P., A. W. Harris, and T. Michalowski (2002). Asteroid Rotations. *Asteroids III*, 113–122.

Quinn, T., S. Tremaine, and M. Duncan (1990). Planetary perturbations and the origins of short-period comets. *ApJ* **355**, 667–679.

Rabinowitz, D., E. Helin, K. Lawrence, and S. Pravdo (2000). A reduced estimate of the number of kilometre-sized near-earth asteroids. *Nature* **403**, 165–166.

Rabinowitz, D. L., E. Bowell, E. M. Shoemaker, and K. Muinonen (1994). The Population of Earth-crossing Asteroids. In *Hazards Due to Comets and Asteroids*, pp. 285–312.

Radzievskii, V. V. (1952). A mechanism for the disintegration of asteroids and meteorites. *AZh* **29**, 162–170.

Richardson, J. E., H. J. Melosh, and R. Greenberg (2004). The Seismic Effect of Impacts on Asteroid Surface Morphology: Early Modeling Results. In *Lunar and Planetary Institute Conference Abstracts*, pp. 1864.

Rubincam, D. P. (1995). Asteroid orbit evolution due to thermal drag. *J. Geophys. Res.* **100**, 1585–1594.

Rubincam, D. P., D. D. Rowlands, and R. D. Ray (2002). Is asteroid 951 Gaspra in a resonant obliquity state with its spin increasing due to YORP? *Journal of Geophysical Research (Planets)* **107**, 3–1.

Ryan, E. V. and H. J. Melosh (1998). Impact Fragmentation: From the Laboratory to Asteroids. *Icarus* **133**, 1–24.

Spitale, J. and R. Greenberg (2001). Numerical Evaluation of the General Yarkovsky Effect: Effects on Semimajor Axis. *Icarus* **149**, 222–234.

Spitale, J. and R. Greenberg (2002). Numerical Evaluation of the General Yarkovsky Effect: Effects on Eccentricity and Longitude of Periapse. *Icarus* **156**, 211–222.

Stern, S. A. and J. E. Colwell (1997). Accretion in the Edgeworth-Kuiper Belt: Forming 100-1000 KM Radius Bodies at 30 AU and Beyond. *AJ* **114**, 841–849.

Stoeffler, D., D. E. Gault, J. Wedekind, and G. Polkowski (1975). Experimental hypervelocity impact into quartz sand - Distribution and shock metamorphism of ejecta. *J. Geophys. Res.* **80**, 4062–4077.

Stuart, J. S. (2001). A Near-Earth Asteroid Population Estimate from the LINEAR Survey. *Science* **294**, 1691–1693.

Tanaka, H., S. Inaba, and K. Nakazawa (1996). Steady-State Size Distribution for the Self-Similar Collision Cascade. *Icarus* **123**, 450–455.

Thomas, P. C., M. J. S. Belton, B. Carcich, C. R. Chapman, M. E. Davies, R. Sullivan, and J. Veverka (1996). The Shape of Ida. *Icarus* **120**, 20–32.

Thomas, P. C., J. Joseph, B. Carcich, J. Veverka, B. E. Clark, J. F. Bell, A. W. Byrd, R. Chomko, M. Robinson, S. Murchie, L. Prockter, A. Cheng, N. Izenberg, M. Malin, C. Chapman, L. A. McFadden, R. Kirk, M. Gaffey, and P. G. Lucey (2002). Eros: Shape, Topography, and Slope Processes. *Icarus* **155**, 18–37.

Thomas, P. C., J. Veverka, D. Simonelli, P. Helfenstein, B. Carcich, M. J. S. Belton, M. E. Davies, and C. Chapman (1994). The shape of Gaspra. *Icarus* **107**, 23–36.

Trujillo, C. A. and M. E. Brown (2001). The Radial Distribution of the Kuiper Belt. *ApJ* **554**, L95–L98.

Veverka, J., M. Robinson, P. Thomas, S. Murchie, J. F. Bell, N. Izenberg, C. Chapman, A. Harch, M. Bell, B. Carcich, A. Cheng, B. Clark, D. Domingue, D. Dunham, R. Farquhar, M. J. Gaffey, E. Hawkins, J. Joseph, R. Kirk, H. Li, P. Lucey, M. Malin, P. Martin, L. McFadden, W. J. Merline, J. K. Miller, W. M. Owen, C. Peterson, L. Prockter, J. Warren, D. Wellnitz, B. G. Williams, and D. K. Yeomans (2000). NEAR at Eros: Imaging and Spectral Results. *Science* **289**, 2088–2097.

Veverka, J., P. Thomas, A. Harch, B. Clark, J. F. Bell, B. Carcich, J. Joseph, S. Murchie, N. Izenberg, C. Chapman, W. Merline, M. Malin, L. McFadden, and M. Robinson (1999). NEAR Encounter with Asteroid 253 Mathilde: Overview. *Icarus* **140**, 3–16.

Vokrouhlický, D. (1998a). Diurnal Yarkovsky effect as a source of mobility of meter-sized asteroidal fragments. I. Linear theory. *A&A* **335**, 1093–1100.

Vokrouhlický, D. (1998b). Diurnal Yarkovsky effect as a source of mobility of meter-sized asteroidal fragments. II. Non-sphericity effects. *A&A* **338**, 353–363.

Vokrouhlický, D. (1999). A complete linear model for the Yarkovsky thermal force on spherical asteroid fragments. *A&A* **344**, 362–366.

Vokrouhlický, D. and M. Brož (1999). An improved model of the seasonal Yarkovsky force for regolith-covered asteroid fragments. *A&A* **350**, 1079–1084.

Vokrouhlický, D. and P. Farinella (1998). The Yarkovsky Seasonal Effect on Asteroidal Fragments: A Nonlinearized Theory for the Plane-Parallel Case. *AJ* **116**, 2032–2041.

Vokrouhlický, D. and P. Farinella (1999). The Yarkovsky Seasonal Effect on Asteroidal Fragments: A Nonlinearized Theory for Spherical Bodies. *AJ* **118**, 3049–3060.

Vokrouhlický, D. and P. Farinella (2000). Efficient delivery of meteorites to the Earth from a wide range of asteroid parent bodies. *Nature* **407**, 606–608.

Vokrouhlický, D. and D. Čapek (2002). YORP-Induced Long-Term Evolution of the Spin State of Small Asteroids and Meteoroids: Rubincam's Approximation. *Icarus* **159**, 449–467.

Welten, K. C., L. Lindner, K. van der Borg, T. Loeken, P. Scherer, and L. Schultz (1997). Cosmic-ray exposure ages of diogenites and the recent collisional history of the HED parent body/bodies. *Meteoritics and Planetary Science* **32**, 891–902.

Werner, S. C., A. W. Harris, G. Neukum, and B. A. Ivanov (2002). NOTE: The Near-Earth Asteroid Size-Frequency Distribution: A Snapshot of the Lunar Impactor Size-Frequency Distribution. *Icarus* **156**, 287–290.

Wetherill, G. W. (1976). Where do the meteorites come from - A re-evaluation of the earth-crossing Apollo objects as sources of chondritic meteorites. *Geochim. Cosmochim. Acta* **40**, 1297–1317.

Wetherill, G. W. (1979). Steady state populations of Apollo-Amor objects. *Icarus* **37**, 96–112.

Wetherill, G. W. (1985). Asteroidal source of ordinary chondrites (Meteoritical Society Presidential Address 1984). *Meteoritics* **20**, 1–22.

Wetherill, G. W. (1987). Dynamical relations between asteroids, meteorites and Apollo-Amor objects. *Royal Society of London Philosophical Transactions Series A* **323**, 323–337.

Wetherill, G. W. (1988). Where do the Apollo objects come from? *Icarus* **76**, 1–18.

Williams, D. R. and G. W. Wetherill (1994). Size distribution of collisionally evolved asteroidal populations - Analytical solution for self-similar collision cascades. *Icarus* **107**, 117–128.

Williams, J. G. (1969). Secular Perturbations in the Solar System. *Ph.D. Thesis, University of California, Los Angeles.*

Williams, J. G. and J. Faulkner (1981). The positions of secular resonance surfaces. *Icarus* **46**, 390–399.

Wisdom, J. (1982). The origin of the Kirkwood gaps - A mapping for asteroidal motion near the 3/1 commensurability. *AJ* **87**, 577–593.

Wisdom, J. (1983). Chaotic behavior and the origin of the 3/1 Kirkwood gap. *Icarus* **56**, 51–74.

Yoshida, F., T. Nakamura, J. Watanabe, D. Kinoshita, N. Yamamoto, and T. Fuse (2003). Size and Spatial Distributions of Sub-km Main-Belt Asteroids. *PASJ* **55**, 701–715.

Zappalá, V., P. Bendjoya, A. Cellino, P. Farinella, and C. Froeschle (1995). Asteroid families: Search of a 12,487-asteroid sample using two different clustering techniques. *Icarus* **116**, 291–314.